Fakultät für
Mathematik, Informatik
und Naturwissenschaften

RWTH AACHEN UNIVERSITY

Extensive Optimization of a Simulation Model for the Electric Dipole Moment Measurement at the Cooler Synchrotron COSY

Von der Fakultät für Mathematik, Informatik und Naturwissenschaften der RWTH Aachen University zur Erlangung des akademischen Grades einer Doktorin der Naturwissenschaften genehmigte Dissertation

vorgelegt von

Vera Poncza, M.Sc., M.Sc.

aus

Siegen

Berichter: Univ.-Prof. Dr. rer. nat. Andreas Lehrach
Univ.-Prof. Dr. rer. nat. Andrzej Magiera
Univ.-Prof. Dr. rer. nat. Achim Stahl

Tag der mündlichen Prüfung: 05. Mai 2021

Abstract

The excess of matter in the known part of the universe still poses a puzzle to physics and cannot be explained by the Standard Model of particle physics. Many explanation attempts are based on mechanisms that violate $\mathcal{CP}$ symmetry. Such mechanisms exist in the Standard Model but are too weak to explain the observed asymmetry. Therefore, additional theories beyond the Standard Model are needed, which are mostly based on additional $\mathcal{CP}$ violating sources. Permanent Electrical Dipole Moments (EDMs) of elementary particles violate $\mathcal{CP}$ symmetry and are therefore a promising starting point for investigations of the underlying problem. EDMs of charged particles can be studied using storage rings as particle traps, where the polarization behavior of the beam in electric fields provides information about the size of the EDM.

The JEDI (Jülich Electric Dipole moment Investigations) collaboration is specialized in the search for EDMs of hadrons using storage rings. It is engaged in design studies for dedicated storage rings for the investigation of protons and deuterons and uses the magnetic storage ring, the cooler synchrotron, COSY at Forschungszentrum Jülich for the first direct deuteron EDM experiment. In this experiment, an EDM leads to a vertical polarization buildup that is directly proportional to the size of the EDM. However, the vertical polarization component is also influenced by systematic effects such as magnet misalignments. In order to investigate systematic effects individually and to support the data analysis, a realistic simulation model is required. In this thesis the development of such a model based on the *Bmad* software library is presented. Furthermore, various systematic effects and their impact on the spin motion in COSY are investigated and quantified using tracking simulations. The consideration of measured magnet misalignments and their measurement errors results in a minimum resolvable EDM of $d = 1.49 \cdot 10^{-19}$ e $\cdot$ cm. For a more realistic description of the experimental situation, algorithms are implemented which fit the simulation model to the real conditions by variation of selected machine parameters. The algorithms are successfully tested by means of simulations and afterwards applied to measurement data. The fit results confirm additional magnetic displacements and lead overall to a significantly increased agreement between simulation model and reality.

Zusammenfassung

Der Materieüberschuss im bekannten Teil des Universums stellt die Physik immer noch vor ein Rätsel und kann vom Standardmodell der Teilchenphysik nicht erklärt werden. Viele Erklärungsversuche basieren auf $\mathcal{CP}$ verletzenden Mechanismen, die zwar im Standardmodell existieren, jedoch zu schwach ausgeprägt sind, um die beobachtete Asymmetrie auslösen zu können. Daher bedarf es zusätzlicher Theorien jenseits des Standardmodells, die zum Großteil auf zusätzlichen $\mathcal{CP}$ verletzenden Quellen basieren. Permanente elektrische Dipolmomente (EDMs) von Elementarteilchen verletzen die $\mathcal{CP}$ Symmetrie und sind somit ein vielversprechender Ansatzpunkt für das zugrunde liegende Problem. EDMs geladener Teilchen können mit Hilfe von Speicherringen untersucht werden wobei das Polarisationsverhalten des Strahls in elektrischen Feldern Aufschluss über die Größe des EDMs gibt.

Die JEDI (Jülich Electric Dipole moment Investigations) Kollaboration hat sich auf die Suche nach EDMs von Hadronen mit Hilfe von Speicherringen spezialisiert. Sie beschäftigt sich mit Designstudien für dedizierte Speicherringe zur Untersuchung von Protonen und Deuteronen und nutzt den magnetischen Speicherring, das Kühlersynchrotron, COSY im Forschungszentrum Jülich zur erstmaligen Untersuchung des Deuteron EDMs. Im Rahmen dieses Experiments führt ein EDM zu einem vertikalen Polarisationsaufbau, der direkt proportional zur Größe des EDMs ist. Die vertikale Polarisationskomponente wird allerdings auch durch systematische Effekte, wie Magnetverschiebungen, beeinflusst. Um systematische Effekte isoliert untersuchen zu können und die Datenanalyse zu unterstützen bedarf es eines differenzierten Simulationsmodells. In dieser Arbeit wird die Entwicklung eines solchen Modells auf Basis der *Bmad* Programmbibliothek vorgestellt. Darüber hinaus werden verschiedene systematische Effekte und deren Auswirkung auf die Spinbewegung in COSY mit Hilfe von Trackingsimulationen untersucht und quantifiziert. Durch die Berücksichtigung gemessener Magnetfehlstellungen und deren Messfehlern ergibt sich ein minimal auflösbares EDM von $d = 1.49 \cdot 10^{-19}$ e $\cdot$ cm. Für eine realistischere Beschreibung der Experimentsituation werden des Weiteren Algorithmen implementiert, die das Simulationsmodell durch Variation ausgewählter Maschinenparameter an die echten Begebenheiten anpassen. Die Algorithmen werden mit Hilfe von Simulationen erfolgreich getestet und daraufhin auf Messdaten angewendet. Die resultierenden Ergebnisse bestätigen zusätzliche Magnetverschiebungen und führen insgesamt zu einer deutlich erhöhten Übereinstimmung von Simulationsmodell und Realität.

Contents

Nomenclature

$\mathcal{CPT}$	Combined charge conjugation, parity and time reversal transformation
$\mathcal{CP}$	Combined charge conjugation and parity transformation
$\mathcal{C}$	Charge conjugation transformation
$\mathcal{P}$	Parity transformation
$\mathcal{T}$	Time reversal transformation
AMS	Alpha Magnetic Spectrometer
BNL	Brookhaven National Laboratory
BNN	Big Bang Nucleosynthesis
BPM	Beam Position Monitor
CKM	Cabibbo-Kobayashi-Maskawa matrix
CMB	Cosmic Microwave Background
COSY	COoler SYnchrotron
EDM	Electric Dipole Moment
EPICS	Experimental Physics and Industrial Control System
JEDI	Jülich Electric Dipole moment Investigations
JEPO	JEDI Polarimeter
LAPACK	Linear Algebra PACKage
MDM	Magnetic Dipole Moment
ORM	Orbit Response Matrix
QCD	Quantum Chromo Dynamics
RF	Radio Frequency

RMS ..... Root Mean Square

SCM ..... Standard Model of Cosmology

SM ..... Standard Model of particle physics

SVD ..... Singula Value Decomposition

WASA ..... Wide Angle Shower Apparatus

WMAP ..... Wilkinson Microwave Anisotropy Probe

1. Introduction

The matter over antimatter dominance observed in the universe is one of the large unsolved questions in particle physics. Although the Standard Model of particle physics (SM) is very successful in describing elementary particles and their interactions, it still fails to explain the disappearance of antimatter during the early universe. Many theories beyond the SM trying to answer this question are based on the assumption of the violation of fundamental symmetries. An additional source of $\mathcal{CP}$ violation not predicted by the SM could be manifested by the existence of permanent Electric Dipole Moments (EDMs) of elementary particles which are highly suppressed in the SM. Some extensions of the SM predict EDM values that could be sufficiently large to be measured by high-precision experiments. The search for permanent EDMs has already started more than 60 years ago and up to now all measurements have been consistent with zero within the systematical sensitivity. Typical experiments are based on the idea of trapping particles and using electric fields to manipulate the polarization that is directly influenced by the EDM. Since charged particles are accelerated inside an external electric field, a measurement setup is needed that inhibits the particles from being lost. Storage rings offer the possibility to serve as a trap for charged particles and are therefore predestined for performing EDM experiments.

The Jülich Electric Dipole moment Investigations (JEDI) collaboration aims for measuring the proton and deuteron EDM in a dedicated storage ring with high statistical and systematical sensitivity. Therefore, design studies are under investigation including optics and spin calculations. The existing accelerator facility COoler SYnchrotron (COSY) at Forschungszentrum Jülich in Germany is used as a starting point of these studies and a first direct deuteron EDM measurement is performed. In order to do so, spin manipulating devices as well as a new polarimeter are installed into the storage ring. In order to increase the systematical sensitivity, magnets were realigned to their target position and a beam based alignment procedure was performed in COSY [1, 2]. A first deuteron EDM measurement run was already performed in November 2018 and the data analysis is currently in progress. Starting with an initial polarization in the horizontal plane, a non-vanishing EDM leads to a vertical polarization component that is directly proportional to the EDM magnitude. Besides the EDM itself, various systematic effects such as horizontally misaligned quadrupoles, affect the vertical spin components. In order to disentangle the actual EDM signal from these additional effects, spin tracking simulations have to be performed.

The aim of this thesis is the improvement of the simulation model of COSY in order to support the data analysis and study systematic effects. Therefore, the model is extended by a realistic model of the RF Wien filter that is essential for the EDM experiment at COSY. Furthermore, different systematic effects are implemented and studied and a fitting procedure based on orbit response matrix measurements is presented. The thesis is structured as follows.

Chapter 2 gives an overview over the matter antimatter problem in the SM and motivates the theoretical background of the topic. As part of discussing fundamental symmetries, the EDM is introduced and different EDM measurement procedures are shown. Chapter 3 and Chapter 4 introduce aspects of beam and spin dynamics. Here, the focus lies on the equations of motion describing particle trajectories and the time-dependent evolution of spins in electromagnetic fields. The accelerator facility COSY as well as the simulation model are introduced in Chapter 5. After comparing the particle and spin behaviour to theoretical predictions, extensions to the model are explained and tested. The effect of magnet misalignments as well as the effective lengths of dipoles and quadrupoles are investigated in Chapter 6. Finally, Chapter 7 introduces algorithms that can be used to fit the model to the real machine by comparing orbit and orbit response matrix measurements to simulation results. The algorithms are first benchmarked and afterwards applied to real measurements. Chapter 8 summarizes the results and an outlook is given.

2. Scientific Motivation

The present thesis was accomplished within the JEDI collaboration [3]. The overall aim of the collaboration is to investigate possible experiments for measuring the permanent EDM of charged particles in storage rings. In this chapter it is discussed why EDMs are of high interest for the particle physics community and an overview of already existing EDM experiments and their results is given.

2.1 Matter-Antimatter Asymmetry

The observed imbalance in baryonic matter and antibaryonic matter in the Universe postulates one of the unsolved questions in cosmology and particle physics. According to the most common models the Universe expanded exponentially after the Big Bang. After this so called inflation stopped, the temperature was high enough to create and annihilate particle-antiparticle pairs in thermal equilibrium. At some point the Universe cooled down to a level where the critical particle energy for pair production was no longer given and matter and antimatter annihilated into photons [4]. As witnessed by the material existence of this thesis and its reader, the Universe does not merely consist of photons and thus matter and antimatter behaved differently after the Big Bang. A well-established quantity to express this matter-antimatter-asymmetry is the so called baryon asymmetry:

$$\eta_{BA} = \frac{N_B - N_{\overline{B}}}{N_\gamma}, \tag{2.1}$$

which is the difference of the baryon density N_B and the antibaryon density $N_{\overline{B}}$ over the density of cosmic background radiation photons N_γ just before the disappearance of the antibaryons [5]. It is part of cosmological models and can be determined experimentally using astrophysical observations. One observable are the temperature fluctuations in the Cosmic Microwave Background (CMB), which were investigated within the Wilkinson Microwave Anisotropy Probe (WMAP) experiment. A second experiment to measure η_{BA} investigated the abundances of light elements that were produced during the Big Bang Nucleosynthesis (BNN). Both results are in good agreement and state a baryon asymmetry of [4]

$$\eta_{BA}^{BNN} = (6.07 \pm 0.33) \cdot 10^{-10} \quad \text{(BNN)} \tag{2.2}$$

$$\eta_{BA}^{CMB} = 6.16^{+0.153}_{-0.156} \cdot 10^{-10} \quad \text{(CMB)}. \tag{2.3}$$

On the other hand estimates based on the SM and the Standard Model of Cosmology (SMC) yield $\eta_{BA} \approx 10^{-18}$ which is eight orders of magnitude below the measured value [6].
One could think about two possible explanations for the absence of the antimatter:

1. Either the antimatter still exists in areas that are separated from matter dominated regions. In this case the Milky Way is part of such a matter dominated region resulting in the observation of the matter excess.

2. Or the antimatter was annihilated in asymmetric processes during the further evolution of the Universe, known as baryogenesis.

The first case requires the search for existing antimatter as it is done by the Alpha Magnetic Spectrometer (AMS) experiment on the International Space Station (ISS) [7]. For the baryogenesis three conditions have to be fulfilled that were originally postulated by Andrei Sakharov in 1967 [8]:

1. **Baryon number violation:** Since the initial baryon number B was zero, the baryon number violation is necessary to reach a state with an excess of baryons over antibaryons.

2. **Violation of $\mathcal{C}$ and $\mathcal{CP}$ symmetries:** The probabilities of creating a particle and an antiparticle respectively only differ if the charge conjugation symmetry $\mathcal{C}$ and the combined charge and parity transformation symmetry $\mathcal{CP}$ are violated.

3. **Being out of thermal equilibrium:** If a system is in thermal equilibrium each process takes place as often as the reversed process. Thus, it would be impossible to achieve a baryon asymmetry.

However the $\mathcal{CP}$ violation incorporated in the SM is not sufficient in order to explain the measured matter-antimatter asymmetry. Therefore additional sources of $\mathcal{CP}$ violation from theories beyond the SM are needed. Permanent EDMs of elementary particles are candidates for such processes as discussed later in this chapter.

2.2 Discrete Symmetries and their Transformations

Generally speaking a symmetry is an operation under which a system stays invariant. The relation between conservation laws and symmetries, published by Emmy Noether in 1917, makes symmetries an important tool in elementary particle physics. Every (local) continuous symmetry of nature is related to a conservation law. Or in other words each conservation law reflects an underlying

symmetry. Energy and momentum conservation are results of the time and space translation symmetries of the Universe and the conservation of the angular momentum is coupled to the rotational symmetry of a physical system. Besides these so called *continuous symmetries* additional symmetries called *discrete symmetries* were found within the development of quantum mechanics. The three fundamental discrete transformations are explained in more detail in the following [9].

Parity Transformation

Applying the parity transformation $\mathcal{P}$ is equivalent to the inversion of all three spatial coordinates while leaving the time coordinates unchanged

$$(\vec{x}, t) \rightarrow (\vec{x'}, t') = (-\vec{x}, t). \tag{2.4}$$

Thus, being symmetric under the parity transformation implies that a process and its mirror image process behave in exactly the same way. Polar vectors such as displacement, momentum and acceleration are affected by the transformation while axial vectors such as the angular momentum are not. Regarding electromagnetic fields in a physical system, electric fields which are represented by polar vectors will be reversed by the $\mathcal{P}$ transformation whereas magnetic fields keep their directions since they are axial vectors [10]. This will be important when dealing with EDMs in Section 2.3.
While the electromagnetic and the strong interactions of the SM are symmetrical under $\mathcal{P}$, the weak interaction is parity violating. Triggered by the observation of K^+ meson decays into a final state of two and three pions respectively, in 1956 Lee and Yang suggested to study parity violation for weak interactions by investigating β decays [11]. Shortly afterwards, Wu et. al experimentally analyzed the beta decay of polarized ^{60}Co [12]:

$$^{60}\mathrm{Co} \rightarrow \ ^{60}\mathrm{Ni} + \mathrm{e}^- + \overline{\nu}_e. \tag{2.5}$$

It was found that the emitted electrons were more favored to fly in the direction opposite to the nuclear spin no matter if the polarizing field changed its sign. Since the polarization direction is not affected by the parity transformation but the momentum and therefore the flight direction changes under $\mathcal{P}$ the measurement shows evidence for parity violation. Additionally, the investigation of charged pion decays resulted in the observation of the neutrino spin being always anti-aligned to the momentum vector whereas the spin of the anti-neutrino points along the direction of flight. Thus, under the assumption of massless neutrinos, only left-handed neutrinos and right-handed anti-neutrinos couple to the weak interaction in the SM [13].

Charge Conjugation Transformation

The charge conjugation transformation $\mathcal{C}$ replaces a particle by its antiparticle in the underlying physical process. Therefore, additive quantum numbers such as charge, baryon and lepton number or strangeness are inverted whereas other quantities such as spin, position or momentum are not affected. Inverting the charge directly implies a change of direction of electric and magnetic fields. Violations of the $\mathcal{C}$ symmetry can be find in the weak section of the SM. Evidence for such a $\mathcal{C}$ violation can be seen by considering the $\mathcal{C}$ transformation of a left-handed neutrino resulting in a left-handed anti-neutrino. As already mentioned above, left-handed anti-neutrinos do not participate in weak interactions in the SM [10, 14].

Time Reversal Transformation

The third discrete transformation is the time reversal transformation $\mathcal{T}$. It inverts the sign of the time coordinate while leaving the spatial coordinates fixed

$$(\vec{x}, t) \rightarrow (\vec{x'}, t') = (\vec{x}, -t). \tag{2.6}$$

For a time symmetric process the particular reaction rate should be the same as for the reverse reaction. Several tests for the strong and the electromagnetic interactions show no evidence for $\mathcal{T}$ violation. Experiments in the weak sector are hard to perform but taking the $\mathcal{CPT}$ theorem into account, a valid measurement for $\mathcal{T}$ violation in weak interactions could be performed. The $\mathcal{CPT}$ theorem states that each combination of all transformations ($\mathcal{CPT}$) results in a symmetric process for Lorentz invariant local quantum field theory [9]. Hence, a $\mathcal{T}$ violating process is $\mathcal{CP}$ violating at the same time. Measuring the probability of the transformation $\overline{\mathrm{K}}^0 \rightarrow \mathrm{K}^0$ and the reversed process $\mathrm{K}^0 \rightarrow \overline{\mathrm{K}}^0$ resulted in rate asymmetries proofing a direct violation of the $\mathcal{T}$ symmetry [15]:

$$\left\langle \frac{R(\overline{\mathrm{K}}^0 \rightarrow \mathrm{K}^0) - R(\mathrm{K}^0 \rightarrow \overline{\mathrm{K}}^0)}{R(\overline{\mathrm{K}}^0 \rightarrow \mathrm{K}^0) + R(\mathrm{K}^0 \rightarrow \overline{\mathrm{K}}^0)} \right\rangle = (6.6 \pm 1.3_{\mathrm{stat}} \pm 1.0_{\mathrm{sys}}) \cdot 10^{-3}. \tag{2.7}$$

CP Violation in the Standard Model

In order to explain the observed left-right symmetry in nature, the $\mathcal{CP}$ symmetry was defined after the proof of parity violation in the weak sector of the SM. The $\mathcal{CP}$ transformation successively applies a parity transformation followed by a charge conjugation. Combining these two operations solves the meson decay issue stated above. The $\mathcal{CP}$ transformation converts a left-handed neutrino into a right-handed anti-neutrino [9, 10]. However, a violation of the $\mathcal{CP}$ symmetry in weak interactions was found within the Fitch-Cronin experiment 1964 which investigated the decay of K^0 particles [16]. The decay rates of kaons in the mass

eigenstate K_L into two and three pions were measured [17]. Considering K_L as a pure $\mathcal{CP}$ eigenstate, the decay into two pions would not be possible. Nevertheless, some of these decays were observed during the experiment, giving evidence for $\mathcal{CP}$ violation in the weak sector. This observation could be explained by adding the so called Cabibbo-Kobayashi-Maskawa (CKM) matrix to the SM [18]. It describes the mixing of the six quarks and its empirical phase δ is proportional to the $\mathcal{CP}$ violation. In general, the SM also allows for $\mathcal{CP}$ violation in strong interactions. The so called θ_{QCD} term in the QCD Lagrangian is $\mathcal{CP}$ violating but so far, no such processes were observed within the strong sector, resulting in the so called strong $\mathcal{CP}$ problem [10]. Since the $\mathcal{CP}$ violation in the CKM matrix is not sufficient to explain the matter-antimatter-asymmetry, additional sources of $\mathcal{CP}$ violation are of great interest. The EDM is one possible candidate and will be discussed in the following chapter.

2.3 Electric Dipole Moments

The EDM is a fundamental property of a particle comparable to its momentum, charge, spin or mass. The existence of a permanent EDM in a non-degenerated system could be an additional source of $\mathcal{CP}$ violation and could contribute to the understanding of the matter dominance in the Universe. This chapter briefly discusses the theoretical background of EDMs gives an overview over EDM measurements and their results.

2.3.1 Definition

In general, the EDM $\vec{d}$ is defined by the separation of positive and negative charges in a system and can therefore arise from an asymmetry of its charge density distribution $\rho(\vec{x})$:

$$\vec{d} = \int_V \rho(\vec{x})\ \vec{x}\ d\vec{x}. \tag{2.8}$$

The structure of Equation (2.8) is similar to the one of the magnetic dipole moment (MDM) defined as:

$$\vec{\mu} = \frac{1}{2} \int_V \left(\vec{x} \times \vec{j}(\vec{x}) \right)\ d\vec{x}, \tag{2.9}$$

where $\vec{j}(\vec{x})$ denotes the current density.

The EDM is aligned parallel or anti-parallel to the spin $\vec{S}$ as this is the only distinguishable quantization axis. Another independent preferred direction would result in a degenerated system since other quantum numbers would be needed

to describe the state [19]. The dependency of the EDM and MDM on the spin vector are given by

$$\vec{d} = \eta_{\text{EDM}} \frac{q}{2mc} \vec{S} \tag{2.10}$$

$$\vec{\mu} = g \frac{q}{2m} \vec{S}, \tag{2.11}$$

where q is the charge of the particle, m its mass and c the speed of light. In analogy to the so called g-factor g the dimensionless scaling parameter η_{EDM} is introduced.
As already mentioned earlier, a permanent EDM is $\mathcal{CP}$ violating as can be seen by applying a parity transformation and the charge conjugation transformation to the Hamiltonian of a particle at rest in an external magnetic $\vec{B}$ and electric $\vec{E}$ field:

$$\hat{H} = -\vec{\mu}\vec{B} - \vec{d}\vec{E} \tag{2.12}$$

$$\boldsymbol{\mathcal{P}} : \hat{H} = -\vec{\mu}\vec{B} + \vec{d}\vec{E} \tag{2.13}$$

$$\boldsymbol{\mathcal{T}} : \hat{H} = -\vec{\mu}\vec{B} + \vec{d}\vec{E}. \tag{2.14}$$

Performing the parity transformation leads to an inversion of the electric field while the magnetic field and the spin stay unchanged. Compared to the initial Hamiltonian in Equation (2.12) the sign of the EDM term changes. Therefore, a permanent EDM is $\mathcal{P}$ violating while the MDM is symmetric under the parity transformation.

The time reversal transformation changes the sign of the magnetic field and flips the direction of the spin vector. The product of both thus remains the same. Since the electric field is not affected by the transformation and the EDM points in the direction of the spin, the EDM term of Equation (2.12) changes its sign showing the $\mathcal{T}$ violation of an EDM [19, 20].
The described changes can also be seen in Figure 2.1. According to the $\mathcal{CPT}$ theorem, an EDM is therefore $\mathcal{CP}$ violating as it violates $\mathcal{P}$ as well as $\mathcal{T}$.

2.3.2 $\mathcal{CP}$ Violation and EDMs

Higher order loop effects can introduce EDMs both in the weak and the strong section of the SM. A brief overview of the relevant mechanisms and the resulting SM predictions are given in the following.

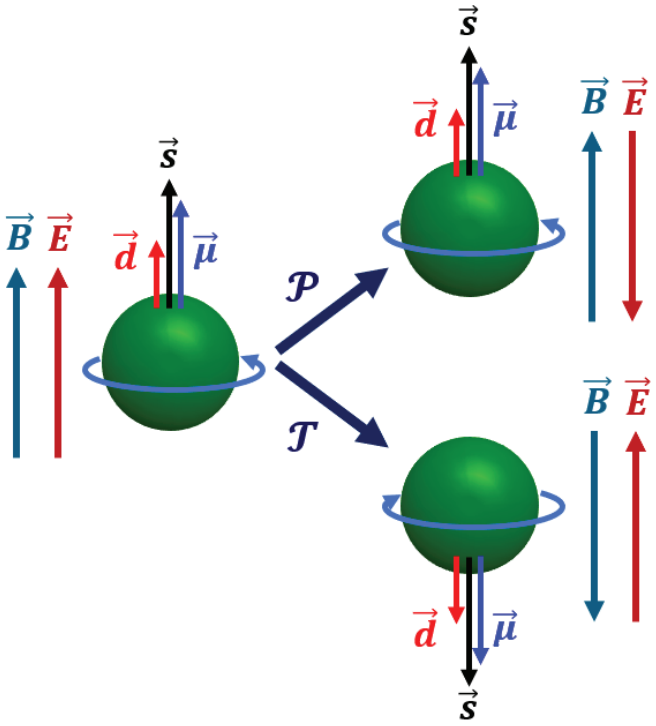

Figure 2.1: Schematic illustration of a particle in an external magnetic $\vec{B}$ and electric $\vec{E}$ field including a permanent EDM. Under a parity transformation ($\mathcal{P}$) the electric field changes its sign while the magnetic field and the spin stay unchanged. The time reversal transformation $\mathcal{T}$ in contrast flips the MDM as well as the EDM and the magnetic field changes its sign. As a result, a system with a permanent EDM violates both symmetries and is according to the $\mathcal{CPT}$ theorem also $\mathcal{CP}$ violating (adopted from [21], Figure 2.1).

As already mentioned in Section 2.2 the imaginary phase δ of the CKM matrix contributes to $\mathcal{CP}$ violation in the weak sector of the SM. The corresponding predictions for the EDMs of neutrons and electrons yield:

$$d_n \approx 10^{-32}\ e\,\mathrm{cm} \tag{2.15}$$
$$d_e \approx 10^{-40}\ e\,\mathrm{cm}. \tag{2.16}$$

These values turn out to be so tiny because the leading contribution to proton and neutron EDMs are at the three-loop level. In case of the electron the EDM is even generated on the four-loop level [22, 23].

In the strong sector of the SM the θ_{QCD} term of the Lagrangian of the QCD contributes to $\mathcal{CP}$ violation:

$$\mathcal{L}_\theta = -\theta_{QCD}\frac{g_s^2}{64\pi^2}\epsilon^{\mu\nu\alpha\beta}G^a_{\mu\nu}G^a_{\alpha\beta}, \tag{2.17}$$

where $G^a_{\mu\nu}$ denotes the gluon field tensor, ϵ describes the four dimensional Levi-Cevita tensor and g_s represents the strong coupling constant. Compared to the contributions of the weak sector, the θ_{QCD} term can lead to larger EDM values. The predictions for the neutron and the proton read [24]:

$$d_n \approx \theta_{QCD}\ (-2.9 \pm 0.9)10^{-16}\ e\,\mathrm{cm} \tag{2.18}$$

$$d_p \approx \theta_{QCD}\ (1.1 \pm 1.1)10^{-16}\ e\,\mathrm{cm}. \tag{2.19}$$

In general, θ_{QCD} can be have any value while measurements of the neutron EDM yield an upper limit of [25]

$$\theta_{QCD} < 10^{-10}. \tag{2.20}$$

The smallness of θ_{QCD} is theoretically unexplained and is often referred to as the strong $\mathcal{CP}$ problem. A possible solution could be the existence of a new particle, the so called axion which, however, could not be measured yet [26, 27].

2.3.3 Existing EDM Measurements

Since the EDM is a potential source for new $\mathcal{CP}$ violation, searches for various particles in several experiments have been performed so far. As the EDM influences the spin motion (see Equation (2.10)), the polarization of a particle ensemble turns out to be the most promising observable for EDM experiments. The main principle of these measurements for neutral systems is described in the following paragraph.

The polarization change of trapped particles is investigated in the presence of electromagnetic fields. Initially a particle sample with a polarization parallel to a main magnetic field is needed and the spins start to precess with an initial Lamor frequency. A radio-frequency (RF) magnetic field is then used to achieve a polarization that is perpendicular to the main magnetic field. In a third step, a homogeneous electric field is superimposed and interacts with the EDMs of the particles. Both, the MDM and the EDM lead to a shift in the spins precession frequency. In order to extract the pure EDM contribution the polarity of the electric field is flipped within the experiment. The difference of the resulting Lamor precession frequencies $\Delta\omega$ due to the two polarities is proportional to the EDM and can expressed as:

$$\Delta\omega = \omega(E\uparrow) - \omega(E\downarrow) = \frac{4|\vec{d}|E}{\hbar}, \tag{2.21}$$

Particle	upper EDM limit
neutron	$d_n \leq 3 \cdot 10^{-26}\ e\,\mathrm{cm}$ (90% C.L.)
electron	$d_e \leq 8.7 \cdot 10^{-29}\ e\,\mathrm{cm}$ (90% C.L.)
proton	$d_p \leq 7.9 \cdot 10^{-25}\ e\,\mathrm{cm}$ (95% C.L.)
muon	$d_\mu \leq 1.9 \cdot 10^{-19}\ e\,\mathrm{cm}$ (95% C.L.)

Table 2.1: Measured upper limits for the EDM of different particles [25, 29, 30, 31].

where the arrows indicate the different polarities of the electric field and $\hbar$ denotes the reduced Planck constant. It can be measured by introducing another RF magnetic field after the interaction with the electric field. The resulting vertical polarization serves as a measure for the EDM and is necessary to deduce the frequency difference in Equation (2.21).

The first measurement for the neutron EDM was published in 1957 by Smith, Ramsey and Purcell, yielding a value of [28]:

$$d_n = (0.1 \pm 2.4) \cdot 10^{-20}\ e\,\mathrm{cm}. \tag{2.22}$$

There are several theories of physics beyond the SM that include EDMs and can therefore make predictions for the EDMs of different particles. In order to investigate these theories and to compare the predictions to experimental data, it is necessary to measure the EDM not only for the neutron but for several other particles. In this context, it is crucial for the experiments to reach very high sensitivities since the EDM values are extremely small and can easily be dominated by systematic uncertainties. Up to now, all measurements only give upper limits for the EDM since the values are in agreement with zero. Upper bounds for the EDM of the most studied particles are summarized in Table 2.1. It's important to note that the given limits for the proton and the electron are achieved by indirect measurements of atoms and molecules. Therefore, the determination of these numbers includes assumptions about how nuclei behave within these systems [32]. The muon EDM instead was derived from a direct measurement using μ^+ and μ^- beams at the g-2 experiment at the Brookhaven National Laboratory (BNL). So far it is the only direct EDM experiment using charged particles. Further experiments for heavy nuclei, such as deuterons, are planned for the near future [33, 34].

Trapping particles and investigating them under the influence of electromagnetic fields gets more complicated as soon as the particles are charged. Charged particles are accelerated in the presence of electric fields and can't be trapped as easily as neutral particles like the neutron. Therefore, new measurement methods have to be introduced [35]. Storage rings offer the useful property that they can store

charged particles and circulating them with for very long beam lifetimes. Details will be discussed in the next section.

3. Beam Dynamics in Storage Rings

Understanding the behavior of particles moving inside an accelerator is essential when considering EDM experiments in storage rings. In this chapter the fundamental forces induced by magnetic and electric elements as well as the equations of motion of particles being stored are motivated and discussed. Furthermore, the effect of field errors and misalignments of magnets are shown. The descriptions and equations are mainly taken from [36], [37] and [38].

3.1 Lorentz Force

In the presence of electric and magnetic fields, a particle with charge q and mass m is accelerated or stored and its change in momentum $\vec{p}$ is described by the Lorentz force:

$$F_L = \frac{d\vec{p}}{dt} = q(\vec{E} + c\vec{\beta} \times \vec{B}), \tag{3.1}$$

where $\vec{E}$ and $\vec{B}$ are the electric field and magnetic field respectively and $c\vec{\beta}$ denotes the velocity of the particle. This relation is used to guide and focus the particles in an accelerator or storage ring. Common storage rings use magnetic fields to guide the beam since equivalent electric fields need to be larger by a factor of c in case of relativistic particles. Such high electric fields are technically much harder to achieve which lead to an almost exclusive use of magnetic bending elements in the past. Acceleration of particles in the longitudinal direction instead can only be achieved by using electric fields since transverse magnetic field do not contribute to the longitudinal momentum change.

3.2 Coordinate System

The motion of particles inside a storage ring has to be described relative to a predefined coordinate system. Usually, the positions of elements in an accelerator are fixed and have static fields. Instead of using the time parameter t as an independent variable it is therefore convenient in accelerator physics to express the position and other beam quantities as a function of the position s along the reference trajectory $\vec{r}_{\mathrm{ref}}(s)$. In order to describe the motion of an arbitrary particle inside the accelerator, a reference particle is defined which moves on the reference orbit $\vec{r}_{ref}(s)$ with the reference momentum of the beam $\vec{p}_{ref}$. Using a

co-moving coordinate system $(\vec{e}_x, \vec{e}_y, \vec{e}_s)$, the motion of an arbitrary particle with respect to the reference particle can be studied. The origin of this coordinate system is located at the position of the reference particle. Figure 3.1 illustrates such a co-moving coordinate system from an initial point s_A to a final point s_B on the reference orbit. The basis vector $\vec{e}_s$ is always aligned with the momentum of the reference particle $\vec{p}_{ref}$. The transverse plane is described by the basis vectors $\vec{e}_x$, being perpendicular to $\vec{e}_s$ and pointing in radial direction, and $\vec{e}_y = \vec{e}_s \times \vec{e}_x$ in vertical direction.

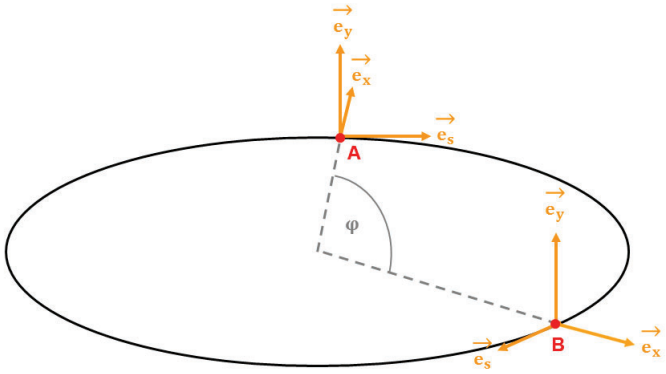

Figure 3.1: Co-moving Cartesian coordinate system with its origin located at the position of the reference particle. The s-axis is tangential to the reference orbit, the x-axis points in radial direction and y denotes the vertical direction. The coordinates (x,y,s) are called curvilinear coordinates [39].

The transformation of the coordinate system from one point s_A to another s_B is then given by:

$$\vec{e}_{x,B} = \vec{e}_{x,A}\cos(\theta) + \vec{e}_{s,A}\sin(\theta), \tag{3.2}$$
$$\vec{e}_{y,B} = \vec{e}_{y,A}, \tag{3.3}$$
$$\vec{e}_{s,B} = -\vec{e}_{x,A}\sin(\theta) + \vec{e}_{s,A}\cos(\theta), \tag{3.4}$$

with

$$\theta = \int_A^B \frac{\mathrm{d}s}{\rho(s)}, \tag{3.5}$$

where $\rho(s)$ denotes the bending radius. The change of the unit vectors over time is given by

$$\dot{\vec{e}}_x = \frac{\mathrm{d}\vec{e}_x}{\mathrm{d}\theta}\frac{\mathrm{d}\theta}{\mathrm{d}t} = \frac{1}{\rho}\dot{s}\vec{e}_s, \tag{3.6}$$

$$\dot{\vec{e}}_y = 0, \tag{3.7}$$

$$\dot{\vec{e}}_s = \frac{\mathrm{d}\vec{e}_s}{\mathrm{d}\theta}\frac{\mathrm{d}\theta}{\mathrm{d}t} = -\frac{1}{\rho}\dot{s}\vec{e}_x. \tag{3.8}$$

To describe the trajectory of a particle $\vec{r}(s)$ in the beam it is thus sufficient to know its position with respect to the trajectory of the reference particle $\vec{r}_0(s)$. Using the transverse deviations from the reference orbit of a single particle $x(s)$ and $y(s)$, its trajectory can be parametrized as

$$\vec{r}(s) = \vec{r}_0(s) + x(s)\vec{e}_x(s) + y(s)\vec{e}_y(s). \tag{3.9}$$

3.3 Transverse Motion

Within this section, the transverse equations of motion are derived and discussed. Furthermore, field error effects are described and an orbit correction method is introduced.

3.3.1 Equations of Motion

In this section the equations of motion of a particle passing the magnetic structure of an accelerator will be derived. Equation (3.9) describes the general trajectory of a particle relative to the reference orbit.
To formulate the equations of motion, the time derivatives of $r(s)$ are needed. Using Equations (3.6) to (3.8) yields

$$\dot{\vec{r}}(s) = \dot{x}\vec{e}_x + \dot{y}\vec{e}_y + \left(1 + \frac{x}{\rho}\right)\dot{s}\vec{e}_s, \tag{3.10}$$

$$\ddot{\vec{r}}(s) = \left[\ddot{x} - \left(1 + \frac{x}{\rho}\right)\frac{\dot{s}^2}{\rho}\right]\vec{e}_x + \ddot{y}\vec{e}_y + \left[\frac{2}{\rho}\dot{x}\dot{s} + \left(1 + \frac{x}{\rho}\right)\ddot{s}\right]\vec{e}_s. \tag{3.11}$$

At every point in time the position s on the path through the accelerator is uniquely determined and can therefore be used as the independent variable.
Hence time derivatives can be transformed into derivatives with respect to s resulting in

$$\dot{\vec{r}}(s) = x'\dot{s}\vec{e}_x + y'\dot{s}\vec{e}_y + \left(1 + \frac{x}{\rho}\right)\dot{s}\vec{e}_s, \tag{3.12}$$

$$\ddot{\vec{r}}(s) = \left[x''\dot{s}^2 + x'\ddot{s} - \left(1+\frac{x}{\rho}\right)\frac{\dot{s}^2}{\rho}\right]\vec{e}_x + \left(y''\dot{s}^2 + y'\ddot{s}\right)\vec{e}_y + \left[\frac{2}{\rho}x'\dot{s}^2 + \left(1+\frac{x}{\rho}\right)\ddot{s}\right]\vec{e}_s. \quad (3.13)$$

The Lorentz force (Equation (3.1)) acts on particles traversing electromagnetic fields. Assuming a pure magnetic accelerator it reduces to

$$m\ddot{\vec{r}}(s) = q\big(\dot{\vec{r}}(s) \times \vec{B}\big). \quad (3.14)$$

Further assuming only vertical magnetic fields[1] and using Equation (3.14) it follows that

$$\ddot{\vec{r}}(s) = \frac{q}{m}\begin{pmatrix} -\big(1+\frac{x}{\rho}\big)\dot{s}B_y \\ \big(1+\frac{x}{\rho}\big)\dot{s}B_x \\ x'\dot{s}B_y - y'\dot{s}B_x \end{pmatrix}. \quad (3.15)$$

For relativistic particles the relative change of the longitudinal velocity in magnetic fields is small and can be neglected. Comparing the vertical components of the Equations (3.15) and (3.13) leads to the equations of motion

$$x''\dot{s}^2 + x'\ddot{s} - \left(1+\frac{x}{\rho}\right)\frac{\dot{s}^2}{\rho} = -\frac{q}{m}\left(1+\frac{x}{\rho}\right)\dot{s}B_y \quad (3.16)$$

for the horizontal direction and

$$y''\dot{s}^2 + y'\ddot{s} = \frac{q}{m}\left(1+\frac{x}{\rho}\right)\dot{s}B_x \quad (3.17)$$

for the vertical components.
In order to further simplify the equations, the change in velocity in the magnetic fields is assumed to happen slowly ($\ddot{s} \approx 0$) and the velocity of an arbitrary particle in the beam can be expressed via

$$v = \dot{s}\,\frac{\rho + x}{\rho} = \dot{s}\left(1+\frac{x}{\rho}\right), \quad (3.18)$$

as can easily be deduced from Figure 3.2.
Using $\ddot{s} \approx 0$ and $p = mv$, Equations (3.16) and (3.17) turn into the simplified equations of motion, given by

$$x'' - \left(1+\frac{x}{\rho}\right)\frac{1}{\rho} = -\frac{q}{p}\left(1+\frac{x}{\rho}\right)^2 B_y, \quad (3.19)$$

[1] This assumption is true for most particle accelerators.

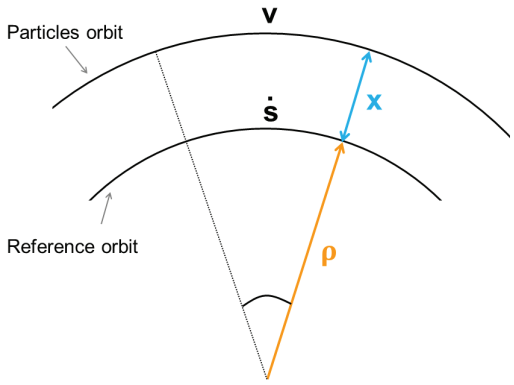

Figure 3.2: The velocity of an arbitrary particle in the beam is not equal to the velocity of the reference particle. It is larger (smaller) for particles that move on an outer (inner) path relative to the reference particle. Adapted from [36].

$$y'' = \frac{q}{p}\left(1 + \frac{x}{\rho}\right)^2 B_x. \tag{3.20}$$

The momenta of the particles in the beam may generally deviate from the reference momentum p_0. These deviations Δp are usually in the order of less than 1 % in which case one can use a linear approximation for the inverse of the momentum

$$\frac{1}{p} = \frac{1}{p_0 + \Delta p} = \frac{1}{p_0}\left(1 - \frac{\Delta p}{p_0}\right) + \mathcal{O}(\Delta p^2). \tag{3.21}$$

The magnetic fields of an accelerator can be expressed using the field expansion:

$$\frac{q}{p}B_y(x) = \frac{q}{p}B_{y0} + \frac{q}{p}\frac{\mathrm{d}B_y}{\mathrm{d}x}\,x + \frac{1}{2!}\frac{q}{p}\frac{\mathrm{d}^2B_y}{\mathrm{d}x^2}\,x^2 + \frac{1}{3!}\frac{q}{p}\frac{\mathrm{d}^3B_y}{\mathrm{d}x^3}\,x^3 + \mathcal{O}(x^4) \tag{3.22}$$

$$= \underbrace{\frac{1}{\rho}}_{\text{Dipole}} + \underbrace{kx}_{\text{Quadrupole}} + \underbrace{\frac{1}{2!}mx^2}_{\text{Sextupole}} + \underbrace{\frac{1}{3!}ox^3}_{\text{Octupole}} + \mathcal{O}(x^4), \tag{3.23}$$

where $\frac{1}{\rho}$ $(k,\ m,\ o)$ represents the magnet strength of the dipoles (quadrupoles, sextupoles, octupoles). By convention a quadrupole is focusing if its strength k is negative and it has a defocusing effect if k is positive. Assuming the beam is bend only in the horizontal plane, the magnetic fields in each direction can be written as

$$\frac{q}{p_0}B_y = \frac{1}{\rho} - kx, \tag{3.24}$$

$$\frac{q}{p_0}B_x = -ky. \tag{3.25}$$

Replacing the respective terms in the equations of motion (3.19) and (3.20) in horizontal and vertical direction by Equations (3.21), (3.24) and (3.25), one ends up with

$$x'' - \Big(1+\frac{x}{\rho}\Big)\frac{1}{\rho} = -\Big(1+\frac{x}{\rho}\Big)^2\Big(\frac{1}{\rho} - kx\Big)\Big(1-\frac{\Delta p}{p_0}\Big), \tag{3.26}$$

$$y'' = -\Big(1+\frac{x}{\rho}\Big)^2 ky\,\Big(1-\frac{\Delta p}{p_0}\Big). \tag{3.27}$$

Since the transverse deviations from the reference orbit x and y are supposed to be much smaller than the bending radius ρ and the relative momentum deviation is much smaller than one ($\frac{\Delta p}{p_0} << 1$) , quadratic terms in x, y and $\frac{\Delta p}{p_0}$ can be neglected after multiplying out the terms in Equations 3.26 and 3.27.
Assuming a purely magnetic storage ring consisting only of dipoles and quadrupoles with only vertical magnetic fields the equations of motion for a particle traversing the magnetic structure are given by

$$x''(s) + \Big(\frac{1}{\rho^2(s)} - k(s)\Big)x(s) = \frac{1}{\rho(s)}\frac{\Delta p}{p_0}, \tag{3.28}$$

$$y''(s) + k(s)y(s) = 0. \tag{3.29}$$

Ignoring dispersive effects. i.e. $\frac{\Delta p}{p_0} = 0$, the equations of motion (3.28) and (3.29) become second order homogeneous differential equations of the form

$$x''(s) + K(s)\; x(s) = 0, \tag{3.30}$$

$$y''(s) + k(s)\; y(s) = 0, \tag{3.31}$$

with

$$K(s) = \frac{1}{\rho^2(s)} - k(s). \tag{3.32}$$

Equations (3.30) and (3.31) are known as *Hill's differential equations*.
Since both equations are structurally identical and they can be solved using the same method, it is sufficient to only consider the solution in horizontal direction. The vertical solution can then be found analogously. Except for the s dependent coefficient $K(s)$ which is periodic over one turn with a length of C, i.e. $K(s+C) = K(s)$, the differential equation resembles the one of a harmonic oscillator. For

simplicity the s dependence will not be explicitly mentioned in every step in the following calculations. By analogy with the harmonic oscillator the ansatz

$$x(s) = A\ u(s)\cos[\Psi(s) + \Psi_0] \tag{3.33}$$

can be made, where A and Ψ_0 are the constants of integration defining the trajectory of an individual particle. Inserting Equation (3.33) into Equation (3.30) leads to

$$\underbrace{(u'' - u\Psi'^2 + uK)}_{\text{I}}\cos(\Psi + \Psi_0) - \underbrace{(2u'\Psi' + u\Psi'')}_{\text{II}}\sin(\Psi + \Psi_0) = 0. \tag{3.34}$$

Independently of each other, terms I and II must vanish for Equation (3.34) to hold. Thus

$$u'' - u\Psi'^2 + uK = 0 \tag{3.35}$$

and

$$2u'\Psi' + u\Psi'' = 0. \tag{3.36}$$

Integrating Equation (3.36) twice yields

$$\Psi'(s) = \frac{1}{u^2} \tag{3.37}$$

and

$$\Psi(s) = \int_0^s \frac{\mathrm{d}s'}{u^2(s')}. \tag{3.38}$$

Inserting Equation (3.37) into Equation (3.35) the differential equation for $u(s)$ can finally be written as

$$u''(s) + K(s)u(s) = \frac{1}{u^3(s)}, \tag{3.39}$$

which has a uniquely defined periodic solution $u(s)$. Introducing the betatron function $\beta(s)$ with

$$\beta(s) = u^2(s) \tag{3.40}$$

the general solution of Hill's differential equation are pseudo-harmonic oscillations, so called betatron oscillations, about the reference orbit with an s dependent amplitude given by

$$x(s) = A\sqrt{\beta(s)}\ \cos[\Psi(s) + \Psi_0] \tag{3.41}$$

and

$$x'(s) = \frac{A}{\sqrt{\beta(s)}}\left[\underbrace{\frac{1}{2}\beta'(s)}_{:=-\alpha(s)}\cos[\Psi(s) + \Psi_0] - \sin[\Psi(s) + \Psi_0]\right]. \tag{3.42}$$

The parameter A denotes the amplitude of the oscillation and Ψ_0 indicates the initial phase. The betatron function $\beta(s)$ depends on the magnetic structure of the accelerator and can be interpreted as a measure of the transverse beam profile. The betatron tune, defined as the number of betatron oscillations per turn, is calculated as

$$Q = \frac{1}{2\pi}\int_s^{s+C} \Psi' \mathrm{d}s = \frac{1}{2\pi}\int_s^{s+C} \frac{\mathrm{d}s'}{\beta(s)}. \tag{3.43}$$

The particles thus perform oscillations about the reference orbit. The oscillation amplitude is dependent on the magnetic structure $\beta(s)$ and on the integration constant A. It is different for each particle as A is an intrinsic quantity of a particle as will be discussed in the following section.

Courant-Snyder Invariant and Phase Space Ellipse

Using the general solution for the transverse motion of a particle from Equation (3.41) one can find a description of the particle motion in the two-dimensional phase space defined by the coordinates x and x'. Therefore the Ψ dependent terms in Equation (3.42) must be eliminated. From Equation (3.41) one finds

$$\cos[\Psi(s) + \Psi_0] = \frac{x(s)}{A\sqrt{\beta(s)}}. \tag{3.44}$$

Substituting this term into Equation (3.42) leads to

$$\sin[\Psi(s) + \Psi_0] = \frac{\sqrt{\beta(s)}x'(s)}{A} + \frac{\alpha(s)x(s)}{A\sqrt{\beta(s)}}. \tag{3.45}$$

From $\sin^2(s) + \cos^2(s) = 1$ and Equation (3.41) it follows that

$$\frac{x^2(s)}{\beta(s)} + \left(\frac{\alpha(s)x(s)}{\sqrt{\beta(s)}} + \sqrt{\beta(s)}x'(s)\right)^2 = A^2 = \epsilon, \tag{3.46}$$

where $\epsilon = A^2$, is the so called Courant-Snyder invariant or emittance [36]. This invariant is a characteristic property of a single particle and independent of the magnetic structure of the accelerator. The particle with the largest emittance defines the envelope $E(s)$ of the beam since the amplitude of the betatron oscillations is given by $\sqrt{\epsilon\beta(s)}$. A sketch of the transverse motion of particles inside the boundaries of the envelope is shown in Figure 3.3.
Defining

$$\gamma(s) := \frac{1 + \alpha^2(s)}{\beta(s)}, \tag{3.47}$$

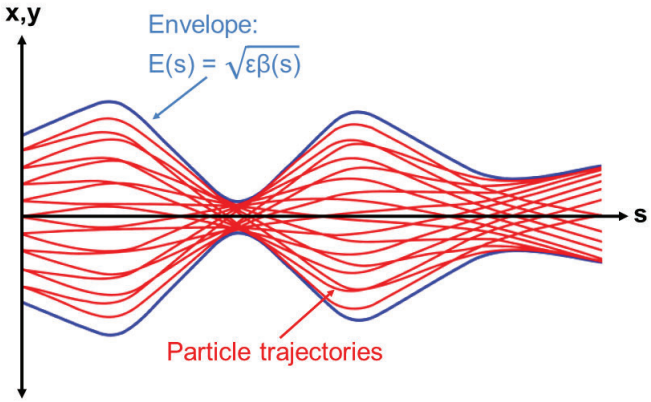

Figure 3.3: The transverse motion of all particles in the beam is limited by the particle with the largest emittance. Its trajectory along the ring forms the envelope for all other particles. Adapted from [[36], [39]].

Equation (3.46) reads

$$\gamma(s)x^2(s) + 2\alpha(s)x(s)x'(s) + \beta(s)x'^2(s) = \epsilon. \tag{3.48}$$

This equation describes an ellipse with a constant enclosed area of ($F = \pi\epsilon =$ const.). The form of the ellipse is defined by the optical functions $\alpha(s), \beta(s)$ and $\gamma(s)$ and is therefore a function of s. The area of the phase space ellipse however stays constant due to *Liouville's theorem* [40] whose underlying conditions are generally fulfilled in accelerators. A phase space ellipse defined by a particle with a given Courant-Snyder invariant ϵ describes the phase space behavior of all particles with a betatron amplitude smaller than $\sqrt{\epsilon}$. Figure 3.4 illustrates a phase space ellipse at a fixed position s and for a given emittance ϵ.

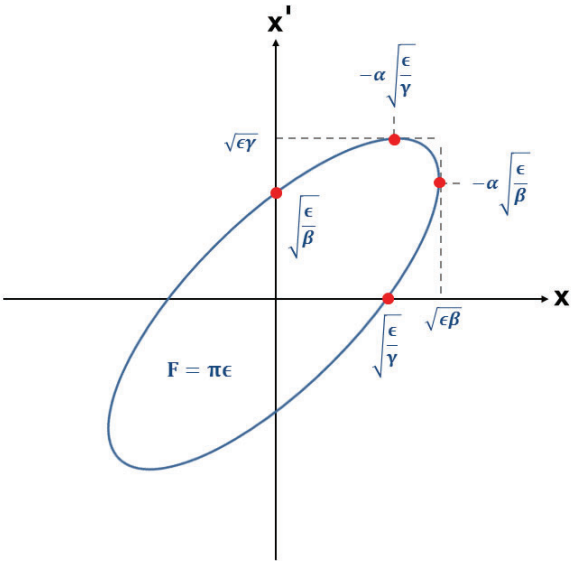

Figure 3.4: The phase space of a linear transverse particle motion is described by an ellipse with constant area, dependent on the Courant-Snyder invariant of the particle. Along the magnetic structure of the ring, the ellipse rotates in the coordinate system but its size and form stays unchanged. Adapted from [[37], [39]].

3.4 Longitudinal Motion

So far, only the transverse motion of particles inside a storage ring was discussed. The longitudinal motion is mainly influenced by the accelerating cavity providing a longitudinally oscillating electric field. For a stable operation with a constant mean momentum, it is necessary that the circulating particles arrive at a fixed phase relative to the accelerating voltage. The frequency of the accelerating field thus is an integer multiple of the particles revolution frequency. In case of a synchrotron, the field inside the cavity as well as the magnetic fields are increased synchronously with the particle energy. Since the EDM experiment at COSY requires a bunched beam [41], the revolution frequency after reaching the final energy is constant. Therefore, momentum deviations lead to orbit lengthening effects which will be discussed below.

In general the change in the revolution frequency Δf due to the path lengthening ΔL or changes in the velocity Δv can be written as:

$$\frac{\Delta f}{f_0} = \frac{\Delta L}{L_0} - \frac{\Delta v}{v_0}, \tag{3.49}$$

where the reference quantities are indicated by the subscript 0. The orbit lengthening due to momentum deviations can be expressed using the momentum compaction factor which is defined as

$$\alpha_p = \frac{1}{L_0}\int_0^{L_0} \frac{D(\tilde{s})}{\rho(\tilde{s})}\mathrm{d}\tilde{s}. \tag{3.50}$$

Using the relation [36]

$$\Delta L = \frac{\Delta p}{p_0}\oint \frac{D(s)}{\rho_x(s)}\mathrm{d}s \tag{3.51}$$

results in

$$\frac{\Delta L}{L_0} = \alpha_p \frac{\Delta p}{p_0}. \tag{3.52}$$

The relative velocity change can also be expressed in terms of momentum deviations which reads

$$\frac{\Delta v}{v_0} = \frac{1}{\gamma_0^2}\frac{\Delta p}{p_0}. \tag{3.53}$$

Combining Equations (3.49), (3.52) and (3.53) results in

$$\frac{\Delta f}{f_0} = \left(\alpha_p - \frac{1}{\gamma_0^2}\right)\frac{\Delta p}{p_0} = \eta\frac{\Delta p}{p_0}, \tag{3.54}$$

where η is the so called phase slip factor.

In the following the longitudinal motion of an arbitrary particle with respect to the synchronous particle will be motivated. For the longitudinal motion the energy gain per revolution of the synchronous particle can be written as

$$\Delta E_s = qU_0\sin(\phi_s), \tag{3.55}$$

where ϕ_s is the phase where the reference particle is supposed to enter the cavity. A deviation $\Delta\phi = \phi - \phi_s$ from this reference phase leads to oscillations of a given arbitrary particle in the longitudinal phase space according to the differential equation [38].

$$\frac{\mathrm{d}^2}{\mathrm{d}t}\Delta\phi + \frac{h\eta_s\omega_s^2}{2\pi p_s v_s}qU_0\cos(\phi_s)\Delta\phi = \frac{\mathrm{d}^2}{\mathrm{d}t}\Delta\phi + \omega_{\mathrm{syn}}^2\Delta\phi = 0. \tag{3.56}$$

The particle oscillates with the frequency $f_{\mathrm{syn}} = \omega_{\mathrm{syn}}/2\pi$ and the number of synchrotron oscillations per turn is given by

$$Q_{\mathrm{syn}} = \frac{\omega_{\mathrm{syn}}}{\omega_s}. \tag{3.57}$$

4. Spin Dynamics in Storage Rings

As discussed previously, the EDM experiment in Jülich is conducted using a polarized beam. An understanding of the spin motion in electromagnetic fields is therefore crucial. The following chapter thus discusses the equation of motion of spins inside storage rings. With regard to the precursor experiment, the discussion concentrates on purely magnetic machines. Finally, the chapter motivates various EDM measurement setups with different combinations of electromagnetic fields. The following information is mainly taken from [42, 43, 44].

4.1 Polarization

The polarization is defined as the average spin orientation of a particle ensemble. A single spin of a particle can be described by an operator $\hat{\vec{S}}$ such that the projection of the spin angular momentum along the specified quantization axis is given by $S_z = m_s\hbar$. The associated spin quantum number m_s can take $(2s+1)$ values and ranges from $-s$ to s, where s is the spin number of the particle [45]. In the following a Cartesian coordinate system is assumed and the spin quantization axis is chosen to be along the z-axis.

4.1.1 Spin-$\frac{1}{2}$ Particles

A spin-$\frac{1}{2}$ particle ($s = \frac{1}{2}$) can only be in the states $m_s = \pm\frac{1}{2}$. The state of such a particle can be expressed by a normalized Pauli spinor:

$$\chi = \begin{pmatrix} u \\ d \end{pmatrix}, \tag{4.1}$$

with $|u|^2 + |d|^2 = 1$ and the two possible spin states m_s correspond to the two spinor components. From quantum mechanics it is known that each observable is linked to an hermitian operator $\hat{A}$ and that an observable is defined as the expectation value of the observable is defined as

$$\langle A \rangle = \langle \chi | \hat{A} | \chi \rangle = \chi^\dagger \hat{A} \chi. \tag{4.2}$$

Using the density matrix

$$\rho = |\chi\rangle\langle\chi| = \begin{pmatrix} |u|^2 & ud^* \\ u^*d & |d|^2 \end{pmatrix} \tag{4.3}$$

one can write the observable as

$$\langle A \rangle = \mathrm{Tr}\rho\hat{A}. \tag{4.4}$$

The hermitian operators corresponding to the spin observable are the Pauli matrices σ_i. Thus the spin operator reads

$$\hat{\vec{S}} = \frac{\hbar}{2}\vec{\sigma}, \tag{4.5}$$

where

$$\sigma_1 = \begin{pmatrix} 0 & 1 \\ 1 & 0 \end{pmatrix}, \quad \sigma_2 = \begin{pmatrix} 0 & -i \\ i & 0 \end{pmatrix}, \quad \sigma_3 = \begin{pmatrix} 1 & 0 \\ 0 & -1 \end{pmatrix}. \tag{4.6}$$

Together with the unity matrix $\sigma_0 = \mathbb{1}$ the Pauli matrices form a complete basis of the space of the hermitian 2×2-matrices. The spin vector $\vec{S} = (S_x, S_y, S_z)$ is defined as the expectation value of the spin operator and can be written as:

$$\vec{S} = \langle \hat{\vec{S}} \rangle = \frac{\hbar}{2}\mathrm{Tr}\rho\vec{\sigma} = \frac{\hbar}{2}\begin{pmatrix} 2\ \mathrm{Re}(ud^*) \\ 2\ \mathrm{Im}(ud^*) \\ |u|^2 - |d|^2 \end{pmatrix}. \tag{4.7}$$

Changing from a single particle to an ensemble of N particles the quantity of interest is now the expectation value of the spin observables of this ensemble. In this case the density matrix has to be extended to:

$$\rho = \frac{1}{N}\begin{pmatrix} \sum_{i=1}^{N} |u^{(i)}|^2 & \sum_{i=1}^{N} u^{(i)}d^{(i)*} \\ \sum_{i=1}^{N} u^{(i)*}d^{(i)} & \sum_{i=1}^{N} |d^{(i)}|^2 \end{pmatrix} = \frac{1}{2}\Big(\sigma_0 + \vec{P}\vec{\sigma}\Big), \tag{4.8}$$

where the density matrix is expressed in terms of the Pauli spin operators in the last step. Here, $\vec{P}$ denotes the polarization vector that is defined as the average of all expectation values of the spin operators in the ensemble:

$$\vec{P} = \frac{1}{N}\sum_{i=1}^{N} \vec{S}_i. \tag{4.9}$$

Assuming an ensemble with N^+ particles of quantization state $m = +\frac{1}{2}$ and N^- particles in quantization state $m = -\frac{1}{2}$, the vector polarization is defined as:

$$P_V = \frac{N^+ - N^-}{N^+ + N^-}. \tag{4.10}$$

The beam is therefore fully polarized if the vector polarization is ± 1 and fully unpolarized if $P_V = 0$.

4.1.2 Spin-1 Particles

A spin-1 particle can have three different states: $m = -1$, $m = 0$ or $m = 1$. It is therefore described by a three-dimensional spinor:

$$\chi = \begin{pmatrix} a_1 \\ a_2 \\ a_3 \end{pmatrix}. \tag{4.11}$$

In this case the three spin operators read:

$$\hat{S}_1 = \frac{\hbar}{\sqrt{2}} \begin{pmatrix} 0 & 1 & 0 \\ 1 & 0 & 1 \\ 0 & 1 & 0 \end{pmatrix}, \quad \hat{S}_2 = \frac{\hbar}{\sqrt{2}} \begin{pmatrix} 0 & -i & 0 \\ i & 0 & -i \\ 0 & i & 0 \end{pmatrix}, \quad \hat{S}_3 = \hbar \begin{pmatrix} 1 & 0 & 0 \\ 0 & 0 & 0 \\ 0 & 0 & -1 \end{pmatrix}. \tag{4.12}$$

The space of hermitian 3×3 matrices requires a basis of nine matrices. Taking the identity matrix (I) into account, five matrices are missing which can be defined in the standard Cartesian notations as

$$\hat{S}_{ij} = \frac{3}{2}\left(\hat{S}_i \hat{S}_j + \hat{S}_j \hat{S}_i\right) - 2I\delta_{ij}, \quad i, j \in 1, 2, 3. \tag{4.13}$$

In total this results in ten operators where only nine of them are independent and the dependency relation is given by

$$\hat{S}_{11} + \hat{S}_{22} + \hat{S}_{33} = 0 \tag{4.14}$$

and commonly the basis operators $\hat{S}_i$ are normalized according to

$$\mathrm{Tr}\hat{S}_i \hat{S}_j = 3\delta_{ij}. \tag{4.15}$$

Using the above operators, the density matrix for an ensemble of spin-1 particles can be expressed as

$$\rho = \frac{1}{3}\left[I + \frac{3}{2}\sum_{i=1}^{3} P_i S_i + \frac{1}{3}\sum_{i=1}^{3}\sum_{j=1}^{3} P_{ij} S_{ij}\right], \quad \text{with} \quad P_{ij} = P_{ji}, \tag{4.16}$$

where the parameters P_i and P_{ij} denote polarization states of the spin-1 particle. Considering an ensemble with N^+ particles of quantization state $m = +1$, N^0 particles with $m = 0$ and N^- particles in quantization state $m = -1$, the vector polarization P_V and tensor polarization P_T along the quantization axis are defined as

$$P_V = \frac{N^+ - N^-}{N^+ + N^0 + N^-}, \tag{4.17}$$

$$P_T = \frac{N^+ + N^- - 2N^0}{N^+ + N^0 + N^-}. \tag{4.18}$$

Since the polarization of a spin-1 particle beam is always a combination of vector and tensor polarization, the maximum values that can be achieved are:

$$(P_V, P_T) = \Big(\pm\frac{2}{3}, 0\Big) \quad \text{or} \quad (P_V, P_T) = \Big(\pm\frac{1}{3}, \pm 1\Big). \tag{4.19}$$

4.2 Spin Motion in Storage Rings

After the general definition of the polarization this chapter will describe the behavior of the polarization under the influence of electric and magnetic fields. Therefore, the equation of motion of spins in electromagnetic fields is motivated and discussed and spin transfer matrices are introduced. Finally, different EDM experiment methods are described.

4.2.1 Spin Motion in the Particle Rest Frame

The interaction of the spin with electromagnetic fields in the rest frame of a given particle was already given by the Hamiltonian in Equation (2.12). The corresponding non-relativistic equation of motion for the spin $\vec{S}$ in the presence of electric and magnetic fields is given by:

$$\frac{\mathrm{d}\vec{S}}{\mathrm{d}t} = \vec{\Omega} \times \vec{S} = \vec{\mu} \times \vec{B} + \vec{d} \times \vec{E}, \tag{4.20}$$

where the expressions for the MDM $\vec{\mu}$ and EDM $\vec{d}$ are given in Equations (2.11) and (2.10). Equation (4.20) describes a spin precession in the plane perpendicular to $\vec{\Omega}$ with an angular frequency of $|\vec{\Omega}|$. The MDM values for hadronic systems are usually expressed in terms of the nuclear magneton

$$\vec{\mu}_N = 3.1524512550(15) \cdot 10^{-8}\mathrm{eV/T}. \tag{4.21}$$

A given particle with velocity $\vec{v}$ will precess in a magnetic field with angular frequency $\vec{\Omega}_{cyc}$. The relative frequency difference between particle and spin precession is the gyromagnetic anomaly

$$G = \frac{g-2}{2} = \frac{|\vec{\Omega}_{cyc}| - |\vec{\Omega}|}{\vec{\Omega}_{cyc}}. \tag{4.22}$$

Particle	Gyromagnetic anomaly G
proton	$1.792847351 \pm 0.000000009$
deuteron	$-0.1429872724 \pm 0.0000000015$

Table 4.1: Measured values of the gyromagnetic anomaly of the proton and the deuteron.

At lowest order in perturbation theory, Dirac particles have a g factor of exactly 2 and a vanishing gyromagnetic anomaly. However, higher order corrections lead to a non-vanishing values of G and can be measured within the $g-2$ experiment [46]. The measured values for the gyromagnetic anomaly for protons and deuterons are given in Table 4.1.

4.2.2 The Thomas-BMT Equation

For common accelerator setups, the electromagnetic fields in the laboratory system are known. However, the fields in Equation (4.20) are given in the rest frame of the particle. Using a Lorentz transformation, the spin equation of motion can be expressed by magnetic and electric fields in the laboratory system, whereas the spin is still defined in the particles rest frame. The resulting equation is the so called Thomas-Bargmann-Michel-Telegdi (T-BMT) equation which can be extended in order to include the EDM effect and ultimately reads [47, 48, 49]:

$$\frac{d\vec{S}}{dt} = \vec{\Omega} \times \vec{S} = (\vec{\Omega}_{\mathrm{MDM}} + \vec{\Omega}_{\mathrm{EDM}}) \times \vec{S} \quad \text{where} \tag{4.23}$$

$$\vec{\Omega}_{\mathrm{MDM}} = -\frac{q}{m}\left[G\vec{B} - \frac{\gamma G}{\gamma+1}\vec{\beta}(\vec{\beta}\cdot\vec{B}) - \left(G - \frac{1}{\gamma^2-1}\right)\frac{\vec{\beta}\times\vec{E}}{c}\right], \tag{4.24}$$

$$\vec{\Omega}_{\mathrm{EDM}} = -\frac{q}{mc}\frac{\eta_{\mathrm{EDM}}}{2}\left[\vec{E} - \frac{\gamma}{\gamma+1}\vec{\beta}(\vec{\beta}\cdot\vec{E}) + c\vec{\beta}\times\vec{B}\right]. \tag{4.25}$$

One can also express the rotation due to the MDM in terms of perpendicular and parallel field components with respect to the momentum vector:

$$\vec{\Omega}_{\mathrm{MDM}} = \vec{\Omega}_{B_\perp} + \vec{\Omega}_{B_\parallel} + \vec{\Omega}_{E_\perp} \tag{4.26}$$

$$= -\frac{q}{\gamma m}\left[(1+G\gamma)\vec{B}_\perp + (1+G)\vec{B}_\parallel - \left(G\gamma + \frac{\gamma}{\gamma+1}\right)\vec{\beta}\times\frac{\vec{E}}{c}\right]. \tag{4.27}$$

The momentum itself precesses under the influence of electromagnetic fields with the angular frequency $\vec{\Omega}_{\mathrm{cyc}}$ and the corresponding equation of motion reads:

$$\frac{\mathrm{d}\vec{p}}{\mathrm{d}t} = \vec{\Omega}_{\mathrm{cyc}} \times \vec{p}, \tag{4.28}$$

with

$$\vec{\Omega}_{\mathrm{cyc}} = -\frac{q}{\gamma m}\Big(\vec{B}_{\perp} - \frac{\vec{\beta} \times \vec{E}}{\beta^2 c}\Big). \tag{4.29}$$

A spin that is always aligned to the momentum vector is called *frozen* and can be used as the basis for an EDM experiment (see Section 4.4.2). The point where the cyclotron frequency and the spin precession frequency due to the MDM are equal can easily be calculated using:

$$\Delta\vec{\Omega}_{\mathrm{cyc},S} = \vec{\Omega}_{\mathrm{MDM}} - \vec{\Omega}_{\mathrm{cyc}} \tag{4.30}$$

$$= -\frac{q}{\gamma m}\left[G\gamma\vec{B}_{\perp} + (1+G)\vec{B}_{\parallel} - \Big(G\gamma - \frac{\gamma}{\gamma^2-1}\Big)\vec{\beta} \times \frac{\vec{E}}{c}\right]. \tag{4.31}$$

Assuming now an ideal accelerator consisting only of vertical magnetic bending fields and neglecting the EDM, the spin moves according to

$$\frac{\mathrm{d}\vec{S}}{\mathrm{d}t} = -\frac{q}{\gamma m}(1+G\gamma)\vec{B}_y \times \vec{S}. \tag{4.32}$$

Contrary to all other spin orientations, an initial spin parallel or anti-parallel to the vertical axis will not precess in this case and stays stable over time. The axis along which the spin orientation is preserved is called the invariant spin axis or spin closed orbit $\vec{n}_c$. In analogy to the betatron oscillations the spin tune ν_S is defined as the number of spin oscillations per revolution. For the considered case of a basic pure magnetic ring the spin tune is given by

$$\nu_S = \frac{-\frac{q}{\gamma m}(1+G\gamma)}{-\frac{q}{\gamma m}} - 1 = \gamma G. \tag{4.33}$$

Here, the rotation of the co-moving coordinate system was taken into account by the subtraction of one revolution.

4.3 Spin Transfer Matrix

In order to perform spin tracking simulations it can be useful to describe the spin motion in terms of the phase space coordinates of a particle. Therefore, the equation of motion (4.23) can be expressed with respect to the ring angle θ:

$$\frac{\mathrm{d}\vec{S}}{\mathrm{d}\theta} = \rho\frac{\mathrm{d}\vec{S}}{\mathrm{d}s} = \rho\frac{\mathrm{d}t}{ds}\frac{\mathrm{d}\vec{S}}{dt} = \rho t'\frac{\mathrm{d}\vec{S}}{dt} = \rho t'\Big[\vec{\Omega}_{\mathrm{MDM}} + \vec{\Omega}_{\mathrm{EDM}}\Big] \times \vec{S}. \tag{4.34}$$

Considering again only the MDM part of the equation and assuming a vanishing EDM, Equation (4.34) reduces to:

$$\frac{\mathrm{d}\vec{S}}{\mathrm{d}\theta} = \rho t' \vec{\Omega}_{\mathrm{MDM}} \times \vec{S} = \vec{S} \times \vec{F}, \tag{4.35}$$

where $\vec{F}$ includes all perturbing fields. The evolution of the three spin components is then described in a rotating frame by

$$\frac{\mathrm{d}}{\mathrm{d}\theta}(S_1, S_2, S_3) = \vec{S} \times \vec{F} + (S_2, -S_1, 0). \tag{4.36}$$

For small transverse and longitudinal perturbation fields, the vector components can be written as

$$F_1 = \rho(1+G\gamma)\frac{q}{p}B_1 = \rho y''(1+G\gamma), \tag{4.37}$$

$$F_2 = \rho(1+G)(B_2 - y'B_3)\frac{q}{p} = -(1+G)y' + \rho(1+G)\left(\frac{y}{\rho}\right)', \tag{4.38}$$

$$F_3 = \rho(1+G\gamma)\frac{q}{p}B_3 = -(1+G\gamma) + (1+G\gamma)\rho x''. \tag{4.39}$$

In case of having only magnetic guiding fields and a particle moving on the reference orbit, $\vec{F}$ reduces to

$$\vec{F} = -(1+G\gamma)\vec{e}_3 \tag{4.40}$$

and the system of linear equations with initial spin components $\vec{S}_i$ given in Equation (4.36) is solved by the vector

$$\begin{pmatrix} S_1 \\ S_2 \\ S_3 \end{pmatrix} = \begin{pmatrix} \cos(G\gamma\theta) & -\sin(G\gamma\theta) & 0 \\ \sin(G\gamma\theta) & \cos(G\gamma\theta) & 0 \\ 0 & 0 & 1 \end{pmatrix} \begin{pmatrix} S_{1,i} \\ S_{2,i} \\ S_{3,i} \end{pmatrix}. \tag{4.41}$$

In the discussed ideal case, the eigenvalues of the spin transfer matrix read

$$\lambda_{1,2} = e^{\pm iG\gamma\theta},\ \lambda_3 = 1. \tag{4.42}$$

As already mentioned previously, this illustrates again that the spin component along the $\vec{e}_3$ axis is stable whereas the other components precess.
Assuming that there are no other vertical magnetic fields, one can exchange the F_3 component simply by γG. Equation (4.35) can then be written as

$$\frac{\mathrm{d}\vec{S}}{\mathrm{d}\theta} = \vec{n} \times \vec{S} \quad \text{with} \quad \vec{n} = \gamma G\vec{e}_3 - F_1\vec{e}_1 - F_2\vec{e}_2. \tag{4.43}$$

The two-component spinor formalism from Section 4.1 can be used to rewrite Equation (4.43) in the following way:

$$\frac{\mathrm{d}\chi}{\mathrm{d}\theta} = -\frac{i}{2}H\chi = -\frac{i}{2}(\vec{\sigma}\vec{n})\chi = -\frac{i}{2}\begin{pmatrix}\gamma G & \xi \\ -\xi^* & \gamma G\end{pmatrix}\chi, \tag{4.44}$$

where H denotes the spin precessing kernel and the perturbating fields are incorporated in the complex expression

$$\xi(\theta) = F_1 - iF_2. \tag{4.45}$$

It can directly be seen that in the presence of additional perturbating fields ($\xi \neq 0$) the spinor components are no longer conserved. The solution of the spinor equation is given by

$$\chi(\theta_f) = \mathcal{T}exp\left(\int_{\theta_i}^{\theta_f} -\frac{i}{2}H(\theta)\mathrm{d}\theta\right)\cdot\chi(\theta_i) = t(\theta_f,\theta_i)\cdot\chi(\theta_i), \tag{4.46}$$

where $\mathcal{T}$ denotes the quantum mechanical time evolution operator and the subscript i and f indicate the initial and final state respectively. The spin transfer matrix for each element in the accelerator can be calculated using the T-BMT equation. Hence, the product of all single matrices $t(\theta_f,\theta_i)$ between the starting and end point has to be multiplied by the initial spinor state to obtain the final spinor wave function. The spin transfer matrix for a full revolution is called the one turn map and is defined as:

$$t(\theta_i + 2\pi, \theta_i) = e^{-\frac{i}{2}\nu_S\vec{n}_C\cdot 2\pi}. \tag{4.47}$$

In this general form, the spin tune ν_S and the spin closed orbit $\vec{n}_C$ are also defined in a general case where perturbating fields could be involved. The phase space coordinates of an arbitrary particle that performs betatron and synchrotron oscillations vary each turn. Therefore, the spin is influenced by different fields at different positions each revolution. As a consequence, the spin precession frequency and its phase advance also vary from turn to turn. Accounting for this effect, the definition of the invariant spin axis is extended to the invariant spin field $\vec{n}(\vec{z})$ and the following expression holds:

$$\vec{n}(\vec{z}_f) = A(\vec{z}_i)\vec{n}(\vec{z}_i). \tag{4.48}$$

Here, $\vec{z}$ denotes the phase space motion and A describes the spin transfer map that is now dependent on the phase space.

4.4 EDM Experiments in Storage Rings

At present, any EDM experiment uses the interaction of the EDM with electric fields. Non-zero EDMs lead to a distortion of the regular spin precession. Storage

rings can be used to investigate charged particles since they work as a trap and the particles will not get lost in the presence of electric fields.

4.4.1 Basic Concept

The main principle of an EDM measurement using a storage ring is based on an initial polarization in the horizontal plane. Magnetic or electric fields are then used to trap the particle beam inside the accelerator. These fields can be Lorentz transformed to the rest frame of the particle resulting in electric $\vec{E}^*$ and magnetic $\vec{B}^*$ fields in the rest frame. The electric fields in the rest frame interact with the EDM according to [50]:

$$\frac{d\vec{S}}{dt} = \vec{d} \times \vec{E}^*. \tag{4.49}$$

Assuming that the magnetic and electric fields are perpendicular to the momentum and taking the MDM into account, the spin motion can be expressed by simplifying Equation (4.25) to [49, 51]:

$$\frac{d\vec{S}}{dt} = \vec{S} \times \vec{\Omega} = \vec{S} \times (\vec{\Omega}_{\mathrm{MDM}} + \vec{\Omega}_{\mathrm{EDM}}) \tag{4.50}$$

where

$$\vec{\Omega}_{\mathrm{MDM}} = -\frac{q}{m}\left[G\vec{B} - \left(G - \frac{1}{\gamma^2 - 1}\right)\frac{\vec{\beta} \times \vec{E}}{c}\right], \tag{4.51}$$

$$\vec{\Omega}_{\mathrm{EDM}} = -\frac{q}{mc}\frac{\eta_{\mathrm{EDM}}}{2}\left[\vec{E} + c\vec{\beta} \times \vec{B}\right]. \tag{4.52}$$

For a vanishing EDM the spin precession in an ideal storage ring thus takes place in the horizontal plane and the spin closed orbit $\vec{n}_C$ is aligned to the vertical direction. Since $\vec{\Omega}_{\mathrm{EDM}} \perp \vec{\Omega}_{\mathrm{MDM}}$, a non-zero EDM ($\vec{\Omega}_{\mathrm{EDM}} \neq 0$) tilts the spin closed orbit in the radial direction as shown in Figure 4.1 . The result is a vertical oscillation of the polarization with frequency $\vec{\Omega}_{\mathrm{EDM}}$. For a pure magnetic machine, the tilt angle ξ_{EDM} can be described by the ratio of the EDM and MDM contributions (see Equations (4.23) and (4.31)):

$$\tan(\xi_{\mathrm{EDM}}) = \frac{\eta_{\mathrm{EDM}}\beta}{2G}. \tag{4.53}$$

An EDM measurement is possible if the experimental setup results in a macroscopic buildup of the vertical polarization. The method described above was used for the EDM measurement of muons [31]. The anomalous magnetic moment G of protons and deuterons are two and three orders of magnitude larger. Therefore, the resulting tilt angle ξ_{EDM} would be significantly smaller in case of similar beam energy and EDM value. To overcome this challenge and to realize EDM

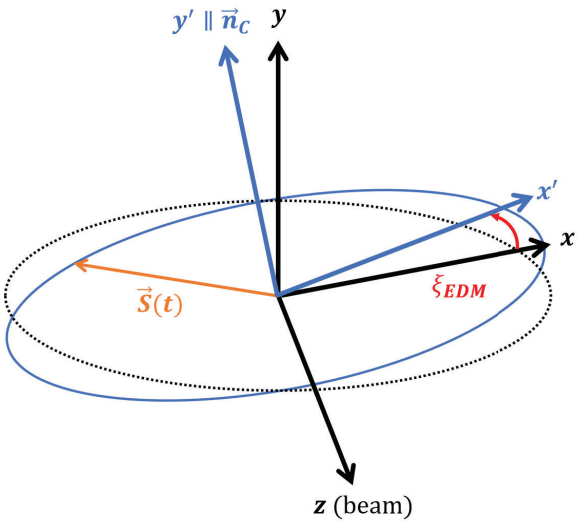

Figure 4.1: Sketch of the tilt ξ_{EDM} of the spin closed orbit due to the interaction of the EDM with the magnetic bending fields in a storage ring. The MDM and EDM contributions are perpendicular to each other. As a result, the vertical spin component oscillates.

experiments for protons and deuterons, different methods were proposed and will be discussed in the following sections [34, 52].

4.4.2 Frozen Spin Method

The sensitivity of the EDM measurement is directly coupled to the tilt angle ξ_{EDM}. This angle can be increased by minimizing the spin precession due to the MDM. To ensure a spin parallel to the momentum vector, the spin precession frequency has to be the same as the momentum precession. Using Equation (4.31) the so called *Frozen Spin* condition is achieved:

$$G\vec{B} = \left(G - \frac{1}{\gamma^2 - 1}\vec{\beta} \times \frac{\vec{E}}{c}\right). \tag{4.54}$$

Depending on the particle and its anomalous magnetic moment G different combinations of electric and magnetic fields have to be used in order to fulfill this condition.

- **Pure electric ring:** For particles with $G > 0$ the spin can be frozen using only electric fields. Therefore, the particles must have a specific momentum, often called *magic* momentum:

$$p_{\mathrm{magic}} = \gamma\beta mc = \sqrt{\gamma^2 - 1}\; mc = \frac{mc}{\sqrt{G}}. \tag{4.55}$$

The magic momentum of the proton possessing an anomalous magnetic moment of $G = 1.79$ is $p \approx 0.701\mathrm{Gev/c}$.

- **Combined magnetic and electric ring:** Particles with a negative anomalous magnetic moment ($G < 0$) can only be frozen when a combination of electric and magnetic fields is used. The ratio between the field strength of the vertical magnetic and radial electric field can easily be deduced from Equation (4.54) and yields:

$$\frac{|\vec{B}|}{|\vec{E}|} = \Big(1 - \frac{1}{G(\gamma^2 - 1)}\Big)\frac{\beta}{c}. \tag{4.56}$$

Lattice design studies for both types of storage rings are currently carried out within the JEDI collaboration [53, 54]. If the frozen spin condition is fulfilled, the MDM does not at all contribute to the spin motion. The interaction of the EDM and the present electromagnetic fields lead to a slow buildup of the vertical polarization and the EDM can directly be determined by measuring the spin rotation frequency Ω_{EDM}. In case of a pure electric ring using electric fields of $10\,\mathrm{MVm}^{-1}$ and assuming an EDM of $|\vec{d}| \approx 10^{-24}\ e\,\mathrm{cm}$, the spin precession frequency would be of the order of 0.1 mHz. Since the polarization lifetime at a usual storage ring is up to 1000 s only the beginning of this small frequency is observed by the polarimeter, leading to a linear increase in the vertical polarization P_y which is directly proportional to the EDM:

$$P_y(t) = P_0 \cdot \sin(\Omega_{\mathrm{EDM}} t) \approx P_0 \cdot \Omega_{\mathrm{EDM}} t. \tag{4.57}$$

In addition to the EDM signal, systematic contributions could also lead to a vertical polarization buildup. Besides other magnet misalignments and field imperfections, especially radial magnetic fields from misaligned quadrupoles could have a significant impact on the measured signal [21, 55]. The contribution of these imperfections could be resolved by using clockwise and counter-clockwise rotating beams within in same storage ring [56, 57].

As already mentioned, proposals for frozen spin storage rings have been made but not such storage ring has reached the operation stage yet. Common storage rings only use magnetic fields and cannot fulfill the frozen spin condition. Therefore, a different method of measuring the EDM in a storage ring like the Cooler Synchrotron (COSY) is proposed and will be discussed in the following section.

4.4.3 RF Wien Filter Method

As described in Section 4.4.1, a non-vanishing EDM leads to an oscillation of the vertical polarization. In principle, this oscillation is measurable but gets very small for protons and deuterons. In addition, the spin precession due to the

MDM in a magnetic storage ring is always present and the resulting spin tune yields $\nu_S = G\gamma$. Therefore, the signal averages out over time since the vertical polarization oscillates at a frequency of $f_S = \nu_s f_{rev}$. The idea of using an RF Wien filter is to introduce an artificial spin resonance that prevents the signal from vanishing completely [33, 58]. The device is installed such that the electric field points in radial direction and the perpendicular magnetic field is aligned to the vertical axis. The fields are set up in a way that the Lorentz force inside the device vanishes relative to the reference momentum. Therefore, no force acts on the reference particle and its trajectory through the machine stays unperturbed. In order to increase the EDM signal, the electromagnetic fields of the RF Wien filter oscillate at a harmonic of the spin precession frequency:

$$f_{WF} = (1 + k)f_S = (1 + k)\gamma G f_{rev} \quad \text{with} \quad k \in \mathbb{Z}. \tag{4.58}$$

Running the Wien filter with the above settings does not change the oscillation frequency f_S of the vertical polarization. In addition, the induced spin resonance by the Wien filter results in a small vertical polarization buildup over time that is directly proportional to the EDM. The main principle of an RF Wien filter in an EDM experiment is also shown in Figure 4.2. In a purely magnetic storage ring without a Wien filter and an initial polarization in the horizontal plane, the longitudinal component of the spin points as often in the direction of the momentum as it does in the opposite direction. Therefore, the vertical polarization due to an EDM oscillates around zero and the average over time vanishes. The Wien filter introduces an additional rotation of the spin around the vertical axis such that the longitudinal component of the spin is no longer as often parallel as it is anti-parallel to the momentum direction. Thus, a fraction of the vertical polarization survives and a polarization buildup can be observed over time. Such an RF Wien filter was already installed in COSY in order to perform the first direct deuteron EDM measurement within the precursor experiment [59].
Besides the EDM itself, systematic effects such as magnet misalignments lead to a vertical spin buildup. The measured signal is therefore a sum of all these systematic effects and the real EDM contribution. In order to study several systematic effects, a realistic model of the machine and precise spin tracking simulations are required. Especially the simulation of the spin closed orbit under the influence of all known systematic effects is of great interest. Its radial component cannot be determined within the experiment and is needed for the data analysis [60]. Therefore, a reliable model is the necessary basis for all further simulations. The implementation and optimization of such a model as well as the investigation of the spin closed orbit under several systematic effects are the topic of this thesis.

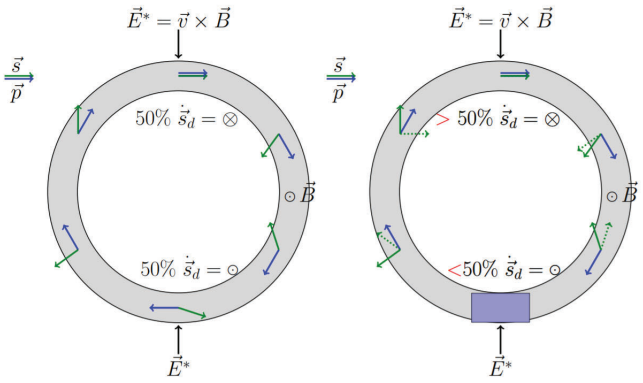

Figure 4.2: Schematic drawing of the RF Wien filter method. The RF Wien filter is represented by the blue box in the right sketch. Without an RF Wien filter (left), the spin points as often in direction of motion as it points in opposite direction. Therefore, the EDM signal fully averages to zero over time. The Wien filter (right) leads to an additional rotation of the spin around the vertical axis. As a result, the vertical polarization still oscillates but the signal does not completely vanish and a vertical polarization builds up over time [50].

5. Simulation Model

In order to systematically investigate the particle and spin motion for the precursor experiment at COSY, it is essential to develop a simulation model that describes the real machine and experiment setup as precise as possible. In this chapter, the model that was used within this thesis is described and benchmarked. Furthermore, different systematic effects that influence the measurement, are implemented into the model and their impact on the behavior of the particles is discussed.

5.1 The Cooler Synchrotron COSY

The accelerator facility COSY (COoler SYnchrotron) is located at *Forschungszentrum Jülich* in Germany and consists of three main parts: an ion source, the cyclotron JULIC and finally the Cooler Synchrotron COSY [61]. Figure 5.1 shows a schematic overview over the setup of COSY and the cyclotron.

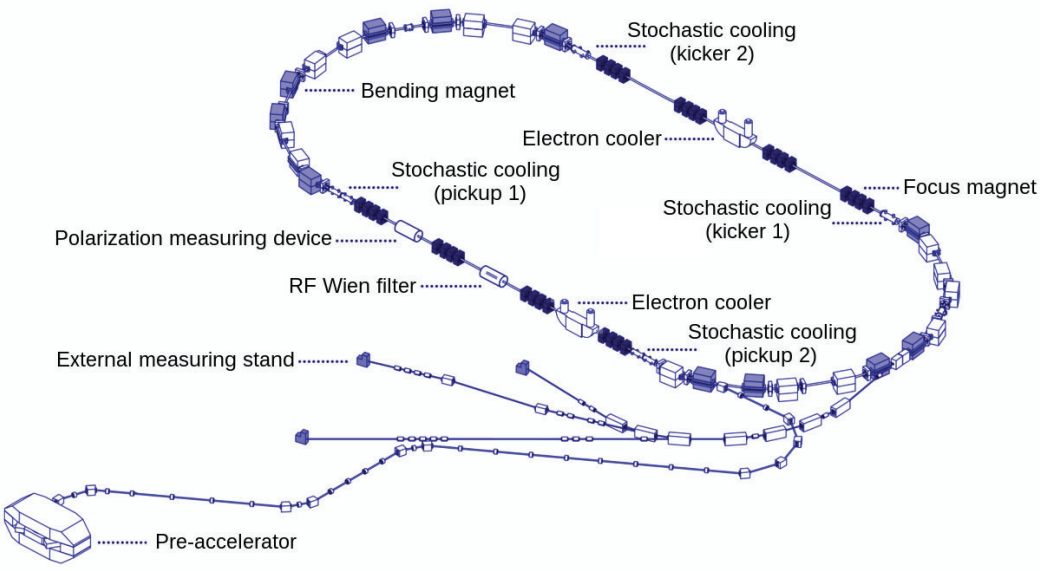

Figure 5.1: Sketch of the synchrotron COSY and the pre-accelerator JULIC including the main magnets, cooling sections, the RF Wien filter device and the polarimeter. Adapted from [62].

The ion source can provide negatively charged hydrogen H^- or deuterium ions D^-, either polarized or unpolarized [63]. The H^- and D^- ions can be pre-accelerated in the cyclotron JULIC up to kinetic energies of 45 MeV and 75 MeV respectively [64]. Finally, the beam is injected into COSY via stacked stripping injection, where two electrons are removed from the ions using a carbon foil. Therefore, the final beam consists of protons or deuterons.

In COSY, the beam can be accelerated up to momenta of 3.7 GeV/c and the acceleration takes place in an RF cavity located in the middle of one of the straight sections. The ring has a total circumference of roughly 183.4 m and consists of two arcs and two straight sections, each with a length of 40 m [61]. The bending of the beam is achieved by using 24 normal-conducting dipoles with magnetic fields of up to 1.67 T. In order to focus the beam, 56 magnetic quadrupoles are installed and grouped into families of four. Within one family, the magnets have the same dimensions and are connected to the same power supply. In order to use each straight section as a telescope with 1:1 imaging and to enable a betatron phase advance of π or 2π per straight section, eight of the quadrupole families are located in the straight sections, four triplets in each one [65]. In addition to dipoles and quadrupoles, 17 sextupoles, seven in the straight sections and 10 positioned in the arcs, can be used for changing the chromaticity. Here, the sextupoles in the arcs are divided into three families. Orbit measurements and corrections can be done by using 30 (29) beam position monitors (BPMs) and 22 (19) corrector magnets in the horizontal (vertical) direction along the ring.

COSY partly owes its name to the phase space controlling which is achieved by beam cooling. On the one hand, the beam can be cooled by electron cooling, which is used up to momenta of 0.6 GeV/c. Additionally a second electron cooler was installed at COSY in 2013 which enables cooling in the whole energy range of COSY [66, 67]. On the other hand stochastic cooling is provided for particle momenta above 1.5 GeV/c [68, 69]. The combination of cooling and beam motion manipulation results in a perfect setup to investigate methods and tools for a dedicated EDM storage ring.

Several devices for spin manipulation, like an RF Solenoid, an RF Wien filter and a Siberian Snake, are installed into the ring. They can among others be used to cross depolarizing resonances or to transfer the polarization from the vertical into the horizontal plane [70, 71, 72].

In the straight sections of COSY, experiments can be installed. The Wide Angle Shower Apparatus (WASA) detector is installed in one of them [73]. A target can be moved into the beam pipe such that elastic scattering reactions are produced. Starting a measurement, the beam is broadened by an external excitation. A feedback loop between the detector rate and the excitation ensures a slow and

constant depletion of the beam. A second polarimeter, that was installed recently, is the so called JEDI Polarimeter (JEPO) [74, 75]. It is composed of inorganic scintillators and supposed to measure vertical polarization changes with an increased precision compared to previous methods.

Besides internal experiments, COSY also provides the option to extract the beam using a magnetic septum and guiding it via the extraction beamline to one out of three possible external experiment places.

5.2 The Lattice

The simulations within this thesis are done using the software library *Bmad* that has been developed at Cornell University's Laboratory for Elementary Particle Physics [76]. The library provides subroutines in order to simulate the beam and spin dynamics of relativistic charged particles within linear or closed accelerator structures. It offers the possibility to do single particle as well as multi-particle tracking using different tracking algorithms. For the following simulations, the tracking was done using a 4th order Runge-Kutta integration algorithm with adaptive step size control. Regarding spin tracking, Bmad allows to take a non-vanishing EDM into account.

The COSY model includes all relevant magnets: dipoles, quadrupoles and sextupoles. The effective lengths l_{eff} of the magnets are summarized in Table 5.1. An RF cavity ensures phase focusing and a model of the RF Wien filter is designed (see Section 5.4). Furthermore, the corrector magnets, used for orbit bumps and the orbit correction, are implemented. To compare measured and simulated orbits, all beam position monitors are included. The default lattice consists of ideal magnets without fringe fields and vanishing misalignments. Those effects can separately be turned on in order to study their effects on the orbit and the spin

Magnet type	l_{eff} in m
Dipole	1.832596
Quadrupole (arc)	0.372
Quadrupole(straight)	0.620
Sextupole ("G")	0.328
Sextupole ("L")	0.243
Sextupole ("S")	0.140

Table 5.1: Effective lengths of magnets in the COSY model. There are two types of quadrupoles: the ones in the arcs are shorter than the ones used in the straight sections. Three types of sextupoles are used, each with a different length.

motion. Initially, the sextupoles and corrector magnets are turned off. The dipole fields are always set such that the reference particle is perfectly guided around the ring. The default quadrupole strengths are given in Appendix A.2. The actual magnet settings of a specific beam time are stored via the Experimental Physics and Industrial Control System (EPICS) [77] and a routine was implemented to directly download and transform them into Bmad syntax.

The optical functions of the described model are displayed in Figure 5.2. The horizontal axis of the plot indicates the position s along the ring and the starting point is chosen to be the injection point which is located close to the end of the first arc. The location of the arcs and straight sections in terms of the parameter s are displayed within Figure 5.2. Due to the location of the injection point within one arc, this arc is split into two sections in terms of s. The given magnet settings lead to the effect that in the straight sections, the dispersion is close to zero. Therefore, dispersive effects have their origin primarily in the arc sections. The betatron tunes for the default lattice turn out to be $Q_x = 3.62512$ in horizontal direction and $Q_y = 3.63061$ in vertical direction.

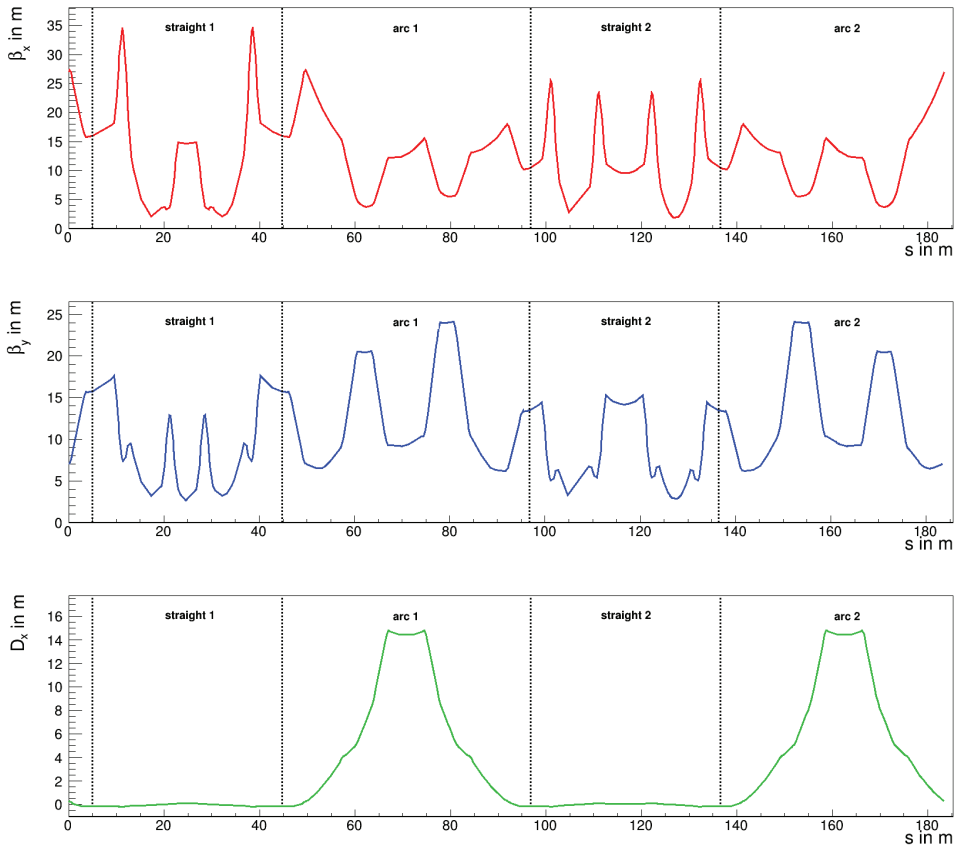

Figure 5.2: Optical functions β_x, β_y and D_x of the default lattice. The resulting dispersion in the straight sections is close to zero. Therefore, dispersive effects mainly appear in the arcs. The betatron tunes for the default lattice are $Q_x = 3.62512$ in horizontal direction and $Q_y = 3.63061$ in vertical direction.

5.3 Benchmarking of Particle and Spin Motion

Before adding additional effects, it is necessary to benchmark the default model. Therefore, the particle and spin motion is compared to theoretical predictions. Doing so, the numerical limit of the model can be quantified and it is guaranteed that the basis of all following simulations behaves correctly. The following simulations use deuterons with a momentum of 970 MeV/c and the closed orbit in both transverse directions is calculated. As expected, it is perfectly zero in vertical direction. Small deviations from zero of the horizontal closed orbit in the order of 10^{-11} can be observed. They are a consequence of small numerical deviations from the reference momentum. Nevertheless, these deviations are many orders of magnitude smaller than the effects that will be discussed later in this thesis. The closed orbit RMS[1] values are $\mathrm{RMS}_x = 7.625 \cdot 10^{-12}$ and $\mathrm{RMS}_y = 0.0$.

[1] Root Mean Square

In order to ensure the correct behaviour of the simulation model, the three-dimensional phase space was investigated for particles with different initial phase space coordinates. First, a particle having an initial horizontal offset with respect to the closed orbit, such that the horizontal emittance yields ϵ_x is 1 mm mrad, was analyzed and the corresponding phase space plots are shown in Appendix A.1. The horizontal offset leads to a well defined phase space ellipse in the horizontal phase space. Since the particle dynamics in COSY are almost completely decoupled, the vertical particle motion is not affected by the horizontal offset. Due to the horizontal offset, the particle moves no longer on the reference orbit but on a longer trajectory due to betatron oscillations and the non-zero dispersion in the arcs. This path lengthening leads to a mismatch of the arrival phase of the particle at the cavity and the design phase. Therefore, the center of the longitudinal ellipse is shifted to a new equilibrium momentum. Due to dispersion effects different ellipses varying in their horizontal center position can be seen in the longitudinal phase space. With an initial vertical offset, a well defined phase space ellipse can be seen in the vertical and the longitudinal phase space, as it is shown in Figure 5.3. The small distortions in the horizontal phase space result from non-vanishing dispersive areas in the arcs. The phase space of a particle with an initial longitudinal momentum offset of $\frac{\Delta p_z}{p_0} = 10^{-4}$ is displayed in Appendix A.2. Again, the vertical phase space is not affected by this distortion. However, the horizontal motion is now a superposition of betatron oscillations and dispersion trajectories.

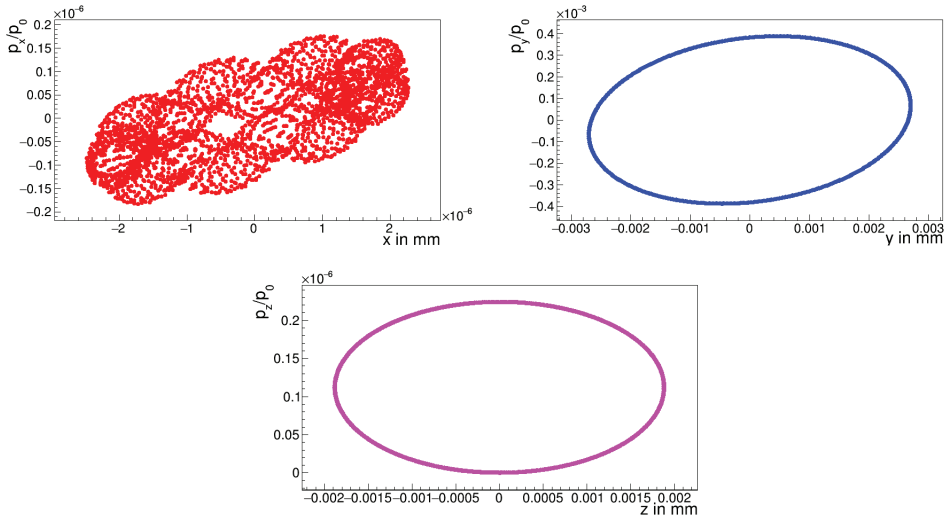

Figure 5.3: Three-dimensional phase space of a particle with an initial vertical offset at injection. The offset is chosen such that the vertical emittance ϵ_y turns out to be 1 mm mrad. A well defined phase space ellipse can be seen in the vertical and the longitudinal phase space. Small distortions in the horizontal phase space are the result of dispersive areas in the arcs.

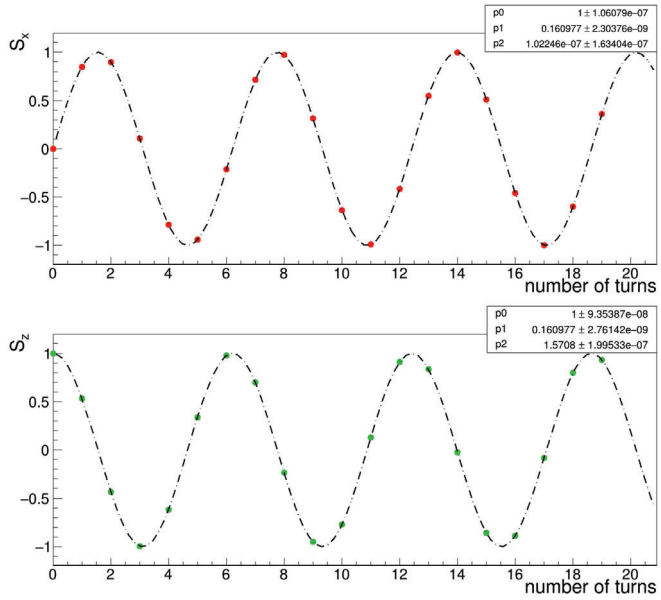

Figure 5.4: In-plane spin precession due to the MDM. The initial spin orientation is along the momentum vector and the spin precesses in the guiding fields of the dipoles. A sinusoidal fit was performed to determine the spin tune. The resulting value agrees with the theoretical prediction of $|\nu_S| = -0.160977$.

Besides the particle motion, the spin motion, too, has to be benchmarked against theoretical predictions. Starting with an initial spin pointing along the longitudinal axis ($S_z = 1$) and assuming a vanishing EDM, the spin is supposed to precess in the horizontal plane and the vertical spin component should be zero all the time. Using Equation (4.33), the spin tune is expected to be $|\nu_S| = 0.160977$. Figure 5.4 shows the tracking results of the in-plane spin components. One can see the oscillation in the horizontal plane. A sinusoidal fit was performed in order to determine the precession frequency. The resulting value is in agreement with the theoretical prediction. Due to numerical restrictions of the tracking simulation, the vertical spin component shows small fluctuations of the order of 10^{-13} as can be seen in Figure 5.5. Introducing now a non-vanishing EDM, a vertical oscillating spin buildup is expected. Figure 5.6 shows the vertical spin component in the case of an EDM of $10 \cdot 10^{-18}\,\mathrm{e\,cm}$ ($\eta_{\mathrm{EDM}} = 1.902052 \cdot 10^{-4}$). According to Equation (4.53), the invariant spin axis is now tilted and the vertical spin component starts oscillating. The amplitude of this oscillation can be approximated by

$$A \approx \left| \frac{\eta_{\mathrm{EDM}} \beta}{2G} \right| = 3.05532 \cdot 10^{-4}, \tag{5.1}$$

which is in good agreement with the fitted sine function in Figure 5.6. The bottom plot shows the behavior of the vertical spin component over a larger number of

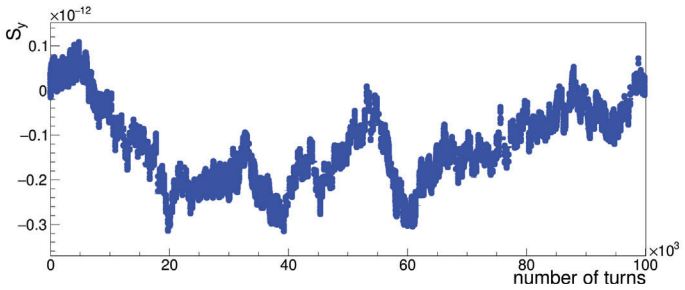

Figure 5.5: Vertical spin component of the reference particle with an initial spin pointing along the momentum vector and assuming a vanishing EDM. The vertical spin component is expected to stay zero. Due to the numerical limitations of the simulation, fluctuations of the order of 10^{-13} can be observed.

turns and the red line indicates the average vertical contribution. As expected, the EDM signal averages out over time without the implementation of an RF Wien filter.

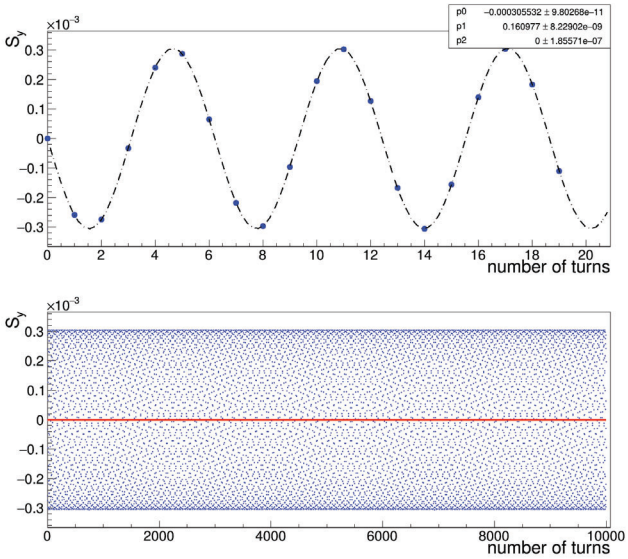

Figure 5.6: Tracking results for an initial spin along the momentum axes and an EDM of $10 \cdot 10^{-18}\,\mathrm{e\,cm}$ ($\eta_{\mathrm{EDM}} = 1.902052 \cdot 10^{-4}$). The invariant spin axis is tilted according to Equation (4.53) and the vertical spin component therefore performs fast oscillations. Over time, the EDM signal vanishes and the net spin buildup is zero.

5.4 Model of the RF Wien Filter

The essential device in the EDM precursor experiment at COSY is the RF Wien filter that was already briefly discussed in Section 4.4.3. In order to provide a complete simulation model of COSY, the RF Wien filter has to be described as realistically as possible within the Bmad model. Field calculations of the stripline design are considered [62] as the basis of the modeling. They are provided as a three-dimensional grid, covering the whole length of the device (1100 mm) and a range of ±5 mm in each transverse direction. Each direction is subdivided into 100 points, such that the distance between the points in the transverse directions equals 0.101 01 mm and a spacing of 11.111 mm is reached along the longitudinal axis. The maximum vertical magnetic and radial electric field values are displayed in Figure 5.7 for a vanishing vertical coordinate ($y = 0$). The advantage of sophisticated field calculations compared to a simple rectangular field approach are the included fringe fields of the magnetic and electric field that lead to a more realistic description of the device.

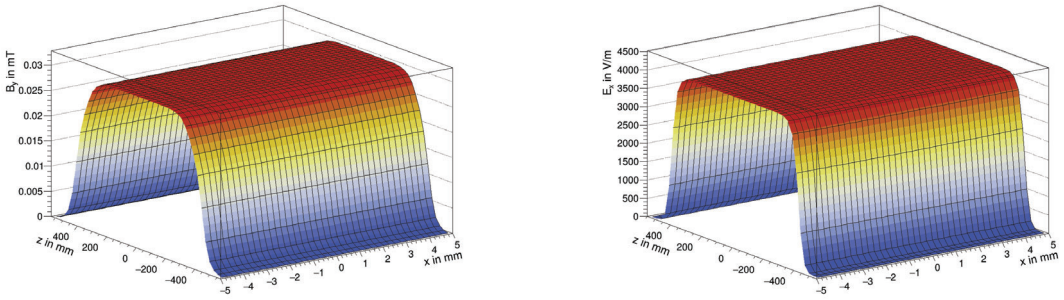

(a) Vertical magnetic field.

(b) Radial electric field.

Figure 5.7: Grid field calculations of vertical magnetic and radial electric field at maximum amplitude for a vanishing vertical field component ($y = 0$). The grid consists of one million grid points, i.e. 100 points in each direction. The transverse plane (x and y) covers a range of ±5 mm. The longitudinal range covers the complete length of the RF Wien filter device ($l_{WF} = 1100\,\text{mm}$).

Bmad offers the option to implement customized elements including field maps. The field value grid can be read in and a linear interpolation is done in order to evaluate the field in between the single grid points. The amplitude of the field can be adjusted using a field amplification factor f_{amp} within the model and the time dependent amplitude changes are synchronized with the revolution frequency f_{rev} of the simulated particle:

$$E_x = f_{\text{amp}} E_0 \cdot \cos(2\pi f_{\text{rev}} |k + \nu_S| + \phi), \tag{5.2}$$

where k denotes the harmonic number, which is typically chosen to be -1 ($f_{\mathrm{WF}} = 871\mathrm{kHz}$) for simulations within this thesis. The influence of the phase ϕ on the spin motion is further discussed in Section 5.4.2. The field is assumed to be zero outside the given grid dimensions. Therefore, tracking simulations only lead to reliable results if the transverse particle offsets at the position of the RF Wien filter are smaller than $\pm 5\,\mathrm{mm}$. A larger range could be covered using a larger grid map. Since the number of grid points critically influences the simulation time, a trade off between grid spacing and the performance of the simulations has to made based on the use case. Within this thesis, the given grid is large enough since the particle offsets do not exceed the given limits in simulations where a turned on Wien filter is used.

5.4.1 Lorentz Force Cancellation

The EDM experiment using an RF Wien filter only works properly, if the beam motion is not perturbed inside the device. Therefore, the electric and magnetic field have to be set up in a way that the Lorentz force vanishes. Assuming an ideal rectangular field distribution, the Lorentz condition can easily be calculated and reads:

$$\vec{E} = -\beta c \cdot \vec{B}. \tag{5.3}$$

In case of fringe fields, the local Lorentz force compensation is no longer guaranteed. Figure 5.8 displays the normalized electric and magnetic field along the longitudinal axis, assuming no transverse offset of the particle ($x = 0$ and $y = 0$). The fall off behavior of the fields in the fringe field areas is differently for electric and magnetic fields. Therefore, the Lorentz force is locally different from zero. In order to ensure a minimal beam perturbation inside the Wien filter, the magnetic field can be slightly adjusted in the simulation model. Following the procedure in [21], the main idea is to determine a scaling factor of the magnetic field such that the emittance is minimized when tracking the reference particle through the device. Therefore, a particle starting on the closed orbit is tracked over several turns. In case of a perfect local Lorentz force compensation or if the Wien filter was turned off, the particle would never leave the closed orbit. However, due to the different fringe field shape of the fields inside the Wien filter, the particle experiences a kick and starts to perform betatron oscillations. The particle motion is most sensitive, if the Wien filter fields oscillate with a frequency close to a betatron sideband frequency. The kicks inside the Wien filter add up and amplify the amplitude of the betatron motion. Therefore, the horizontal betatron tune is set to $Q_x = 4 + \nu_S \approx 3.839$ by varying the quadrupoles in the arcs. The vertical betatron tune has a value of $Q_y = 3.622$. As an example, Figure 5.9 depicts the horizontal particle offset as well as the horizontal emittance of the particle for a magnetic field scaling of $-1\,\%$. The horizontal offset and the emittance increase

up to a maximum value. Due to an amplitude dependent betatron tune a mismatch of the resulting excitation frequency and the betatron sideband frequency can occur. As a consequence, the particle slightly drifts away from the resonance with the Wien filter excitation and the amplitude of the betatron oscillations starts to decrease again.

The magnetic field of the RF Wien filter is subsequently changed while the electric field stays unchanged and a deuteron with a momentum of 970 MeV/c and initially positioned on the closed orbit is tracked for several turns. For each setting, the maximum value of the emittance is determined and summarized in Figure 5.10. In order to find the scaling factor of the magnetic field resulting in the minimum emittance value, a parabolic fit is performed to the data. In the case of simple rectangular fields without fringe field areas, the expected scaling factor would be exactly zero. For the more realistic case, the minimum is reached for an enhancement of the magnetic field by about 0.045 % and this scaling factor will be used in all following Wien filter related simulations.

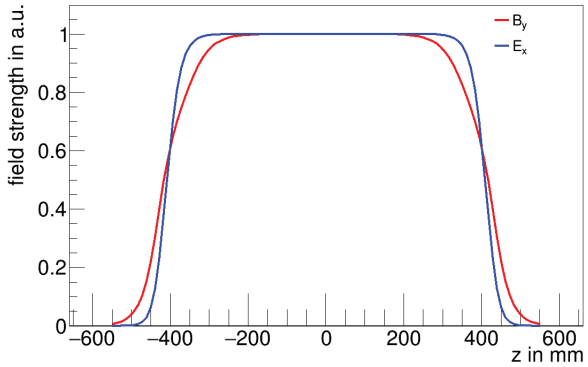

Figure 5.8: Normalized field distribution of the radial electric and vertical magnetic field along the longitudinal axis ($x = 0$ and $y = 0$) inside the RF Wien filter device. The fringe field behavior of both fields differ. Therefore, the Lorentz force is locally different from zero and the particle motion is perturbed.

5.4.2 Benchmarking

As a next step, the implemented RF Wien filter model has to be tested against theoretical predictions. The interaction of the spin with the additional electromagnetic fields can directly be seen when performing the same simulation as it was done for Figure 5.6. Again, the reference particle is tracked and an EDM of $10 \cdot 10^{-18}$ e cm is assumed. The tracking result is shown in Figure 5.11 and a linear fit was performed to indicate the average vertical spin component. Compared to Figure 5.6, the fast oscillations with an amplitude according to Equation

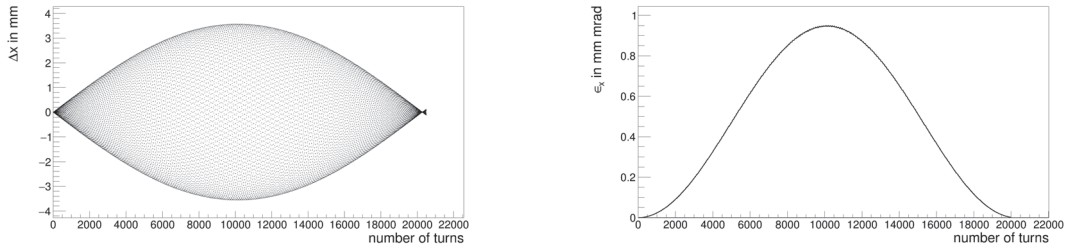

(a) Horizontal particle offset. (b) Horizontal emittance.

Figure 5.9: Tracking results of a deuteron with a momentum of 970 MeV/c and initial phase space coordinates on the closed orbit. The magnetic field of the Wien filter is reduced by 1 % compared to the default grid calculations. The horizontal betatron tune is changed to $Q_x = 4 + \nu_S \approx 3.839$ such that the Wien filter fields oscillate with a betatron sideband frequency. Therefore, the amplitude of the betatron oscillations adds up over time until the particle slips out of resonance.

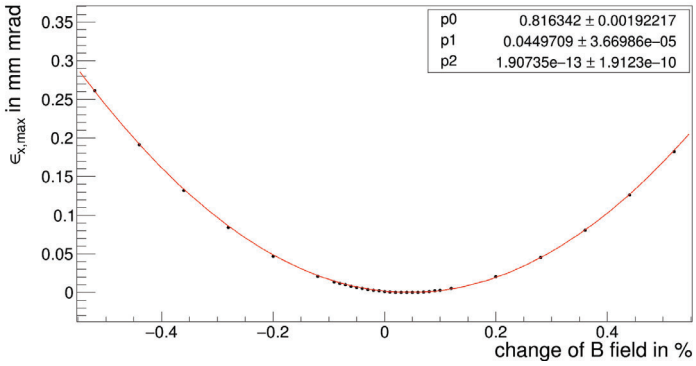

Figure 5.10: The maximum value of the horizontal emittance is shown as a function of the enhancement of the magnetic field inside the RF Wien filter. The electric field stays unchanged. A parabolic fit is performed in order to find the minimum emittance value and the corresponding scaling factor for the magnetic field. The minimum is reached for an increase of 0.045 %.

(4.53) are still present. In addition, a slow buildup of the average vertical spin component can be seen as it is expected due to the RF fields of the Wien filter. Assuming only small tilts of the invariant spin axis with respect to the vertical axis and having an initial spin in the plane perpendicular to $\vec{n}_c$, the slow vertical spin buildup can be estimated by [21]

$$S_y(\theta) \approx -\frac{\alpha_0}{4\pi} \frac{\eta_{\mathrm{EDM}} \beta}{2G} \cos(\phi)\ \theta, \tag{5.4}$$

where θ denotes the position along the beamline and ϕ is the initial phase of the Wien filter field oscillation. The parameter α_0 describes the maximum rotation

angle per turn, that depends on the maximum field strength inside the Wien filter. The initial phase ϕ directly influences the average vertical spin buildup per turn. This was investigated by several spin tracking simulations using the reference particle and an EDM of $10 \cdot 10^{-18}$ e cm. Figure 5.12 summarizes the results over the full range of ϕ. The single points show the simulation results and the dashed line represents the theoretical predictions. As expected from Equation (5.4), the average spin buildup takes its largest value for $\phi = 0°$ and there is no buildup at all for a phase of $\phi = 90°$.

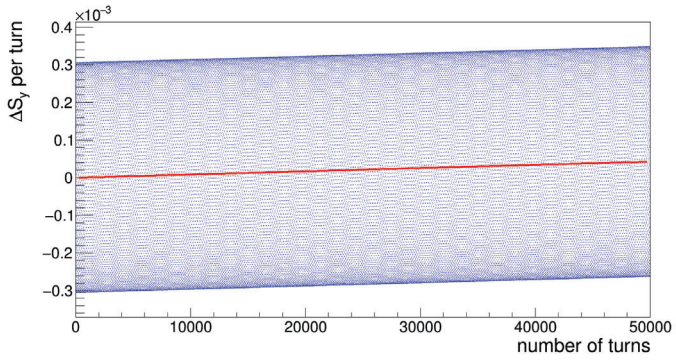

Figure 5.11: Tracking results for an initial spin along the momentum axes and an EDM of $10 \cdot 10^{-18}$ e cm ($\eta_{\mathrm{EDM}} = 1.902052 \cdot 10^{-4}$). The invariant spin axis is tilted according to Equation (4.53) and the vertical spin component therefore performs fast oscillations. Due to the electromagnetic fields of the RF Wien filter, a slow buildup of the average vertical spin component can be observed.

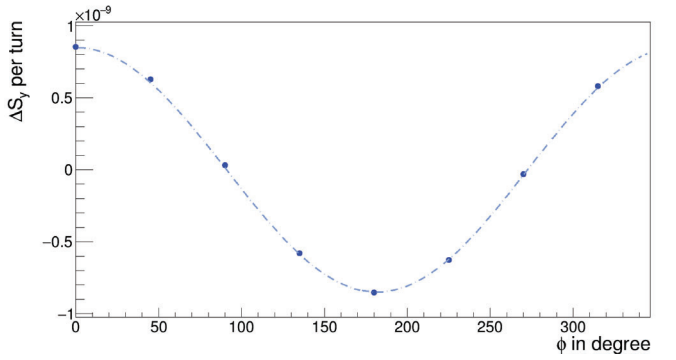

Figure 5.12: Average vertical spin buildup per turn as a function of the initial RF Wien filter phase ϕ. The dashed line represents the theoretical predictions based on Equation (5.4). For a phase of $\phi = 0°$ the vertical spin buildup per turn is maximum and there is no buildup at all for an initial phase of $\phi = 90°$.

The difference in fast oscillation amplitudes and the slope of the slow buildup of the vertical spin component for different EDM values can be seen in Figure 5.13.

For these tracking simulations, the field amplification factor for the Wien filter fields was set to 1000 to decrease the simulation time and to enhance the buildup. One can clearly see, that the amplitudes as well as the average buildup over time increase for larger EDMs which is in agreement with the theoretical prediction. A full slow oscillation was also simulated by using a field amplification factor of 10000 and an EDM value of $10 \cdot 10^{-15}$ e cm. The result is shown in Figure 5.14 where the blue points show the tracking results and the solid red line is a sinusoidal fit to the data. A full slow oscillation can not be detected during the precursor experiment due to its long oscillation period. The measurement takes place in the very beginning of the vertical spin buildup where the behavior of the spin buildup is linear in first order.

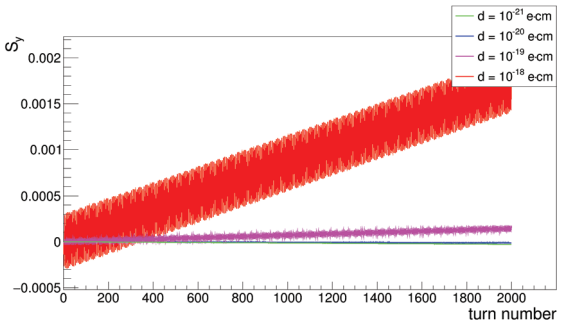

Figure 5.13: Vertical spin component for different EDM values. For the tracking calculation, a field amplification factor of 1000 was used to decrease the computing time and to enhance the spin behavior. The amplitude as well as the slope of the slow spin buildup clearly increase with larger EDM values which is in agreement with the theoretical prediction.

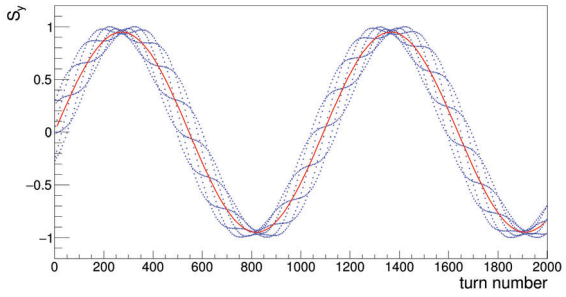

Figure 5.14: Tracking results using a field amplification factor of 10000 and an EDM value of $10 \cdot 10^{-15}$ e cm. The blue points correspond to the simulation results and the red line represents a sinusoidal fit to the data. A full slow oscillation is usually not detected within the experiment since the oscillation period is too long. The EDM measurement takes place in the very beginning of the vertical spin buildup where the behavior is almost linear.

5.5 Algorithm for Spin Tune and Invariant Spin Axis

The spin tune describes the spin precession per turn in the plane perpendicular to the invariant spin axis. Considering the default lattice, only the vertical magnetic guiding fields of the dipole contribute to the spin precession. Assuming a vanishing EDM, the spin precesses over one turn in the horizontal plane according to Equation (4.31) [78]:

$$\tilde{\vec{\Omega}} = -\frac{1}{c\beta}\frac{q}{m}G\int B\,\mathrm{d}l\cdot\vec{e}_y, \tag{5.5}$$

where the transformation $\mathrm{d}l = c\beta\mathrm{d}t$ was applied and it was assumed that $\vec{S} = S\vec{e}_s$ holds. The spin motion is then described by:

$$\frac{\mathrm{d}\vec{S}}{S} = \frac{1}{c\beta}\vec{\Omega}\times\vec{e}_s\mathrm{d}l = \tilde{\vec{\Omega}}\times\vec{e}_s \tag{5.6}$$

From the equilibrium of the Lorentz force and centripetal force one can easily get the expression:

$$\int B\,\mathrm{d}l = B\rho\cdot 2\pi = \frac{2\pi m\gamma c\beta}{q}, \tag{5.7}$$

such that the spin precession finally can be written as:

$$\tilde{\vec{\Omega}} = -\frac{1}{c\beta}\frac{q}{m}G\int\frac{2\pi m\gamma c\beta}{q}\cdot\vec{e}_y = -2\pi\gamma G\cdot\vec{e}_y. \tag{5.8}$$

As expected, the spin tune in this case is given by $\nu_S = |\tilde{\vec{\Omega}}|/(2\pi) = \gamma G$ and the invariant spin axis points along the vertical axis $\vec{e}_y$. If the EDM now takes a non-vanishing value and assuming that $\vec{\beta}\parallel\vec{e}_s$, the invariant spin axis tilts according to Equation (4.53). Equation (5.8) is extended to:

$$\tilde{\vec{\Omega}} = -2\pi\gamma G\cdot\vec{e}_y - \frac{1}{c\beta}\frac{q}{m}\eta_{\mathrm{EDM}}\frac{\beta}{2}\int B\mathrm{d}l\cdot(\vec{e}_z\times\vec{e}_y) \tag{5.9}$$

$$= -2\pi\gamma G\cdot\vec{e}_y + \pi\gamma\eta_{\mathrm{EDM}}\beta\cdot\vec{e}_x \tag{5.10}$$

and the spin tune now reads:

$$\nu_S = \gamma G\sqrt{1+\left(\frac{\eta_{\mathrm{EDM}}\beta}{2G}\right)^2}. \tag{5.11}$$

To determine the spin tune and the invariant spin axis for a given simulation setting, short spin tracking calculations are used. The reference particle is tracked for n turns and the spin orientation is recorded at the longitudinal position of interest after each turn. Since the particle moves exactly on the closed orbit, a well defined spin wheel is the result of the tracking simulation as can be seen in Figure 5.15 [79].

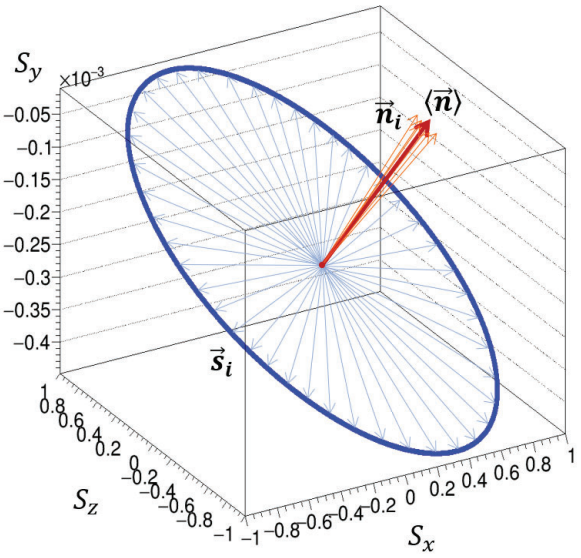

Figure 5.15: Spin tracking simulations using the reference particle moving on the closed orbit result in a well defined spin wheel. The invariant spin axis is the vector perpendicular to the plane that is defined by the spin wheel. The tilt of the invariant spin axis depends on the EDM value and other systematic effects such as magnet misalignments. For each turn, the normal vector $\vec{n}_i$ is calculated. The average normal vector $\langle\vec{n}\rangle$ is then considered as the invariant spin axis.

For the spin tune calculation, the following vectors are defined:

$$\vec{v}_1 = \begin{pmatrix} s_{x,i} \\ s_{y,i} \\ s_{z,i} \end{pmatrix}, \tag{5.12}$$

$$\vec{v}_2 = \begin{pmatrix} s_{x,i+1} \\ s_{y,i+1} \\ s_{z,i+1} \end{pmatrix} \quad \text{with } i \in \{1, ..., n-1\}, \tag{5.13}$$

	spin tune	
d [e cm]	theory	simulation
0.0	−0.160977180445162	−0.160977180441461
10^{-18}	−0.160977187958749	−0.160977187955047
10^{-19}	−0.160977180520298	−0.160977180516598
10^{-20}	−0.160977180445913	−0.160977180442212

Table 5.2: Comparison of spin tune values of the simulation code with theoretical predictions.

where i denotes the turn number. The spin tune is then calculated as the average spin tune of all consecutive single spin tunes:

$$\nu_{S,i} = \frac{1}{2\pi} \cos^{-1}\left(\frac{\vec{v}_1 \cdot \vec{v}_2}{|\vec{v}_1||\vec{v}_2|}\right), \tag{5.14}$$

$$\nu_S = \overline{\nu_S} = \frac{1}{n-1} \sum_{i=1}^{n-1} \nu_{S,i}. \tag{5.15}$$

In order to test the algorithm, the default lattice is used for tracking deuterons at 970 MeV/c and a vanishing EDM is assumed. The spin tune according to theoretical predictions is then given by $\nu_S = -0.160977180445162$. Tracking the spin over 30 turns ($n = 30$) and calculating the spin tune according to Equation (5.15) yields:

$$\nu_S = -0.16097718044146114 \pm 3.5 \cdot 10^{-16}. \tag{5.16}$$

The error on the spin tune value is the standard deviation of the ensemble of single spin tunes. The simulation agrees with the theoretical prediction to the 11th digit. This precision is sufficient since the spin tune at COSY can only be measured with an accuracy of 10^{-9} [[80], [81]]. Further tests can now be done assuming non-vanishing EDMs. Table 5.2 shows simulation results for three different EDM values and compares them to the theoretical predictions. One can be seen that the accuracy stays within eleven digits. Figure 5.16 shows simulation results in red and the corresponding theoretical predictions in blue for EDM values between $10 \cdot 10^{-20}$ e cm and $10 \cdot 10^{-18}$ e cm.

For the determination of the invariant spin axis, the same tracking results as for the spin tune can be used. In addition to the vectors $\vec{v}_1$ and $\vec{v}_2$, the initial spin vector is denoted by $\vec{v}_0$. For each turn i, the two vectors $\vec{d}_1$ and $\vec{d}_2$ are defined as the difference between the spin vector after the $i-$th turn and the initial one:

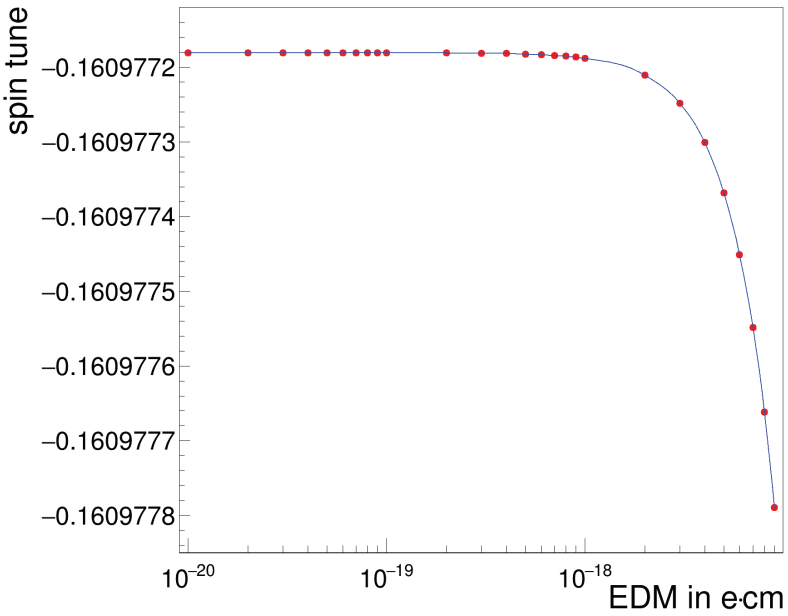

Figure 5.16: Spin tune determination using spin tracking calculations. The red dots represent the simulation results, the blue line indicates the theoretical predictions according to Equation (5.10).

$$\vec{d}_1 = \frac{\vec{v}_1 - \vec{v}_0}{|\vec{v}_1 - \vec{v}_0|} = \frac{1}{|\vec{v}_1 - \vec{v}_0|} \begin{pmatrix} s_{x,i} - s_{x,0} \\ s_{y,i} - s_{y,0} \\ s_{z,i} - s_{z,0} \end{pmatrix}, \tag{5.17}$$

$$\vec{d}_2 = \frac{\vec{v}_2 - \vec{v}_0}{|\vec{v}_2 - \vec{v}_0|} = \frac{1}{|\vec{v}_2 - \vec{v}_0|} \begin{pmatrix} s_{x,i+1} - s_{x,0} \\ s_{y,i+1} - s_{y,0} \\ s_{z,i+1} - s_{z,0} \end{pmatrix} \quad \text{with } i \in \{1, ..., n-1\}. \tag{5.18}$$

The invariant spin axis is then calculated as the average normal vector to the plane that is spanned by the vectors $\vec{d}_{1,i}$ and $\vec{d}_{2,i}$:

$$\vec{n}_i = \frac{\vec{d}_{1,i} \times \vec{d}_{2,i}}{|\vec{d}_{1,i} \times \vec{d}_{2,i}|} \tag{5.19}$$

$$\langle \vec{n} \rangle = \frac{1}{n-1} \sum_{i=1}^{n-1} \vec{n}_i. \tag{5.20}$$

The procedure is sketched in Figure 5.15. To benchmark the algorithm, the default lattice is again taken and the reference particle is tracked over 30 turns

assuming a vanishing EDM. The invariant spin axis is supposed to be perfectly aligned with the vertical axis. The algorithm results in an invariant spin axis of:

$$\vec{n}_{c,sim} = \begin{pmatrix} -1.7 \cdot 10^{-14} \\ 1.0 \\ 1.5 \cdot 10^{-14} \end{pmatrix} \pm \begin{pmatrix} 5.6 \cdot 10^{-14} \\ 1.9 \cdot 10^{-28} \\ 1.0 \cdot 10^{-14} \end{pmatrix}. \tag{5.21}$$

The result is in good agreement with the theoretical prediction. The simulation can now be repeated under the assumption of non-vanishing EDM values. Figure 5.17 shows the resulting tilt angles of the invariant spin axes and the corresponding theoretical predictions according to Equation (4.53). The simulation results match the theoretical values up to the numerical accuracy of Bmad.

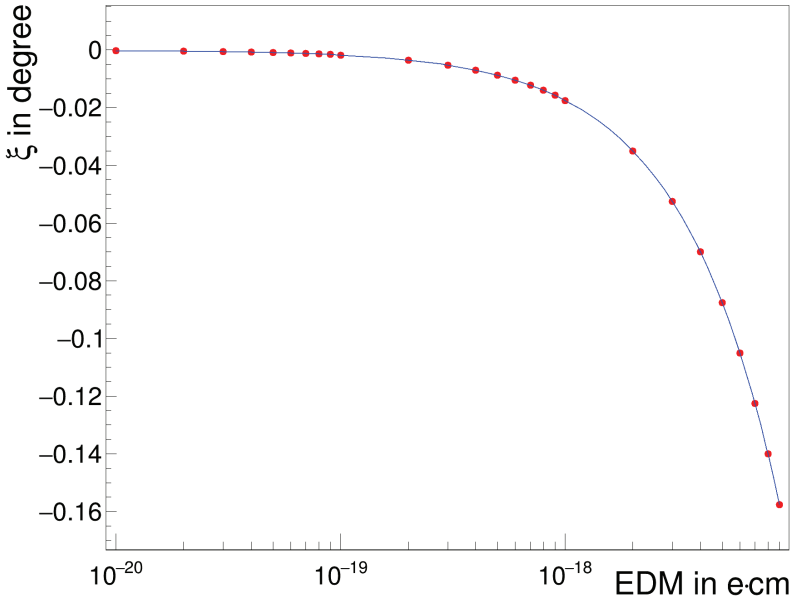

Figure 5.17: Determination of the invariant spin axis using spin tracking calculations. The plot shows the tilt angle ξ for different EDM values. The red dots represent the simulation results, the blue line indicates the theoretical predictions according to Equation (4.53).

6. Magnet Studies

So far, all elements of the simulation model are assumed to be ideally positioned and the impact of closely positioned elements with field overlaps were neglected. This chapter discusses the influence of magnet misalignments and the effective length of quadrupoles as well as field shortening effects on the beam and spin motion. Especially the prediction accuracy of the invariant spin axis is investigated.

6.1 Magnet Misalignments

Up to now, the COSY model assumes, that all magnets are perfectly mounted at their reference position. In reality, the elements in the machine have position offsets in all three dimensions and are rotated around all axes. These misalignments are a main source for systematic effects in the EDM experiment. A vertical spin buildup could for instance be the consequence of an additional radial magnetic field of a shifted quadrupole. In order to investigate all contributions of magnet misalignments to the spin motion, it is essential to measure the alignment of each single magnet in COSY and to readjust their positions to the reference position as precisely as possible. All dipoles and quadrupoles are equipped with reference marks on top of the magnet that can be used to measure the position and rotation offset using a laser based measurement setup. Figure 6.1 shows the geometric layout of these reference marks.
The survey is conducted on a regular basis by the company *Stollenwerk* [1] and the latest measurements were taken in Summer 2019 and communicated in January 2020. Figure 6.2 and Figure A.3 show the position misalignments Δx, Δy and Δs of all dipoles in each direction. The corresponding values for quadrupoles and the rotation errors α_x, α_y and α_s are displayed in Appendix A.3. In addition to the misalignment values, the plots show the measurement uncertainties that were determined by *Stollenwerk*. These errors are hardly visible due to their smallness compared to the misalignments themselves. The misalignments of sextupoles and steerers couldn't be measured, since they have no reference mark. The offsets of the beam position monitors along the ring were determined by a beam based alignment procedure in October 2019 such that a reliable orbit measurement can be performed [2].

The measurement results are implemented into the COSY model which leads to a distortion of the nominal closed orbit, i.e. the reference particle no longer

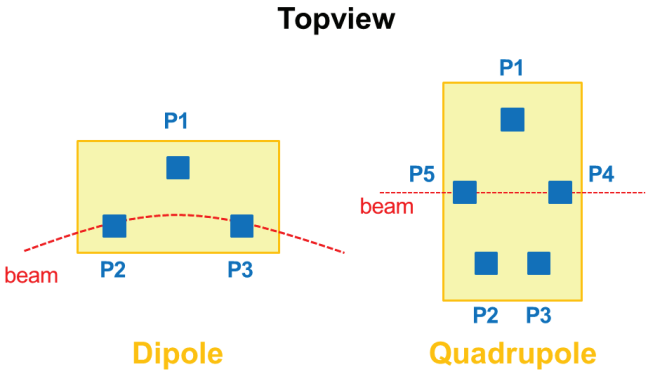

Figure 6.1: Geometric layout of the reference marks on top of the COSY dipoles and quadrupoles. The red line is the beam's reference orbit. A laser based system can be used in order to determine the positions and rotations of each dipole and quadrupole [39].

passes each magnet at its geometric center. As can be seen in Figure 6.3, the new closed orbits, indicated by the red and blue curve, show deviations in the millimeter range in both transverse directions. The corresponding betatron tunes ($Q_x = 3.62496$ and $Q_y = 3.63016$) only show small changes compared to ideally positioned magnets.
The spin motion is also influenced by the magnet misalignments. Using the algorithms from Section 5.5, the invariant spin axis turns out to be:

$$\vec{n}_{c,\mathrm{sim}} = \begin{pmatrix} -1.8508367770 \cdot 10^{-4} \\ 0.99999995714698 \\ -2.2682606262 \cdot 10^{-4} \end{pmatrix} \pm \begin{pmatrix} 2 \cdot 10^{-14} \\ 0.0008 \cdot 10^{-14} \\ 3 \cdot 10^{-14} \end{pmatrix}. \tag{6.1}$$

In comparison to the ideal lattice, where the invariant spin axis was perfectly aligned with the vertical axis, the invariant spin axis is now tilted in horizontal and longitudinal direction. Due to the misalignments and rotations of the magnets, the spin sees additional radial and longitudinal fields, that lead to non-commutative rotations of the invariant spin axis.

In order to study the stability of the simulated closed orbit, the misalignments of dipoles and quadrupoles are randomly changed according to a Gaussian distribution centered around zero:

$$\Delta\tilde{x} = \Delta x + \mathcal{N}(0, \sigma_{\Delta x}). \tag{6.2}$$

Equation (6.2) shows the random value generation for the horizontal offsets, where $\sigma_{\Delta x}$ denotes the measurement error provided by *Stollenwerk*. The calculation

for the remaining five misalignments is done in the same way. 10000 different random samples are generated and the closed orbit for each of them is calculated. The measurement uncertainties of the magnet positions directly translate into uncertainties on the simulated closed orbit. Figure 6.3 shows the 2σ bands in each direction, i.e. 95.45 % of all values lie within this interval. The spread of the closed orbit curves reach values up to the order of millimeters. This can have a large impact on the spin behavior if the orbit uncertainty is large at locations of quadrupoles. In order to test the stability of the invariant spin axis under closed orbit deviations due to the measurement uncertainties of the magnet misalignments, spin tracking calculations are performed for the same 10000 random seeds that were used for the closed orbit simulations. Figure 6.4 and Figure 6.5 display the tilt angles of the invariant spin axes in the y-x-plane (ξ) and y-s-plane (ζ). A Gaussian fit was performed to each data set and the standard deviation of the fit is considered to quantify the fluctuation of the angles. The fluctuation of the horizontal component yields $\pm\sigma_{n_x} = \pm 1.51504 \cdot 10^{-5}$. Transferring this interval into the tilt angle of the invariant spin axis in the y-x-plane gives a range of

$$-0.000200093\,\text{rad} \leq \xi \leq -0.000169793\,\text{rad}. \tag{6.3}$$

The corresponding EDM values that would lead to such a tilt lie within the interval

$$5.56166 \cdot 10^{-19}\ \text{e} \cdot \text{cm} \leq d \leq 6.55351 \cdot 10^{-19}\ \text{e} \cdot \text{cm} \tag{6.4}$$

with an average EDM value of

$$\bar{d} = 6.05734 \cdot 10^{-19}\ \text{e} \cdot \text{cm}. \tag{6.5}$$

A non-vanishing EDM shifts the distribution further to the left, since the EDM applies an additional tilt in the y-x-plane. Figure 6.6 shows the distribution when an EDM of $10 \cdot 10^{-18}\,\text{e}\,\text{cm}$ is assumed. The distribution with a vanishing EDM is shown as well. As expected, the width of both fits is equal, only the mean value is different. The difference of $\Delta\xi = -0.0003055$ radian fits well to the theoretical prediction of Equation (4.53).

The uncertainty of the invariant spin axis due to the limited measurement accuracy of the magnet misalignments can therefore be directly translated into a systematic limit of the EDM value that could be resolved in the precursor experiment. In order to estimate this limit, assume that on the one hand the only systematic error source is given by the magnet misalignments and that on the other hand the tilt angle ξ is only influenced by these misalignments and the contribution of a non-vanishing EDM. Then, a non-vanishing EDM produces an expected tilt angle according to:

$$\xi_{\mathrm{EDM}} = \xi_{\mathrm{measured}} - \mu_{\xi_{\mathrm{magnets}}}, \tag{6.6}$$

where ξ_{measured} represents the measurement value of all accumulated tilts and $\mu_{\xi_{\mathrm{magnets}}}$ denotes the expected value of the above depicted distribution for ξ_{magnets}. The minimal required value of ξ_{EDM} for the measured value ξ_{measured} to be significant at the $r \cdot \sigma$ level is then simply given by

$$\xi_{\mathrm{EDM}} = -r \cdot \sigma, \tag{6.7}$$

where σ is the width of the ξ_{magnets} distribution. The negative sign is introduced since the EDM tilts the invariant spin axis counterclockwise around the longitudinal axis within the coordinate system described in Section 3.2. For instance, the threshold angle for the 3σ level turns out to be

$$\xi_{\mathrm{EDM}} = -0.0000454215 \text{ rad} = -0.0026 \text{ deg}. \tag{6.8}$$

Using Equation (4.53), this angle can be transformed into a minimal resolvable EDM value of

$$d = 1.49 \cdot 10^{-19} \text{ e} \cdot \text{cm} \tag{6.9}$$

or

$$\eta_{\mathrm{EDM}} = 2.82766 \cdot 10^{-5}. \tag{6.10}$$

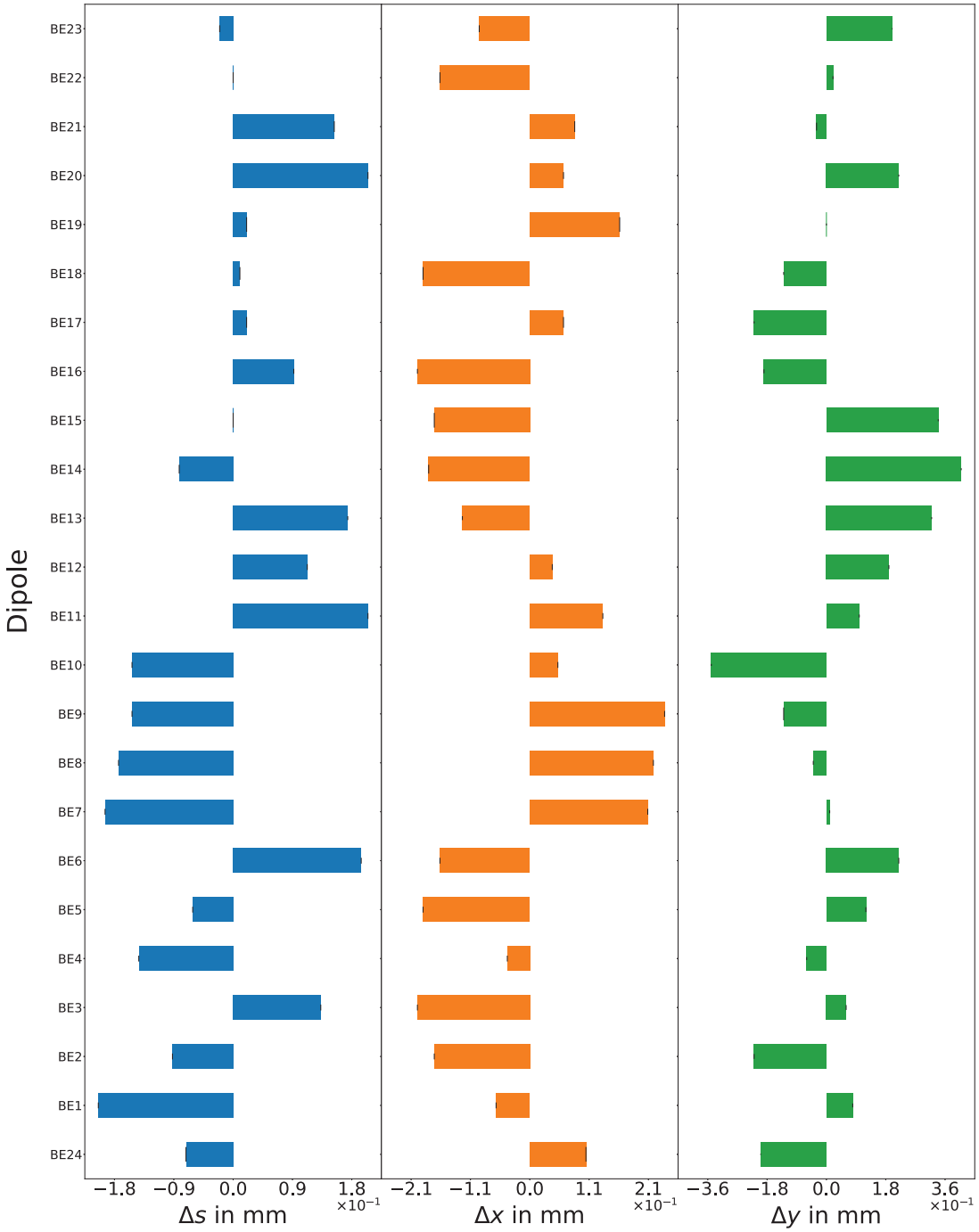

Figure 6.2: Measured misalignments of all dipoles including the measurement uncertainties. The individual 24 dipole magnets of COSY are denoted with B1, ..., B24. The measurements were performed in January 2020.

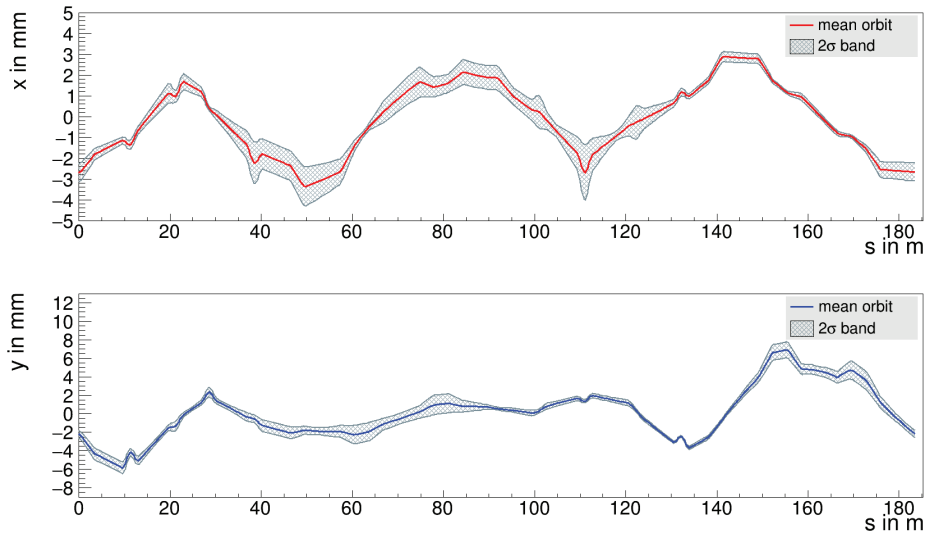

Figure 6.3: Closed orbits in horizontal and vertical direction including dipole and quadrupole misalignments. Both orbits (red and blue) show distortions of several millimeters compared to the default model with ideally positioned magnets. Additionally, a 2σ range is shown based on 10000 random settings according to Equation (6.2).

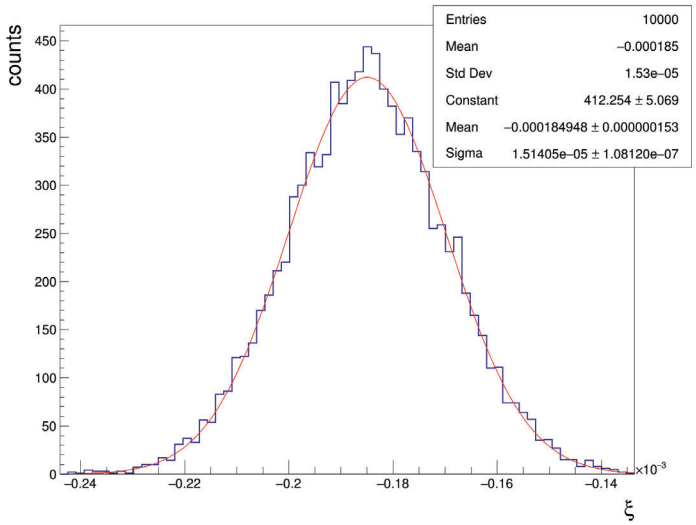

Figure 6.4: Distribution of tilt angles of the invariant spin axis in the y-x-plane for 10000 random Gaussian magnet misalignments. A Gaussian fit was performed to the data set. The mean value is equal to the tilt angle of the invariant spin axis when no random changes are applied and only the measured misalignments are taken into account. Note that the simulations are assuming a vanishing EDM ($\xi_{\mathrm{EDM}} = 0$).

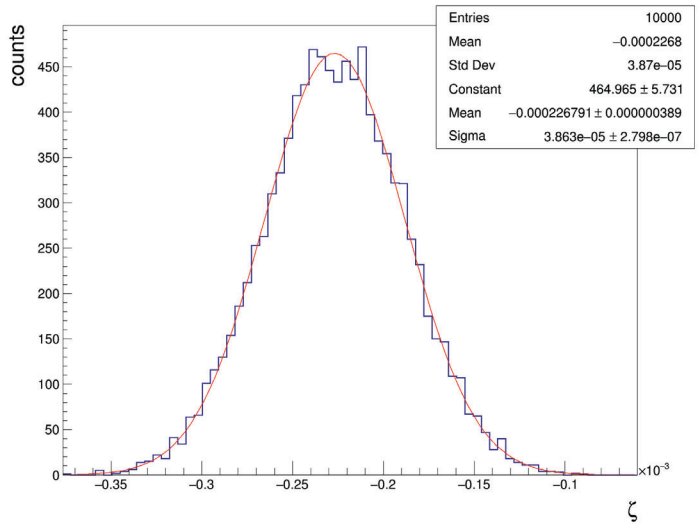

Figure 6.5: Distribution of tilt angles of the invariant spin axis in the y-s-plane for 10000 random Gaussian magnet misalignments. A Gaussian fit was performed to the data set.

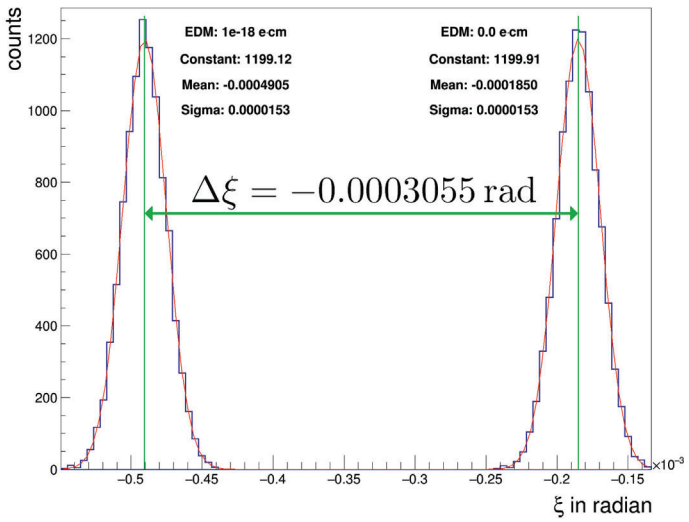

Figure 6.6: Distribution of tilt angles of the invariant spin axis in the y-x-plane for 10000 random Gaussian magnet misalignments. For the tracking calculations on the left, an EDM of 10^{-18} e cm was assumed. The distribution has the same shape and width as the one with a vanishing EDM (right). Only the mean value is shifted by the additional tilt angle described by Equation (4.53).

6.2 Field Studies

All previous simulation models as well as the default lattice within this thesis assume that the effective lengths of all magnets equal the values in Table 5.1. In this section, the effective lengths of the quadrupoles based on crosscheck measurements are discussed. Furthermore, the shortening of the effective lengths of dipoles and quadrupoles due to other magnets close by is investigated. The simulation results are compared to measurements that were taken in October 2019.

6.2.1 Effective Length of Quadrupoles

The effective lengths of the COSY quadrupoles in Table 5.1 are based on a moving-coil measurement that was performed for all magnets. The principle of this measuring method is based on the Faraday law of magnetic induction. In the dipole, a plane coil with n turns, a width b and a length l is axially aligned and rotated around the magnetic axis of the magnet under investigation [[82], [83], [84], [85]]. The electrical voltage

$$U = n\frac{\mathrm{d}\phi}{\mathrm{d}t} \tag{6.11}$$

resulting from the magnetic flux change $\frac{\mathrm{d}\phi}{\mathrm{d}t}$ in the coil ends is measured with an integrating voltmeter. As long as the coil moves in the homogeneous field, the value of the component of the magnetic induction perpendicular to the coil surface can be measured. With a long coil, which also covers the entire stray field, the integral

$$\int B_y \mathrm{d}s \tag{6.12}$$

is obtained directly, giving the quantity which, in the case of the dipole and a given momentum, produces the desired deflection of the ion beam. In case of a quadrupole, the plane coil is positioned azimuthally at a distance a from the magnetic axis and then the whole arrangement is rotated around the magnetic axis. Different coil lengths are also used here. The long coil, extended over the whole stray field, directly measures the focusing strength of the quadrupole. With the short coil, staying in the homogeneous area of the quadrupole field, one obtains the maximum field value at distance a, and thus the gradient

$$G_{\mathrm{QP}} = \frac{B_{\max}}{a} \tag{6.13}$$

inside the quadrupole.

The magnets are then characterized by their magnetic lengths

$$l_{\text{eff,dipole}} = \frac{1}{B_{\max}} \int B(s)\mathrm{d}s. \tag{6.14}$$

The accuracy and reproducibility of moving coil measurements is generally very high. A precise measurement can be evaluated with regard to the multipole components. The weak point is the possible systematic error caused by the accuracy with which the area is determined. It is obvious that this is especially important for short coils, which can cause errors in the accuracy of l_{eff}, especially for quadrupole measurements [[84], [85]].

Therefore, the effective lengths of one arc and one straight section quadrupole were determined directly in 1998/1999 using a 3D Hall probe. The Hall probe was moved at a distance d parallel to the magnetic axis across the entire stray field and the measured values were recorded at specific discrete intervals.
The accuracy of this measurement is much higher as long as the Hall probe behaves linearly in the measurement regime and is positioned accurately within the measurement setup. The effective lengths using the Hall probe differ significantly from the ones in Table 5.1:

$$l_{\text{eff,QU}} = 0.380 \text{ m} \tag{6.15}$$

$$l_{\text{eff,QT}} = 0.650 \text{ m}. \tag{6.16}$$

It is reasonable to take the reliable measurement of the focusing strength with the long coil as a basis to convert the old gradient values to the new ones which are based on the Hall probe measurements. It is also useful to operate with the current-specific gradients $g = G_{\text{QP}}/I$ of the field because a direct relation between quadrupole strengths values k and the currents I for the quadrupoles is easily obtained.
Therefore, the new gradient values can be calculated using:

$$l_{\text{eff,new}} \cdot g_{\text{new}} = l_{\text{eff,old}} \cdot g_{\text{old}}. \tag{6.17}$$

Using the old gradient values $g_{\text{QU,old}} = 0.0173\frac{\text{T}}{\text{mA}}$ and $g_{\text{QT,old}} = 0.0176\frac{\text{T}}{\text{mA}}$ the new values turn out to be:

$$g_{\text{QU}} = 0.01694 \ \frac{\text{T}}{\text{mA}} \tag{6.18}$$

$$g_{\text{QT}} = 0.01679 \ \frac{\text{T}}{\text{mA}}. \tag{6.19}$$

Quadrupole family	current in A	k_{old} in $\frac{1}{m^2}$	k_{new} in $\frac{1}{m^2}$
QT1	-104.087	-0.5661846983	-0.5401273343
QT2	96.115	0.5228207391	0.4987591029
QT3	136.938	0.7448788054	0.7105974512
QT4	-126.581	-0.6885415594	-0.656852999
QT5	-116.234	-0.6322587088	-0.6031604387
QT6	107.893	0.5868875619	0.5598773957
QT7	-117.322	-0.6381769210	-0.6088062786
QT8	106.080	0.5770256881	0.5504693922
QU1	-55.459	-0.2965289544	-0.2903584097
QU2	71.026	0.3797628070	0.3718602284
QU3	-55.459	-0.2965289544	-0.2903584097
QU4	85.779	0.4586443531	0.4491003088
QU5	-55.459	-0.2965289544	-0.2903584097
QU6	71.026	0.3797628070	0.3718602284

Table 6.1: Quadrupole strength settings of the COSY model for old and new effective lengths of the quadrupoles. The quadrupole strengths are calculated according to the current settings of the beam time in October 2019 and the measured field gradients. Each quadrupole family comprises four single quadrupoles. The arc quadrupoles are indicated by the letter "U", the ones in the straight sections are labeled with "T". A positive quadrupole strength represents a quadrupole that is horizontally focusing and vertically defocusing.

With the new gradient values, the corresponding quadrupole strengths can be calculated using the current settings at the quadrupole power supplies. Table 6.1 summarizes the current values for each quadrupole as well as the resulting strengths values for the new and the old effective lengths. The currents in Table 6.1 correspond to the ones that were used during the measurement in October 2019.

The new effective lengths are implemented into the Bmad model by on the one hand adding half of the difference to each side of the magnet and on the other hand reducing the drift sections on each side of the magnet such that the total length of the ring is conserved. Figure 6.7 shows the old and the new simulated optical functions. Since the lens strength is the same for both lengths, the changes of the optical functions are small. However, the betatron functions look more symmetric using the new quadrupole lengths. Especially, in the arc sections, the vertical betatron function shows a slightly better tuned pattern as before since the two peaks in the arcs have the same height now. The new tunes are slightly smaller than before, since the new quadrupoles are thicker and thus the focal

lengths are longer.

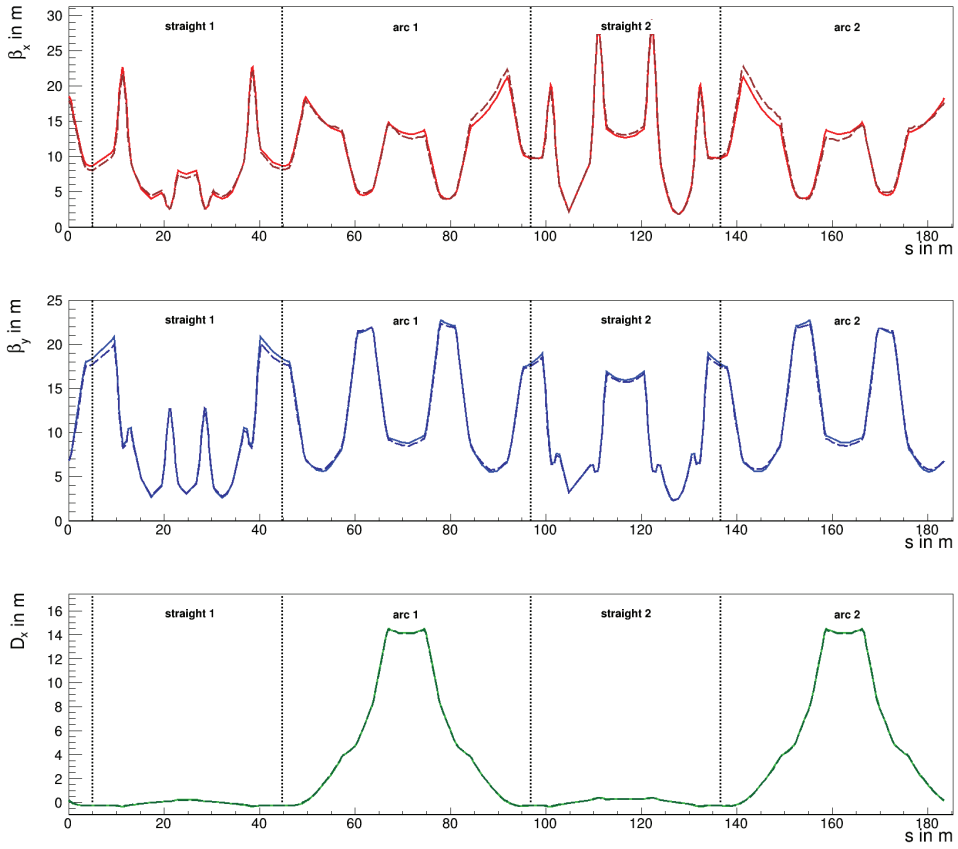

Figure 6.7: Optical functions β_x, β_y and D_x for the quadrupole strengths given in Table 6.1. The optical functions for the old effective quadrupole lengths is given by the solid lines, the optics according to the new effective lengths is shown by the dashed lines. The betatron tunes for the old lattice are $Q_x = 3.68915$ in horizontal direction and $Q_y = 3.72521$ in vertical direction., the ones for the new lattice are $Q_x = 3.66564$ and $Q_y = 3.70662$.

The effect on the invariant spin axis for the reference particle within an ideal lattice is at the order of 10^{-15} and therefore negligible. Introducing again the misalignments from Section 6.1, the tilt of the invariant spin axis in the x-y plane and the s-y plane differs by:

$$\Delta\xi = 18.2 \text{ mrad} = 1.04 \cdot 10^{-3} \text{ deg}, \tag{6.20}$$

$$\Delta\zeta = -4.4 \text{ mrad} = -2.5 \cdot 10^{-4} \text{ deg}. \tag{6.21}$$

It is therefore not negligibly small but is not sufficient to explain the large difference between simulation model and measurement (see Chapter 7).

6.2.2 Effective Length of Dipoles

The effective length measurement described above determines the effective length of a single detached magnet. Being installed into COSY, the situation for some magnets turns out to be different. Due to the close positioning of the magnets, their effective lengths can be influenced by the fields of the surrounding magnets. The following simulations are based on the studies in [86] and contain first, rough approximations to study the effect on the guiding dipoles in COSY.

The iron of close-by steerer magnets interacts with the fringe fields of the dipoles and the effective length of the COSY dipoles is shortened. Thus, the guiding of the beam no longer equals the designed bending of 15 degree per dipole. Field simulations show, that an H-type steerer at a distance of 216 mm reduces the effective length of a dipole by 0.34 %. Another calculation shows the effect of a C-type steerer at a distance of 222 mm to the dipole resulting in a reduction of the effective length of 0.26 % [86]. The effect on the beam can be described by a kick inside each dipole where the kick intensity depends on the individual environment of the dipoles. Estimations for the kicks were deduced by H.J. Stein [87] by considering the distance between the affected dipoles and the magnets in the proximity. The kick values were then calculated using the simulation results in [86]. They are summarized together with the corresponding dipole names in Table 6.2. More sophisticated field calculations are in process and will be used in the future to further study the effect in more detail. The kicks are implemented by using steerers with zero length in the center of each dipole magnet. In Bmad, this can be done by simply overlaying the two elements and giving the steerer a length of zero.
Applying these kicks, the horizontal closed orbit is highly distorted as can be seen in Figure 6.8 which shows the closed orbits for ideal magnets on the top and for simulations including the misalignments from Section 6.1 on the bottom. The horizontal closed orbit is dominated by the large impact of the additional kicks due to shorter effective dipole lengths. As expected, the vertical closed orbit is not affected. Without the quadrupoles, there would be no stable solution. The quadrupoles in the arcs steer the beam back such that a total bending of 360 degrees is ensured. The effect of effectively shortened dipoles is usually covered during machine running since the orbit correction acts contrary to all orbit distortions. During the measurements in October 2019, the orbit correction was turned off in order measure the pure uncorrected orbit. The result can be seen in Figure 6.9, where the simulation results including the magnet misalignments and the shortening of the dipole lengths are compared to the measurement results. The large orbit distortion in horizontal direction is clearly visible in the measurement and the shape of the simulated and the measured orbit show large similarities. The vertical orbits both show distortions in the same order of magnitude. However, their overall shapes differ more than the one in horizontal

dipole name	kick in mrad
BE3	0.7
BE4	0.5
BE5	0.7
BE6	0.5
BE9	0.5
BE10	0.6
BE11	0.6
BE14	0.7
BE16	0.5
BE19	0.5
BE21	0.5
BE22	1.2
BE24	0.7

Table 6.2: COSY dipoles that are influenced due to the magnetic fields of close by sextupoles and steerer magnets. The effect on the effective length of the dipoles can be translated into a kick affecting the beam motion. The kick values are first estimations based on the studies of [86].

direction. Although the simulation is performed on a very first, rough estimate of the effect, the results clearly show, that shorter effective lengths of the dipoles have a large influence on the orbit. It is therefore crucial to further study the effect in more detail using sophisticated measurements and simulations. The effectively shortened dipole lengths also affect the spin motion. For an ideal lattice, the simulated invariant spin axis still points along the vertical axis, but the spin tune is reduced since the total integrated vertical magnetic field is now smaller:

$$\nu_S = 0.1589195769463 \pm 1 \cdot 10^{-13}. \tag{6.22}$$

In combination with the magnet misalignments, the invariant spin axis changes especially in the horizontal component and gets an additional tilt of $\Delta\xi = -0.28$ mrad (compare to Equation (6.1)):

$$\vec{n}_{c,\mathrm{sim}} = \begin{pmatrix} -4.65009155301 \cdot 10^{-4} \\ 0.999999858995368 \\ -2.56467794858 \cdot 10^{-4} \end{pmatrix} \pm \begin{pmatrix} 5.953 \cdot 10^{-12} \\ 0.004 \cdot 10^{-12} \\ 11.189 \cdot 10^{-12} \end{pmatrix}. \tag{6.23}$$

6.2.3 Fringe Fields

So far, all magnets within the simulation model were considered to have no fringe fields, meaning no fields that extend the actual geometrical limits of the defined

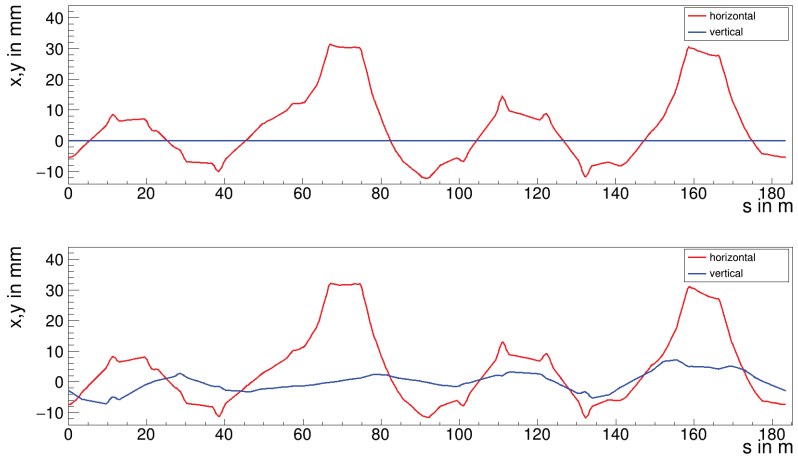

Figure 6.8: Horizontal (red) and vertical (blue) closed orbit resulting from shortened effective dipole length with an underlying ideal lattice (top) and including magnet misalignments (bottom). The horizontal closed orbit is clearly dominated by the shorter effective lengths of the dipoles which leads to orbit distortions up to 32 mm.

elements. However, fringe fields contribute to the spin precessions and it is therefore necessary to study them systematically. Bmad offers an already sophisticated description of fringe fields that are based on the analytical approaches in [88, 89, 90]. Starting again with the default lattice and turning on these fringe fields for the dipoles and quadrupoles leads first of all to a vertical tune shift:

$$Q_{y,\text{default}} = 3.63061 \;\rightarrow\; Q_{y,\text{fringe}} = 3.60172. \tag{6.24}$$

To study the effect on the invariant spin axis, the magnet misalignments from Section 6.1 are again considered in addition. The effect of the fringe fields on the invariant spin axis turns out to be small compared to the simulation result without fringe fields (Equation (6.1)):

$$\Delta\vec{n}_{c,\text{sim}} = \begin{pmatrix} -0.1261637 \cdot 10^{-4} \\ -5.48 \cdot 10^{-9} \\ -0.1313489 \cdot 10^{-4} \end{pmatrix}. \tag{6.25}$$

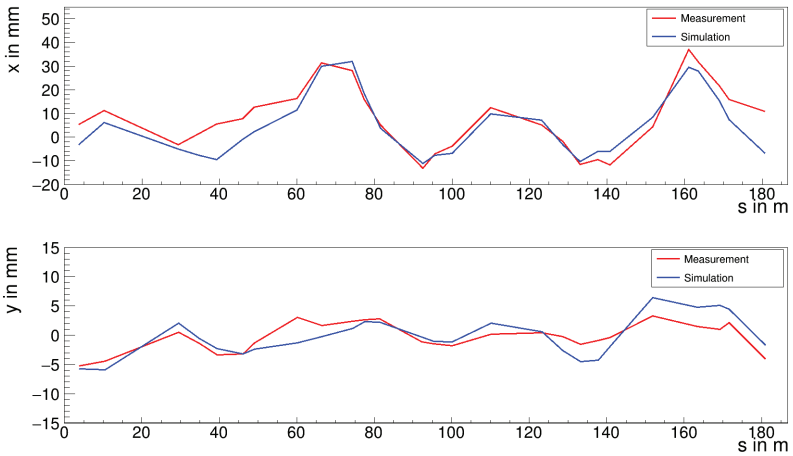

Figure 6.9: Simulated and measured orbit in horizontal and vertical direction. The simulation includes the additional kicks due to the shortening of the effective lengths of the dipoles and the magnet misalignments from Section 6.1. For the measurement, the orbit correction was turned off in order to see the uncorrected orbit that is present when only the dipoles and quadrupoles are turned on.

7. Model Fitting Methods

In this chapter, the major differences between the simulation model and measurements are discussed. Furthermore, the chapter describes sophisticated algorithms to fit various model parameters in order to achieve a better description of the real machine.

So far, various systematic effects were added to the default simulation model and their impact on the beam and spin motion was investigated. In order to see how well the model describes the measured beam and spin quantities, all effects, i.e. the magnet misalignments, the effective length studies of dipoles and quadrupoles as well as the fringe fields are now combined. The dipole, quadrupole, sextupole and steerer strengths are set to the values of the October 2019 measurement. Figure 7.1 shows the resulting simulated closed orbits as well as the measured ones.

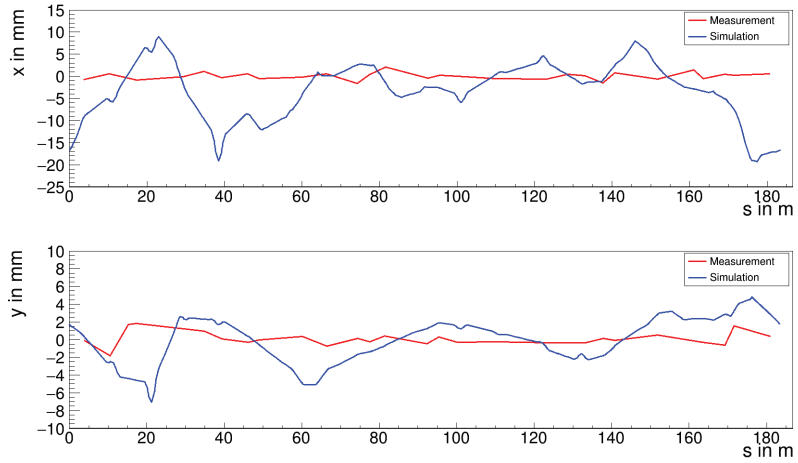

Figure 7.1: Simulated and measured orbit in horizontal and vertical direction. The simulation includes the changed effective length of dipoles and quadrupoles and the magnet misalignments from Section 6.1. The magnet settings (dipoles, quadrupoles, sextupoles and steerers) from the measurements in October 2019 were used for the simulation.

The simulated betatron tunes turn out to be:

$$Q_{x,\mathrm{sim}} = 3.675333, \tag{7.1}$$
$$Q_{y,\mathrm{sim}} = 3.669646. \tag{7.2}$$

On the other hand, the measured tunes with the same underlying magnet settings are:

$$Q_{x,\mathrm{meas}} = 3.570458, \tag{7.3}$$
$$Q_{y,\mathrm{meas}} = 3.585893. \tag{7.4}$$

Neither the simulated orbits nor the corresponding betatron tunes match the measured values. However, by switching off the steerers again and comparing the simulation result and the measured orbits (see Figure 6.9) the simulation model shows a much better overlap with the measurement. It is therefore obvious that the implementation of the archived steerer values leads to the large mismatch of simulation results and measurements. The values are stored in terms of percentage values relative to the maximum possible current of each steerer. In order to translate those values into steerer kicks, calibration factors are needed. Unfortunately, the list of calibration values is incomplete[1] and the values were measured at a different energy than the actual precursor experiment. Therefore, the chance of miscalculating the steerer kicks is one of the major uncertainties when running the simulation model. New measurements of the calibration factors for all steerers are planned in the future. Until then, the simulation model can be used to estimate the steerer kicks so that they fit the measurement well.

7.1 Orbit Response Matrix and Orbit Correction

Due to the magnetic structure of the accelerator the closed orbit deviates from the trajectory through all magnet centers. Considering field imperfections, magnet misalignments and other external effects on the beam, the closed orbit changes and its deviations get larger. To ensure an orbit that resembles the desired target orbit as closely as possible, a correction system is needed. In many cases the target orbit is equal to the trajectory through the magnet centers but one can also imagine desired orbits with $x \neq 0$ and $y \neq 0$. To manipulate the orbit, additional dipoles are used to steer the beam in vertical and horizontal direction. In order to find the best field strength configurations of these corrector magnets it is essential to know the influence of every single corrector on the orbit. The orbit response due to perturbations at one of the corrector magnets can be measured

[1] Many steerers have been dismounted or replaced over many years of COSY operation.

using the beam position monitors. Note, that these measurements only take place at discrete positions and that the largest parts of the true orbit stay unobserved. An unfavorable distribution of BPMs could lead to a situation, where large, local orbit distortions are not recognized by the measurements and to which the orbit correction therefore cannot react. Minimizing the BPM orbit readings therefore only represents the optimal correction method if the electronic or mechanical offsets of the BPMs with respect to the adjacent quadrupoles are removed [91].

Assuming m BPMs and n corrector dipoles the m-dimensional vector $\vec{x}$ represents the measured orbit with respect to the path through the magnet centers. The orbit response due to perturbations at the corrector magnets can be written as

$$\Delta\vec{x} = \mathbf{R}\Delta\vec{\theta}, \tag{7.5}$$

with $\Delta\vec{\theta}$ summarizing all corrector strengths. The $m \times n$ dimensional matrix $\mathbf{R}$ is the so called orbit response matrix (ORM) that describes all BPM responses i $(i = 1, ..., m)$ to a perturbation at corrector j $(j = 1, ..., n)$. The matrix elements are given by

$$R_{ij} = \frac{\Delta x_i}{\Delta\theta_j}. \tag{7.6}$$

The orbit response matrix can also be calculated knowing the optical functions. Assuming vanishing coupling of the horizontal and vertical beam dynamics the matrix entries can be found using [92]:

$$\text{vertical}: R_{ij} = \frac{\sqrt{\beta_{y,i}\beta_{y,j}}}{2\sin(\pi Q_y)}\cos(\Psi_{y,i} - \Psi_{y,j} - \pi Q_y), \tag{7.7}$$

$$\text{horizontal } R_{ij} = \frac{\sqrt{\beta_{x,i}\beta_{x,j}}}{2\sin(\pi Q_x)}\cos(\Psi_{x,i} - \Psi_{x,j} - \pi Q_x) - \frac{D_i D_j}{\left(\alpha_p - \frac{1}{\gamma^2}\right)C}, \tag{7.8}$$

where $Q_{x/y}$ denotes the betatron tune, $\beta_{x/y,i/j}$ are the betatron functions at the respective position of the BPM i and the corrector j and $(\Psi_i - \Psi_j)$ describes the phase advance between BPM and corrector magnet. For the horizontal orbit an additional term is added in order to account for dispersive effects when the cavity is switched on. Here, $D_{i/j}$ is the dispersion function at the BPM and the corrector magnet respectively, α_p is the momentum compaction factor and γ denotes the Lorentz factor.

An efficient orbit correction uses the orbit response matrix to determine the set of corrector strengths that lead to the desired orbit. With a given target orbit $\vec{x}_{\text{tar}}$ the condition under which the problem has to be solved reads

$$\Delta\vec{x} \stackrel{!}{=} \vec{x}_{\text{tar}} - \vec{x}. \tag{7.9}$$

Since the dimensions of the orbit response matrix depend on the number of BPMs and correctors, $\mathbf{R}$ is not always invertible. For a set of less correctors than BPMs there is in general no analytical solution. Besides solving for $\Delta\vec{\theta} = \mathbf{R}^{-1}\vec{x}$ one minimizes the residual error $\delta \equiv ||\mathbf{R}\Delta\vec{\theta} - \Delta\vec{x}||$ with respect to $\Delta\vec{\theta}$:

$$\delta = \sqrt{(\mathbf{R}\Delta\vec{\theta} - \Delta\vec{x})^2} \rightarrow \text{min!}. \tag{7.10}$$

Squaring Equation (7.10) and taking the derivative with respect to $\Delta\vec{\theta}$ yields

$$\frac{\partial\delta^2}{\partial\Delta\vec{\theta}} = 2\mathbf{R}^T(\mathbf{R}\Delta\vec{\theta} - \Delta\vec{x}) \stackrel{!}{=} 0 \tag{7.11}$$

$$\Rightarrow \quad \Delta\vec{\theta} = (\mathbf{R}^T\mathbf{R})^{-1}\mathbf{R}^T\Delta\vec{x}. \tag{7.12}$$

7.2 Orbit Matching Procedure

Starting with the idea of fitting the steerer strength in a way that the overall simulation result matches the measured orbits, an approach is chosen that uses the procedure of an orbit correction. Instead of setting the target orbit to zero, it is now set to be the measured orbit. Therefore, Equation (7.9) is now written as:

$$\Delta\vec{x} \stackrel{!}{=} \vec{x}_{\text{meas}} - \vec{x}_{\text{simulation}}. \tag{7.13}$$

The orbit response matrix of the model $\mathbf{R}_{\text{sim}}$ is determined by using Equation (7.7) and Equation (7.8). Since the number of BPMs at COSY ($m = 63$) is larger than the number of steerer magnets ($n = 41$), there is no analytical solution for the matrix inversion $(\mathbf{R}^T\mathbf{R})^{-1}$ in Equation (7.12). A common way of calculating the pseudo-inverse of this term uses the Singular Value Decomposition (SVD) [93].

7.2.1 Singular Value Decomposition

The decomposition of a matrix $\mathbf{Z} \in \mathbb{R}^{m\times n}$ in its singular values is expressed by

$$\mathbf{Z} = \mathbf{U}\mathbf{\Sigma}\mathbf{V}^{\mathbf{T}}, \tag{7.14}$$

where the singular values σ_i are collected in the diagonal matrix $\mathbf{\Sigma} \in \mathbb{R}^{m\times n}$:

$$\mathbf{Z} = \left(\begin{array}{ccc:ccc} \sigma_1 & & & & \vdots & \\ & \ddots & & \cdots & 0 & \cdots \\ & & \sigma_n & & \vdots & \\ \hdashline & \vdots & & & \vdots & \\ \cdots & 0 & \cdots & \cdots & 0 & \cdots \\ & \vdots & & & \vdots & \end{array}\right), \text{ with } \sigma_1 > \sigma_2 > ... > \sigma_n > 0. \tag{7.15}$$

Since matrices $\mathbf{U} \in \mathbb{R}^{m\times m}$ and $\mathbf{V} \in \mathbb{R}^{n\times n}$ are unitary, they fulfill the following condition:

$$\mathbf{U}\mathbf{U}^T = \mathbf{V}^T\mathbf{V} = \mathbf{1}. \tag{7.16}$$

Assuming the inverse of $\mathbf{Z}$ exists, it can be written as:

$$\mathbf{Z}^{-1} = \mathbf{V}\mathbf{\Sigma}^{-1}\mathbf{U}^T. \tag{7.17}$$

Using the SVD of the orbit response matrix $\mathbf{R} = \mathbf{U}\mathbf{\Sigma}\mathbf{V}^T$, the solution of the minimization problem given in Equation ((7.11)) reads:

$$\begin{aligned} \Delta\vec{\theta} &= (\mathbf{R}^T\mathbf{R})^{-1}\mathbf{R}^T\Delta\vec{x} && (7.18)\\ &= ((\mathbf{U}\mathbf{\Sigma}\mathbf{V}^T)^T(\mathbf{U}\mathbf{\Sigma}\mathbf{V}^T))^{-1}(\mathbf{U}\mathbf{\Sigma}\mathbf{V}^T)^T\Delta\vec{x} && (7.19)\\ &= (\mathbf{V}\mathbf{\Sigma}\mathbf{U}^T\mathbf{U}\mathbf{\Sigma}\mathbf{V}^T)^{-1}(\mathbf{V}\mathbf{\Sigma}\mathbf{U}^T)\Delta\vec{x} && (7.20)\\ &= (\mathbf{V}\mathbf{\Sigma}^{-2}\mathbf{V}^T)(\mathbf{V}\mathbf{\Sigma}\mathbf{U}^T)\Delta\vec{x} && (7.21)\\ &= \mathbf{V}\mathbf{\Sigma}^{-1}\mathbf{U}^T\Delta\vec{x} && (7.22) \end{aligned}$$

For the implementation of the orbit matching algorithm, the Linear Algebra PACKage (LAPACK) was used [94].

7.2.2 Simulation Results

After implementing the orbit matching algorithm, it is benchmarked to test its efficiency. The maximum allowed steerer kick change of the simulation is set to 2 mrad in order to exclude unrealistic solutions. Therefore the matching result can improve if several iterations of the algorithm are performed in order to correct non-linear effects. A distorted orbit is simulated by randomly applying kick values to the steerer magnets in the default simulation model. The kicks are distributed according to a Gaussian distribution around zero with a width of 0.5 mrad:

$$\Delta\tilde{\theta}_i = \mathcal{N}(0, 0.0005) \text{ with } i \in \{0, ..., n\}, \tag{7.23}$$

where n is the total number of steerers. After distorting the steerer settings of the simulation model, the algorithm is applied and the resulting closed orbit as well as the steerer settings are stored after each iteration. Figure 7.2 depicts the closed orbit RMS values in the horizontal and vertical direction for each iteration. Already after three iterations, the closed orbit RMS is reduced by seven orders of magnitude. The progress of the algorithm for each iteration can also be seen in Figure 7.3 showing the steerer kick values after each iteration. The grey bars show the initial kick values according to the random generator. After four iterations, all steerer kicks are below 0.001 mrad which lead to a closed orbit that is almost perfectly set to zero at each position along the ring.

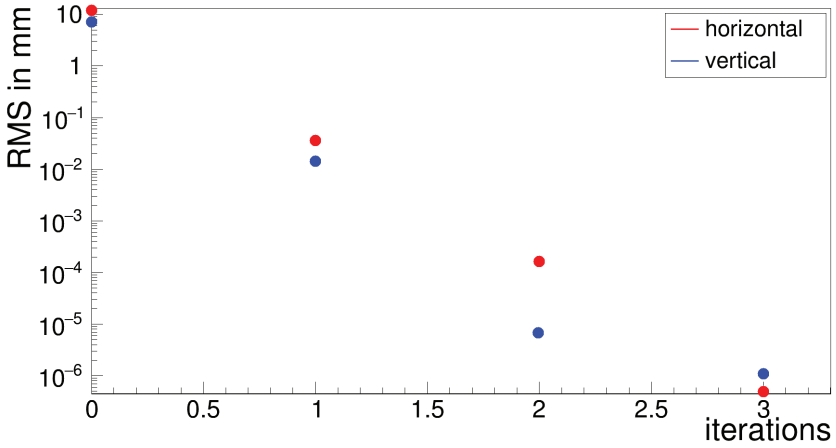

Figure 7.2: Closed orbit RMS values of the simulated orbits after each iteration of the orbit matching algorithm. The default simulation was initially distorted using randomly distributed steerer kicks. Afterwards, the algorithm step by step adjusts the steerer kicks so that the closed orbit becomes less and less distorted.

As a next step, the simulation model including all discussed systematic effects (see Chapter 6) including the magnet settings during the October 2019 measurements is taken as the basis for matching algorithm. The measured orbits now equal the target orbits in both transverse planes and three iterations of the matching procedure are performed. The decrease in the closed orbit RMS is shown in Figure 7.4. The dashed lines indicate the RMS values of the measured orbit, that have the following values:

$$\mathrm{RMS}_{\mathrm{x,measured}} = 0.79583 \text{ mm} \tag{7.24}$$
$$\mathrm{RMS}_{\mathrm{y,measured}} = 0.78059 \text{ mm}. \tag{7.25}$$

The vertical closed orbit RMS lies below the measured value already after the first iterations. The horizontal reaches this level after the next iteration. The

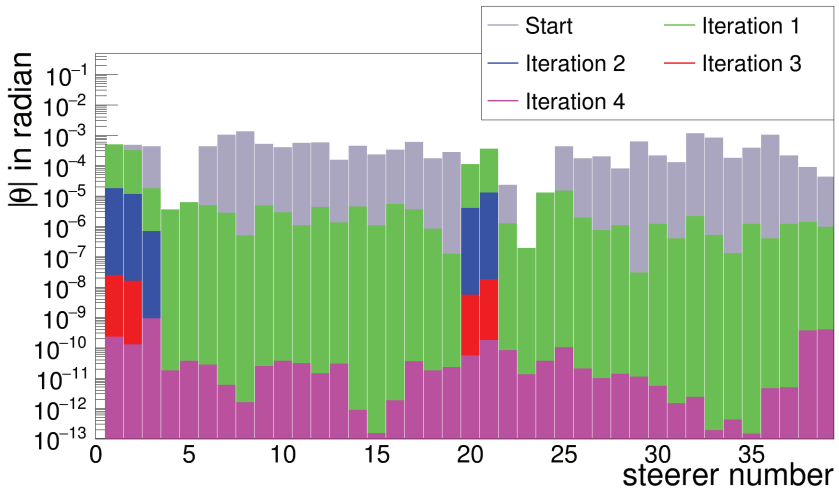

Figure 7.3: Steerer kick values in radian after each iteration of the orbit matching algorithm. The initial kicks are distributed according to a Gaussian distribution with a width of 0.5 mrad.

third iteration then has no further visible impact on the result. The final RMS values of the simulation after three iterations are:

$$\mathrm{RMS}_{\mathrm{x},\ 3^{\mathrm{rd}}\mathrm{iteration}} = 0.61415 \text{ mm} \tag{7.26}$$

$$\mathrm{RMS}_{\mathrm{y},\ 3^{\mathrm{rd}}\mathrm{iteration}} = 0.65048 \text{ mm}. \tag{7.27}$$

The final orbits after the third iteration can be seen in Figure 7.5. Compared to the initial situation displayed in Figure 7.1, the simulated orbits describe the measured one much better and show great agreements. A perfect match is in general not feasible since the number of corrector magnets is smaller than the number of BPMs and the resulting linear system of equation is therefore over-determined. In addition, the tilts of the orbits by main magnets (dipoles and quadrupoles) cannot be locally compensated, since the steerers are located between main magnets.
The preliminary measurement results of the invariant spin axis based on the data of the measurements in November 2018 gives the following tilt angles of the invariant spin axis in the x-y plane and y-s plane [95, 54]:

$$\xi_{\mathrm{meas}} \approx -3 \text{ mrad}, \tag{7.28}$$

$$\zeta_{\mathrm{meas}} \approx 5 \text{ mrad} \tag{7.29}$$

The invariant axis that is calculated on the results of the matching algorithm yields:

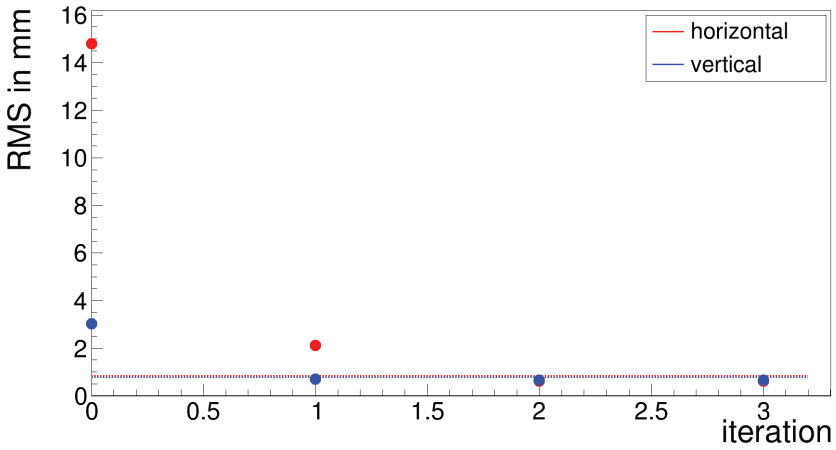

Figure 7.4: Closed orbit RMS values of the simulated orbits after each iteration of the orbit matching algorithm. Initially, all steerer kicks are set to zero. The target orbits are the measured orbits from the October 2019 beam time. The dashed lines (red: horizontal, blue: vertical) indicate the RMS values of the measured orbits.

$$\vec{n}_{c,\mathrm{sim}} = \begin{pmatrix} -2.155972934414 \cdot 10^{-3} \\ 0.999997303263848 \\ 8.63276165080 \cdot 10^{-4} \end{pmatrix} \pm \begin{pmatrix} 6.90 \cdot 10^{-13} \\ 2 \cdot 10^{-15} \\ 1.160 \cdot 10^{-12} \end{pmatrix} \tag{7.30}$$

and the corresponding tilt angles read:

$$\xi_{\mathrm{sim}} = -2.155975 \text{ mrad} \pm 6.904165 \cdot 10^{-10} \text{ mrad}, \tag{7.31}$$

$$\zeta_{\mathrm{sim}} = 0.863278 \text{ mrad} \pm 1.160218 \cdot 10^{-9} \text{ mrad}. \tag{7.32}$$

The order of magnitude and the sign of the two ξ values turn out to be the same and the simulated value for ζ approached the measured value as well.

Although the simulated closed orbits show a great overlap to the measurement and the difference in the invariant spin axis decreased as well by matching the orbits, the simulation model still cannot reproduce the measured betatron tunes (see Equations (7.24) and (7.25)). A possible reason could be gradient errors of the quadrupoles and the effect of other magnets in the vicinity of the quadrupoles so that the effective length is affected as discussed for the dipoles in Section 6.2. Since no reliable data exists for these systematic effects, another matching algorithm will be used that allows for several fit parameters simultaneously. The algorithm as well as the simulation results are discussed in the following Section.

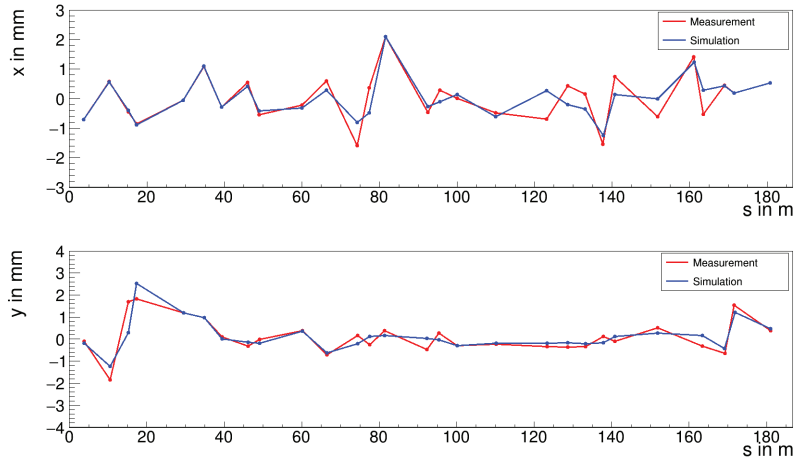

Figure 7.5: Simulated and measured orbits in horizontal and vertical direction. The simulation used the orbit matching algorithms over three iterations.

7.3 LOCO Algorithm

So far, the optimized simulation model is able do reproduce the measured orbits by fitting the steerer kicks. As a consequence, the orbit matching works well but other simulated quantities, like the betatron tunes and the spin tune differ from the measured values. One of the major parameters that affect the optics of a storage ring are the focusing and defocusing quadrupoles. Especially their positions and effective field strengths strongly influence the beam and spin motion. Although the quadrupole misalignments were measured, the beam based alignment studies have shown that some quadrupoles might have larger offsets that cannot be resolved by the laser based position measurements due to geometrical constraints [96]. In addition, magnets close to quadrupoles can affect the effective length of the quadrupole, similar to the dipole studies in Section 6.2. Furthermore, each quadrupole can have an individual gradient error due to manufacturing imperfections.

To further improve the model while varying all parameter of interest simultaneously, the so called Linear Optics from Closed Orbit (LOCO) technique is used. It was originally used as a calibration and correction tool for light sources [97, 98]. The method is based on a measured ORM that is compared to the ORM of the simulation model. The measured ORM contains thousands of points holding information about the machine optics and the focusing structure. It is therefore an appropriate instrument to determine the level of agreement between model and machine and moreover to improve the simulation model by fitting the ORM.

7.3.1 Basic Idea

So far, the orbit response to each steerer magnet was collected in a matrix. Below, this matrix is written as an orbit response vector $\vec{R}$ containing all entries of the ORM [92, 99]:

$$\vec{R} = \begin{pmatrix} R_{11} \\ R_{12} \\ \vdots \\ R_{mn}. \end{pmatrix} \tag{7.33}$$

The ORM analysis is based on the assumption that the orbit response vector $\vec{R}$ is a function of the machine parameters V_i:

$$\vec{R} = f(\vec{V}), \tag{7.34}$$

where $\vec{V}$ is the vector of all selected machine parameters. Typical parameters are quadrupole gradients, quadrupole positions or BPM positions and rolls [100, 101, 102]. In general, the list of parameters can be arbitrarily large. The machine parameters contain unknown errors relative to their design values and the ORM analysis algorithm is supposed to find them. Assuming small impacts of higher order effects, the Taylor series of the orbit response vector in linear order reads [92, 103]:

$$\vec{R}(\vec{V}) \approx \vec{R}(\vec{V_0}) + \mathbf{R}'(\vec{V_0})(\vec{V} - \vec{V_0}). \tag{7.35}$$

Here, $\vec{V_0}$ denotes the initial guess of the N machine parameters, usually given by the simulation model settings and $\vec{R}(\vec{V})$ describes the measured orbit response vector. Thus, $\vec{R}(\vec{V_0})$ is the model orbit response vector based on the initial guess of the machine parameters. The linear map $\mathbf{R}'(\vec{V_0})$ is the Jacobian, also denoted as J. It holds the information how the entries of the orbit response matrix vary with respect to the machine parameters in linear order. The difference of the simulated orbit response vector and the measured one can thus be described by the Jacobian matrix and the difference in the machine parameter vectors:

$$\Delta\vec{R} = \vec{R}(\vec{V})^{\text{meas}} - \vec{R}(\vec{V_0})^{\text{model}} = \mathbf{J}(\vec{V} - \vec{V_0}), \tag{7.36}$$

where the Jacobian reads:

$$\mathbf{J} = \begin{pmatrix} \frac{\partial\Delta R_{11}}{V_{0,1}} & \frac{\partial\Delta R_{11}}{V_{0,2}} & \cdots & \frac{\partial\Delta R_{11}}{V_{0,N}} \\ \frac{\partial\Delta R_{12}}{V_{0,1}} & \frac{\partial\Delta R_{12}}{V_{0,2}} & \cdots & \frac{\partial\Delta R_{12}}{V_{0,N}} \\ \vdots & \vdots & \vdots & \vdots \\ \frac{\partial\Delta R_{m(n-1)}}{V_{0,1}} & \frac{\partial\Delta R_{m(n-1)}}{V_{0,2}} & \cdots & \frac{\partial\Delta R_{m(n-1)}}{V_{0,N}} \\ \frac{\partial\Delta R_{mn}}{V_{0,1}} & \frac{\partial\Delta R_{mn}}{V_{0,2}} & \cdots & \frac{\partial\Delta R_{mn}}{V_{0,N}}. \end{pmatrix} \tag{7.37}$$

The interesting information in the process of improving the simulation model are the real machine parameter $\vec{V}$. It is therefore necessary to extract the difference vector $\Delta\vec{V} = \vec{V} - \vec{V}_0$. Multiplying Equation (7.35) with $\mathbf{J}^{-1}$, the difference of model parameters and real machine parameters can by written as:

$$\Delta\vec{V} = \vec{V} - \vec{V}_0 = \mathbf{J}^{-1}(\vec{R}(\vec{V})^{\text{meas}} - \vec{R}(\vec{V}_0)^{\text{model}}) = \mathbf{J}^{-1}\Delta\vec{R}. \tag{7.38}$$

The goal of the LOCO algorithm is decreasing the difference of the orbit response vectors $\Delta\vec{R}$. Therefore, a χ^2-minimization is performed where the χ^2 function is defined as the squared sum of the difference of the ORM entries [104]:

$$\chi^2 = \frac{|R_{ij}^{\text{meas}} - R_{ij}^{\text{model}}|^2}{\sigma_{ij}^2}. \tag{7.39}$$

The BPMs and steerer magnets are indicated by the indices i and j and σ_{ij} denotes the measurement uncertainties of the ORM. In order to implement the ORM analysis into the established Bmad library, the Jacobian is determined by varying the chosen machine parameters and performing linear fits for the response of each ORM entry. The calculation of the ORM itself was already implemented for the orbit matching algorithm and is now set corresponding to Equations (7.7) and (7.8). The inverse of the Jacobian matrix $\mathbf{J}^{-1}$ can again be obtained using the SVD method.

The implemented algorithm works as follows [92]:

1. Set the first guess for the real machine parameters $\vec{V}_0$ and apply them to the simulation model.
2. Determine the ORM of the simulation model $\mathbf{R}^{\text{model}}$ and reformat it into an orbit response vector $\vec{R}^{\text{model}}$.
3. Measure the ORM at the real machine by varying the steerer strengths and observing the changes of the BPM readings. This has to be done only once.
4. Compute the difference of the orbit response vectors $\Delta\vec{R}$.
5. Compute the Jacobian matrix $\mathbf{J}$: Vary the machine parameters in two directions and observe the changes in $\Delta\vec{R}$. Perform a linear fit for each entry of $\Delta\vec{R}$ and each machine parameter.
6. Determine the pseudo-inverse of the Jacobian matrix by using the SVD method.
7. Calculate a new set of machine parameter guesses using the results from Equation (7.38): $\vec{V}_0^{\text{new}} = \vec{V}_0^{\text{old}} + \Delta\vec{V}$.

8. Start the next iteration at step 1.

For a better understanding, the procedure is sketched in Figure 7.6. Several iterations of the algorithm can further improve the fitting results since the Jacobian matrix entries are based on linear fits. Non-linear effects therefore cannot be resolved within one iteration. After each iteration, the value of χ^2 is computed and the algorithm stops when a chosen threshold value is reached. The advantage of the ORM analysis is the fact that even in the case of more than one iteration, the ORM of the real machine has to be measured only once. All other quantities are based on the simulation model and do not need any measurement data as input.

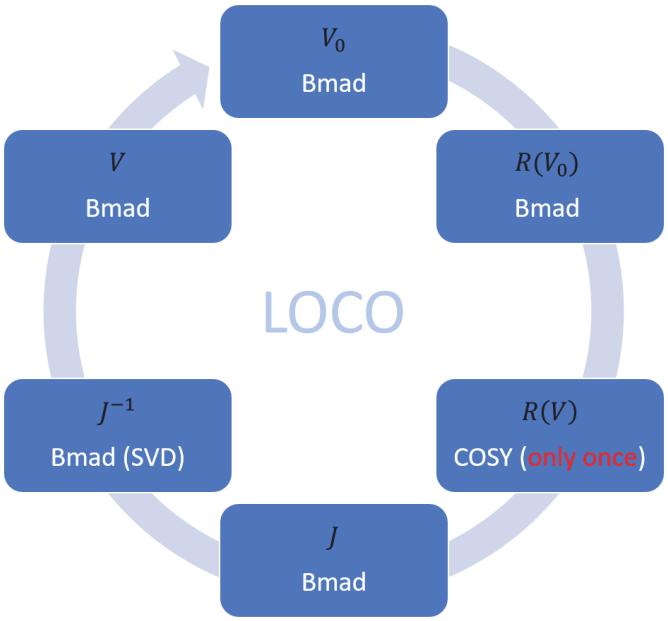

Figure 7.6: Working principle of the ORM analysis algorithm based on the LOCO method. All parts that are purely related to the simulation are marked with *Bmad*. The ORM has to be measured only once independently of the number of fitting iterations that are performed. After one cycle, the result of the current iteration is used to set the new machine parameter guess for the next iteration. Performing several iterations can lead to a better fit result since a single iteration cannot account for non-linear effects (adapted from [105]).

So far, the ORM analysis algorithm is discussed without any external constraints that might be applied to ensure stable beam conditions in between the iterations or to prevent unrealistic solutions. If the initial guess of the starting parameter settings is too far away from the real setup, the LOCO fitting might converge in an unrealistic way with very large changes of very few machine parameters. For instance, a very sensitive quadrupole could get an unrealistically large field whereas other magnets are not used at all for the fitting process. If the field

gets too large, the resulting Bmad model is unable to compute a closed orbit and the following iterations fail. Another inefficiency can appear due to the correlation between the fitting parameters, which usually exists between nearby quadrupoles. These quadrupoles act against one another and the reduction in χ^2 is small although the single quadrupole fields might be set to very high values [106, 107].

A very restrictive approach to avoid unrealistic fit solutions is the removal of singular values that are below a specific threshold value. Since removing a singular value is always coupled to a loss of information and could therefore affect the fitting accuracy, a less drastic approach is used below. The idea is based on penalty weights for each individual machine parameter such that the excursion solutions become less favorable. Therefore, the χ^2 function is modified by directly adding penalty terms to the use of machine parameters [106]:

$$\chi^2 = \sum_{ij} \frac{|R_{ij}^{\text{meas}} - R_{ij}^{\text{model}}|^2}{\sigma_{ij}^2} + \frac{1}{\sigma_0^2} \sum_{k}^{N_q} w_k^2 \Delta V_k. \tag{7.40}$$

The machine parameters are indicated by the index k and N_q represents the total number of machine parameters used in the fitting process. The individual weighting factors are denoted by w_k and a global normalization constant σ_0 is introduced. The modified merit function goes along with N_q additional linear equations in the minimization problem:

$$\Delta V_k = 0, \;\; k \in \{1, ..., N_q\}, \tag{7.41}$$

each weighted with $\frac{w_k^2}{\sigma_0^2}$. These equations can easily be implemented into the existing algorithm by modifying the difference vector $\Delta\vec{R}$ and the Jacobian matrix $\mathbf{J}$. The original Jacobian $\mathbf{J_0}$ is extended by N_q rows with non-zero elements:

$$J_{mn+k,k} = \frac{w_k}{\sigma_0}. \tag{7.42}$$

The final matrix then reads:

$$\mathbf{J} = \begin{pmatrix} & & \vdots & & \\ & \cdots & \mathbf{J_0} & \cdots & \\ & & \vdots & & \\ \frac{w_1}{\sigma_0} & 0 & 0 & \cdots & 0 \\ 0 & \frac{w_2}{\sigma_0} & 0 & \cdots & 0 \\ & & \vdots & & \\ 0 & 0 & \cdots & 0 & \frac{w_{N_q}}{\sigma_0}. \end{pmatrix} \tag{7.43}$$

The initial difference vector $\Delta\vec{R}_0$ is extended by N_q zeros and the new vector is given by:

$$\Delta\vec{R} = \begin{pmatrix} \Delta\vec{R}_0 \\ 0 \\ 0 \\ \vdots \\ 0 \\ 0 \end{pmatrix}. \tag{7.44}$$

The global minimum of the minimization problem is not changed by the additional constraints since the penalty costs are only applied to changes of the machine parameter in each iteration. Thus, the solution of the underlying problem stays the same, only the convergence path changes in a way that excursion solutions are avoided.

The individual weights w_k should be adjusted according to the performance of the algorithm. Setting an infinite penalty on a machine parameter is equivalent to the removal of a singular value. The weights have to be chosen properly: if they turn out to be too high, the simulation model converges too slowly and too many iterations are needed to reach the global minimum. If they are chosen to be too low, the algorithm will still run into unrealistic solutions and there is no benefit of using the penalty weights. In order to find a suitable set of weights, a calibration run is performed before the actual iterative fitting algorithm starts. The sensitive parameters can be identified by their individual χ^2 contribution. It is defined as the increase in χ^2 when the parameter is set to its initial value and meanwhile keeping all other parameters unchanged [106]. Very sensitive parameters with a high contribution will obtain a higher penalty weight, parameters with low sensitivity will get a lower weight respectively. The weights are calculated by globally scaling the χ^2 contributions to values where a stable solution is found by the simulation model. This is done in an iterative process starting with relatively high weights and successively decreasing them until the boundary to unstable motion is reached. The danger of oversized weights and inefficient convergence is therefore decreased.

7.3.2 Benchmarking

In order to test the algorithm and to ensure accuracy of the simulation, two different scenarios are investigated. In the first case, the quadrupole family settings are randomly distorted using a Gaussian distribution around zero with a width of 1 %. The distorted lattice takes the role of the measured lattice and the undisturbed model is the starting point of the algorithm. The threshold χ^2 value is set to:

$$\chi^2_{\text{threshold}} = 0.005. \tag{7.45}$$

In this case, the algorithm needs three iterations to end up with a χ^2 value below the threshold. The χ^2 values after each iteration are:

$$\text{Start} : \chi^2 = 801.6845 \tag{7.46}$$
$$1^{\text{st}} \text{ iteration} : \chi^2 = 64.5243 \tag{7.47}$$
$$2^{\text{nd}} \text{ iteration} : \chi^2 = 0.5510 \tag{7.48}$$
$$3^{\text{rd}} \text{ iteration} : \chi^2 = 0.0009. \tag{7.49}$$

Figure 7.7 depicts the difference ORM as well as the deviation of quadrupole family settings. The situation at the starting point is shown as well as the results after the first and third iteration, where the differences are almost perfectly zero. In the second scenario, the individual quadrupole gradients are randomly distorted, leading to an initial χ^2 value of $\chi^2 = 1132.73$. Again, the algorithm for this case needs three iterations to reach the χ^2 threshold value and the values after each step read:

$$\text{Start} : \chi^2 = 1132.7272 \tag{7.50}$$
$$1^{\text{st}} \text{ iteration} : \chi^2 = 47.0522 \tag{7.51}$$
$$2^{\text{nd}} \text{ iteration} : \chi^2 = 3.2837 \tag{7.52}$$
$$3^{\text{rd}} \text{ iteration} : \chi^2 = 0.0007. \tag{7.53}$$

The initial situation as well as the results after the second and third iteration are shown in Figure 7.8. In both scenarios, the algorithm was able to fit the model with high accuracy to the target lattice within only three iterations. The final magnet settings match the target ones and no excursion path to the minimum solution was taken. Combining both scenarios and randomly mismatching the quadrupole family settings as well as the individual quadrupole gradients can also be resolved by the algorithm. Here, the algorithm reaches the threshold χ^2 value after four iterations. The difference ORMs can be seen in Figure 7.9.

In general, arbitrarily many machine parameters can be included and fitted simultaneously with the LOCO algorithm. However, the ORM is not sensitive to every machine parameter group. While already small quadrupole gradients and positions marginally change the ORM entries, steerer kick changes do not lead to considerable changes in the ORM. Since the ORM entries are calculated on the basis of steerer changes, the initial steerer settings do not matter as long as they do not take extreme values where the orbit is dominated by non-linear effects. It is therefore questionable, if the involvement of steerer kicks into the vector of

machine parameters helps finding a realistic fit result. Nevertheless, the steerer kicks are one of the major unknown parameters when comparing the COSY model to the real machine. A reasonable approach is a step-wise fitting of quadrupole gradients, positions and steerer kicks. First, the quadrupole parameters are fitted using the LOCO algorithm. After reaching a minimum, the steerer kicks are then fitted in a next step using the orbit matching algorithm form Section 7.2.

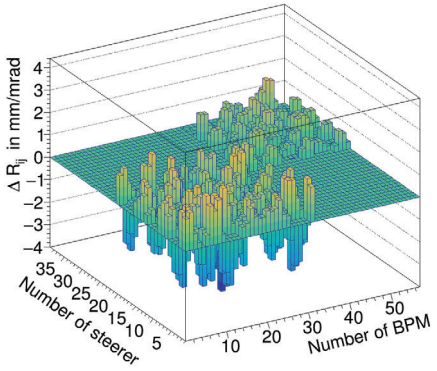

(a) Difference ORM at start.

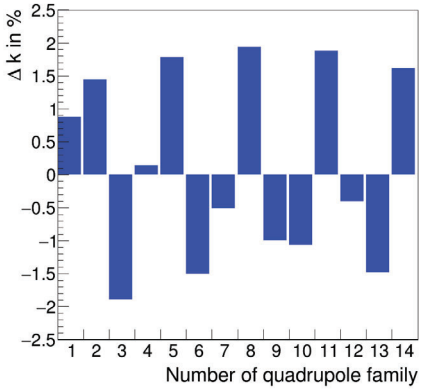

(b) Δk at start.

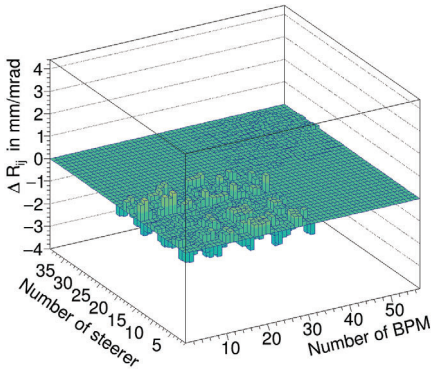

(c) Difference ORM after iteration 1.

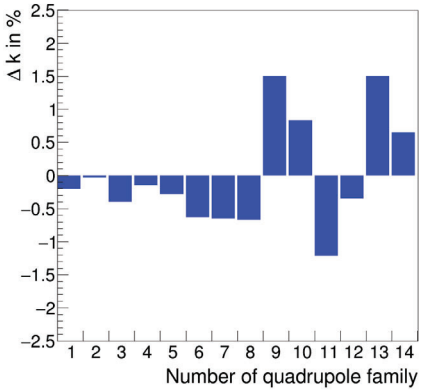

(d) Δk after iteration 1.

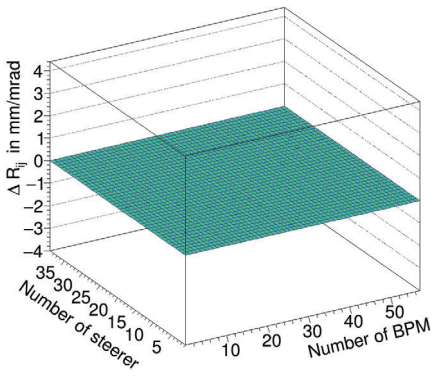

(e) Difference ORM after iteration 3.

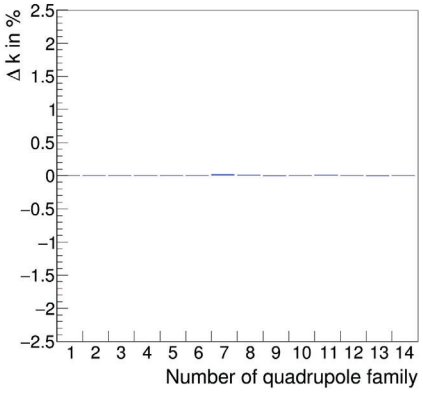

(f) Δk after iteration 3.

Figure 7.7: Evolution of the difference ORM and the difference of quadrupole family settings over three iterations. The initial offset is achieved by randomly disturbing the quadrupole family settings of the initial model lattice.

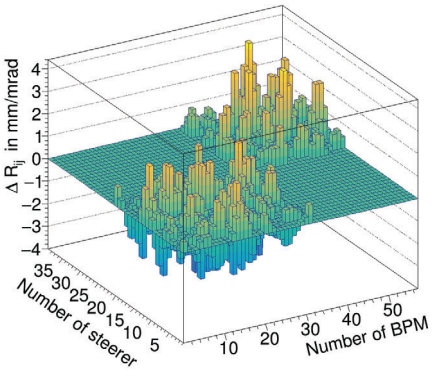

(a) Difference ORM at start.

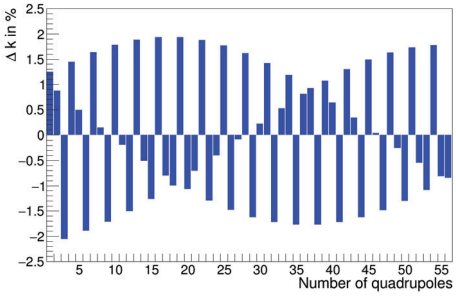

(b) Δk at start.

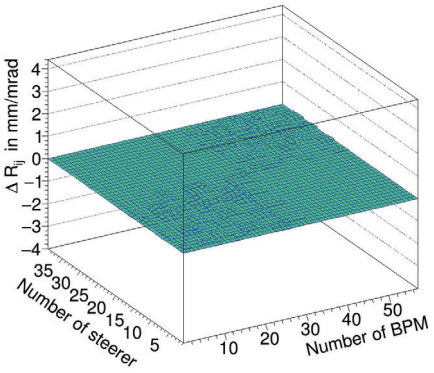

(c) Difference ORM after iteration 2.

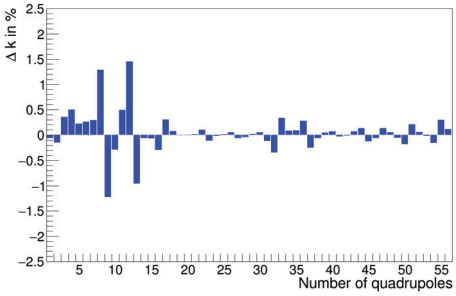

(d) Δk after iteration 2.

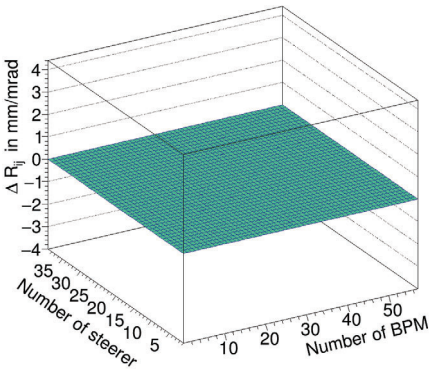

(e) Difference ORM after iteration 3.

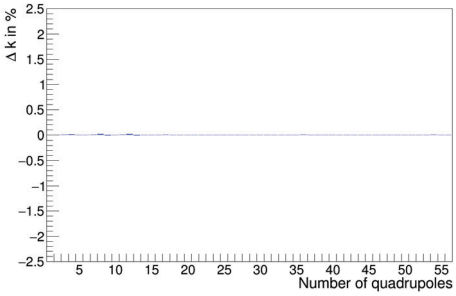

(f) Δk after iteration 3.

Figure 7.8: Evolution of the difference ORM and the difference of individual quadrupole gradient settings over three iterations. The initial offset is achieved by randomly disturbing the individual quadrupole gradients of the initial model lattice.

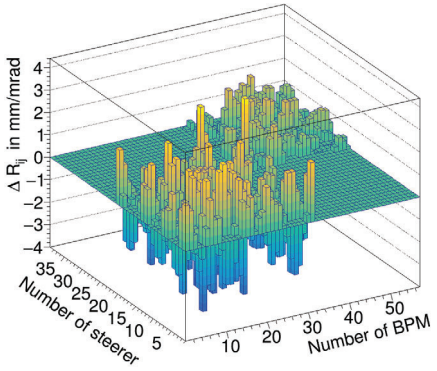

(a) Difference ORM at start.

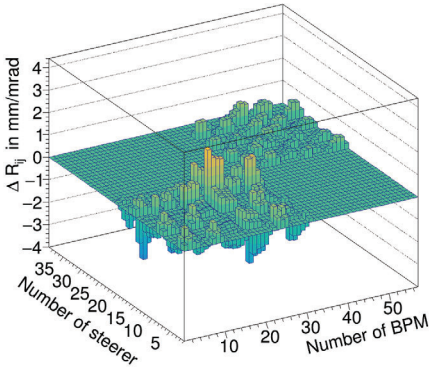

(b) Difference ORM after iteration 1.

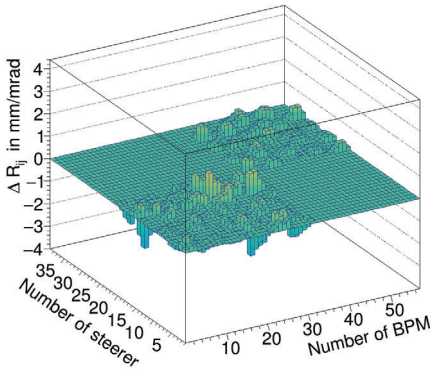

(c) Difference ORM after iteration 2.

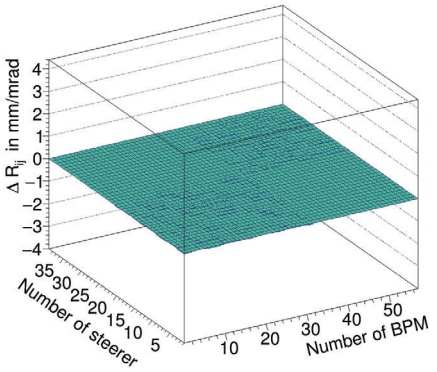

(d) Difference ORM after iteration 3.

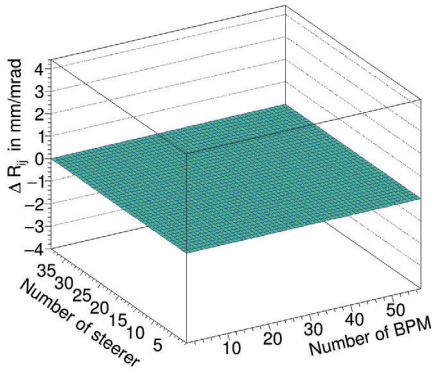

(e) Difference ORM after iteration 4.

Figure 7.9: Evolution of the difference ORM over four iterations. The initial offset is achieved by randomly disturbing the quadrupole family settings as well as the individual quadrupole gradients of the initial model lattice.

7.4 Analysis of Measurements

For a first application of the LOCO algorithm within the Bmad framework, the orbit response matrix was measured in October 2019. Therefore, the settings of the steerers were changed one after another and the corresponding orbit was measured. The set values of the quadrupole and sextupole currents were translated into quadrupole and sextupole strength values and applied to the Bmad model. The measured and the model orbit response matrix are displayed in Figure 7.10. The difference of the two matrices is also shown and serves as the starting point for the LOCO algorithm.

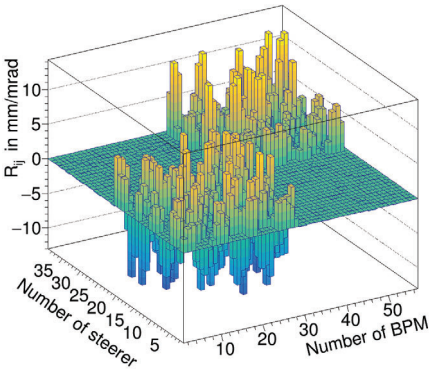

(a) Measured orbit response matrix.

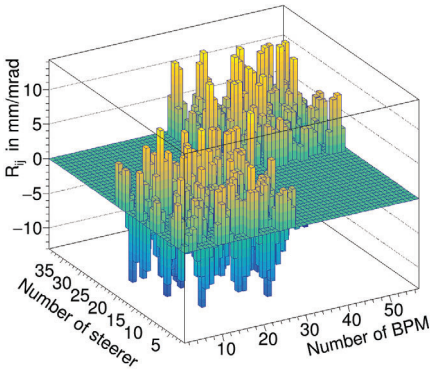

(b) Initial model orbit response matrix.

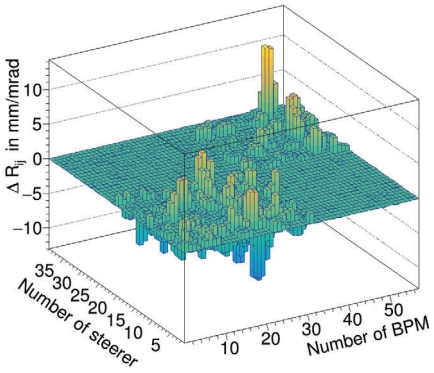

(c) Initial difference orbit response matrix.

Figure 7.10: Measured and model orbit response matrix as well as the difference matrix. The magnet settings during the measurement were applied to the Bmad model and the initial difference matrix serves as the starting point for the LOCO algorithm.

The LOCO algorithm was set up to change the quadrupole gradients as well as the positions in each direction. The influence of the initial weights for the single parameters can be seen in Figure 7.11. For each run, the weights were randomly set within a range that allows for stable operation. After setting the weights, the algorithm was stopped after 30 iterations. The χ^2/ndf value after each iteration is calculated and displayed in Figure 7.11. Independent of the initial weights, the global minimum is approached and the first iterations contribute the most to the overall χ^2 decrease. Nevertheless, there are sets of initial weights that are slightly more efficient and reach smaller χ^2 values within the same number of iterations.

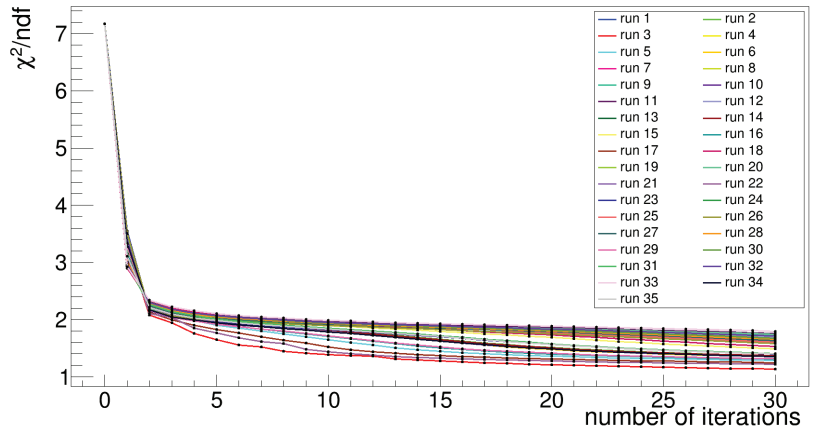

Figure 7.11: Different paths towards the global minimum of the minimization problem. Each path is the result of a different set of penalty weights.

For the most efficient set of weights, the final quadrupole gradient and position changes are given in Figure 7.12. The position changes in all three directions are mostly within the 2σ range of the communicated positioning accuracy of 0.2 mm [108]. However, one can identify larger changes in the horizontal direction. The corresponding quadrupole names are indicated in Figure 7.12. During the beam based alignment procedure in October 2019, exactly these quadrupoles were identified to have larger horizontal offsets than originally measured [96]. Due to an imperfect positioning of the reference marks on top of the magnets, the measurement of the horizontal positions turned out to be inaccurate. With a second measurement using a different method the horizontal misalignments of the named quadrupoles were investigated. The values found by the LOCO algorithm are very close to the ones that were measured. It is therefore a remarkable result that the LOCO algorithm was able to detect the same quadrupoles that were already identified by experimental investigations.

In addition to the LOCO fitting, the simulated orbits are fitted using the method from Section 7.2. Five iterations were performed and the final orbits are displayed

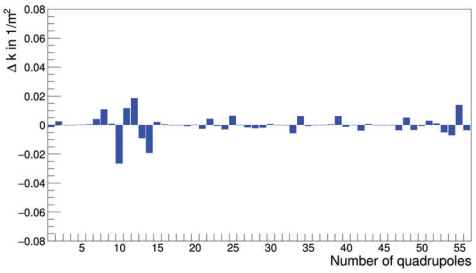

(a) Change of quadrupole gradients.

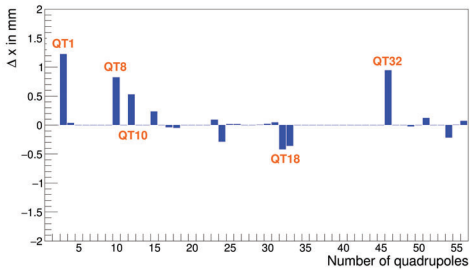

(b) Change of horizontal quadrupole offsets.

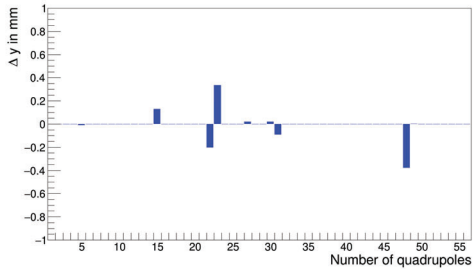

(c) Change of vertical quadrupole offsets.

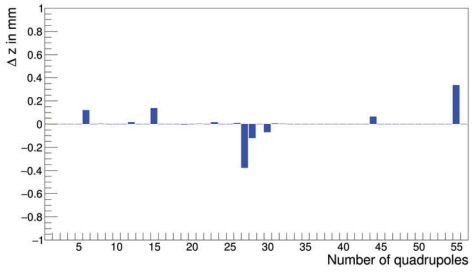

(d) Change of longitudinal quadrupole offsets.

Figure 7.12: Changes of quadrupole gradients and positions after the final LOCO iteration.

in Figure 7.13 together with the measured orbits. The corresponding steerer kicks are given in Figure 7.14. The difference orbit response matrix after using the LOCO algorithm and fitting the orbits is finally given in Figure 7.15. Compared to the initial difference given in Figure 7.10 (c), a large improvement can be seen and the final χ^2/ndf value reads

$$\chi^2/\mathrm{ndf} = 1.13. \tag{7.54}$$

Besides the horizontal and vertical orbits, also betatron function measurements at designated quadrupoles were performed in order to validate the model fitting results. Therefore, the quadrupole strength of one magnet k_i was changed and the resulting tune change was measured. The betatron function can then be determined through

$$\beta_i^{x,y} = 4\pi \cdot \frac{\Delta Q_{x,y}}{\Delta k_i L_i}, \tag{7.55}$$

where L_i is the length of the quadrupole. Both, the simulated and measured betatron function values are shown in Figure 7.16 for the investigated quadrupoles. The error bars for the measured values are relatively large since each quadrupole strength was only changed once upwards and once downwards. A more precise

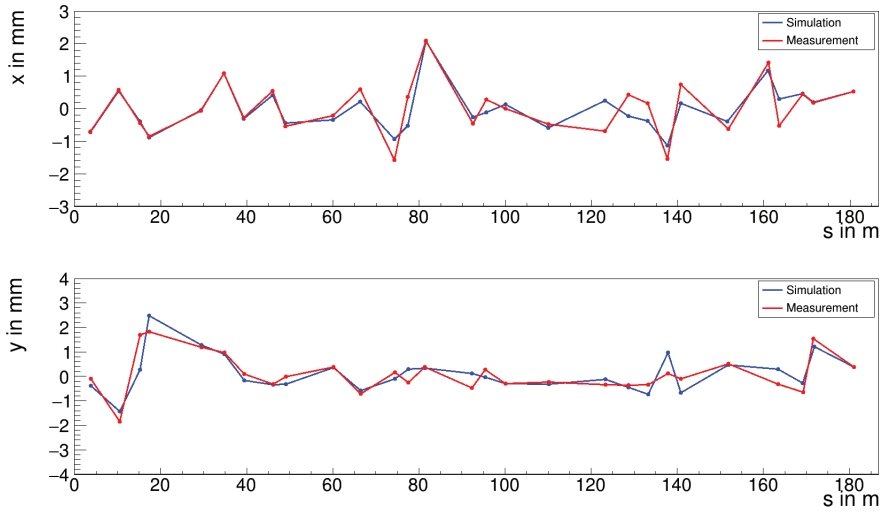

Figure 7.13: Closed orbits in horizontal and vertical direction after fitting the simulated orbits by changing the steerer kicks using the orbit matching method presented in Section 7.2 over five iterations.

value could be reached by performing more and smaller steps during a longer beam time. Nevertheless, the comparison of simulation and measurement shows a large overlap and thus validates the LOCO result. The simulated and measured betatron tunes similarly agree within a 2σ range and read

$$Q_{x,\mathrm{sim}} = 3.58210 \tag{7.56}$$
$$Q_{x,\mathrm{meas}} = 3.57119 \pm 0.00603 \tag{7.57}$$

$$Q_{y,\mathrm{sim}} = 3.59430 \tag{7.58}$$
$$Q_{y,\mathrm{meas}} = 3.58641 \pm 0.00396. \tag{7.59}$$

As the final step, the invariant spin axis of the fitted model is investigated and reads

$$\vec{n}_{c,\mathrm{sim}} = \begin{pmatrix} -3.1220590943607 \cdot 10^{-3} \\ 0.9999946293450525 \\ 9.970095598617 \cdot 10^{-4} \end{pmatrix} \pm \begin{pmatrix} 4.87 \cdot 10^{-14} \\ 2 \cdot 10^{-16} \\ 1.020 \cdot 10^{-13} \end{pmatrix}. \tag{7.60}$$

In order to investigate the stability of these values, the steerer values are randomly varied by using a Gaussian distribution and assuming an error of 1 % for each steerer kick

$$\Delta\theta_i = \mathcal{N}(\mu = 0, \sigma_i = 0.01 \cdot \theta_0), \tag{7.61}$$

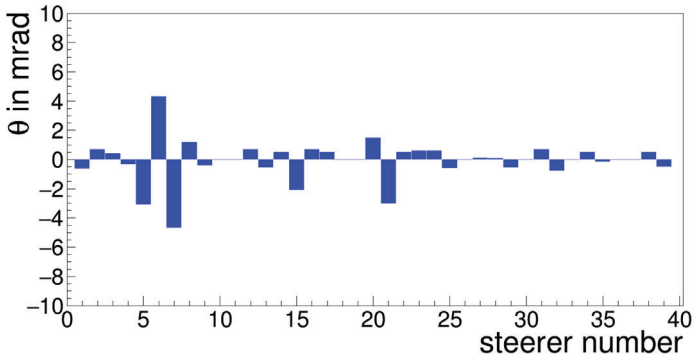

Figure 7.14: Final steerer settings after fitting the simulated closed orbits to the measured orbits using the method presented in Section 7.2.

where the steerer number is denoted by the index i. The distribution of the horizontal and longitudinal component of the invariant spin axis are shown in Figure 7.17. The widths of the Gaussian fits being performed to the data are used as an uncertainty measure for the values in Equation (7.60). In this sense, the horizontal and longitudinal component thus read

$$n_x = -3.122 \cdot 10^{-3} \pm 8.5148 \cdot 10^{-5}, \tag{7.62}$$
$$n_z = 9.97 \cdot 10^{-4} \pm 1.30637 \cdot 10^{-5}. \tag{7.63}$$

Since a change in the steerer kicks not only changes the invariant spin axis but simultaneously changes the orbit, the closed orbits for each random seed were simulated as well. The result can be seen in Figure 7.18. For the assumed steerer kick errors of 1 %, the closed orbit deviations are still small enough to be in good agreement with the measured orbits and the previously performed orbit matching is therefore still valid.

The tilt angles in horizontal and longitudinal direction that correspond to the invariant spin axis in Equation (7.60) are given by

$$\xi_{\text{sim}} = -3.122066 \text{ mrad} \pm 4.870750 \cdot 10^{-11} \text{ mrad} \tag{7.64}$$
$$\zeta_{\text{sim}} = 0.997015 \text{ mrad} \pm 1.019360 \cdot 10^{-10} \text{ mrad}. \tag{7.65}$$

The preliminary measurements based on measurements in November 2018 are given in Equations (7.28) and (7.29). The simulated tilt angle in horizontal direction is in agreement with the measurement, whereas the tilt angle in longitudinal direction is smaller than the measured one by a factor of five. The invariant spin axis is further tilted in the longitudinal direction if an additional longitudinal

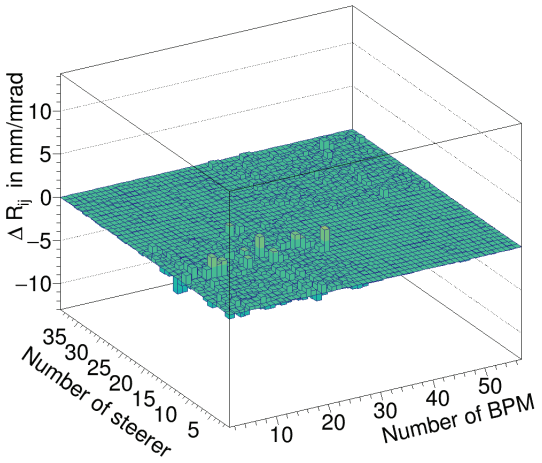

Figure 7.15: Final difference ORM after fitting the model using the LOCO algorithm as well as the orbit matching method.

magnetic field was present. Most likely this additional field component is the sum of many smaller field contributions such as fringe fields, especially in areas where the distances between magnets are small. Field map investigations have already been started to further investigate this effect [109]. An additional hint for potential improvement is provided by the simulated spin tune, which has a value of

$$\nu_{s,\mathrm{sim}} = 0.16143665 \pm 9 \cdot 10^{-14}. \tag{7.66}$$

Compared to typical measured values, it deviates upwards by about 0.0004. One reason for this can be an overestimation of steerer kicks during the orbit matching procedure that tries to minimize any remaining deviation by adjusting the steerers. The model can be further optimized by adding additional systematic effects like the fringe field overlaps mentioned above to the model. In total, one has to be careful when comparing the measured invariant spin axis and spin tune with the presented simulation results since the model optimization was performed on the basis of data taken in October 2019 where no polarized beam was available. The spin related data was taken prior to the beam based alignment procedure in an earlier beam time where different magnet settings were applied and the orbit response matrix was not measured. In the future, it is planned to do both orbit and optics as well as polarization measurements with a fixed machine setting in order to achieve a complete set of information that is needed to compare the simulation model to the real machine.

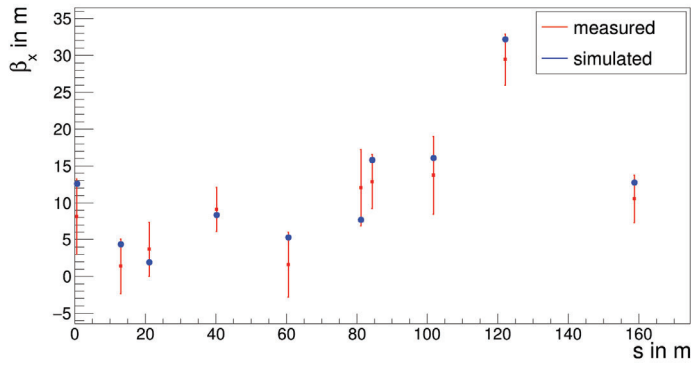

(a) Simulated and measured horizontal betatron function values.

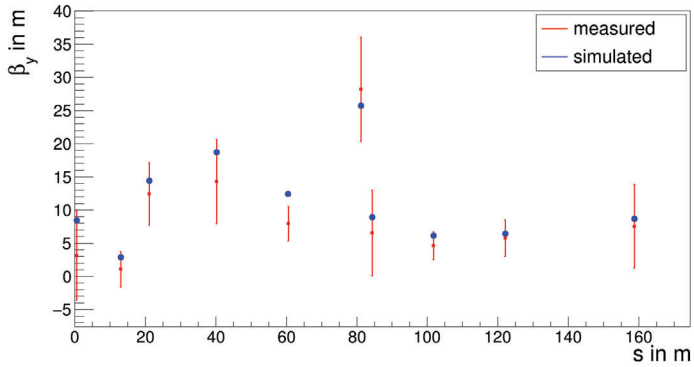

(b) Simulated and measured vertical betatron function values.

Figure 7.16: Comparison of simulated and measured betatron functions. The betatron functions are measured at the position of quadrupoles by varying the quadrupole strength and observing the corresponding betatron tune change.

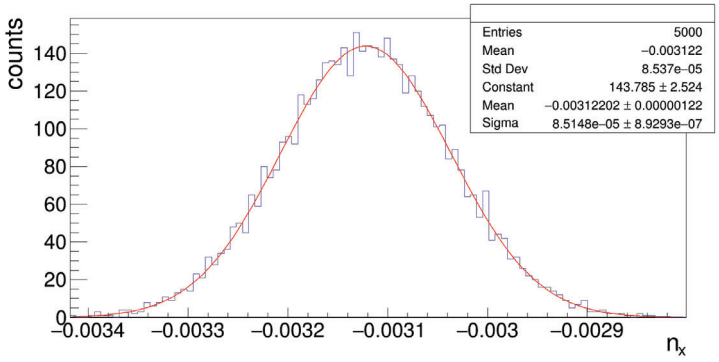

(a) Distribution of the horizontal component of the invariant spin axis.

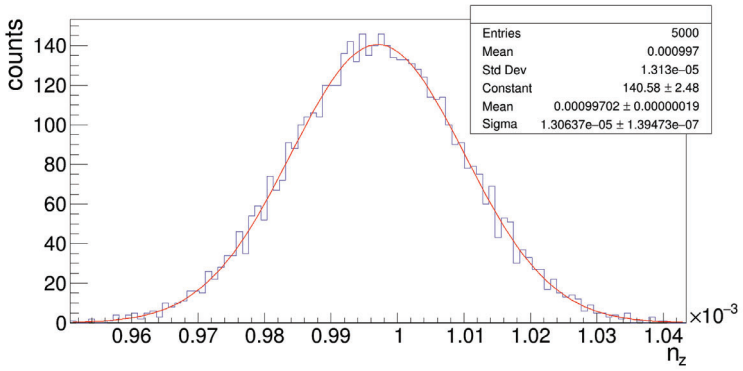

(b) Distribution of the longitudinal component of the invariant spin axis.

Figure 7.17: Distribution of the horizontal and longitudinal component of the invariant spin axis after randomly changing the steerer kicks. For each steerer, an uncertainty of 1 % was assumed. The widths of the Gaussian fits are taken as a measure of the uncertainties to the invariant spin axis components.

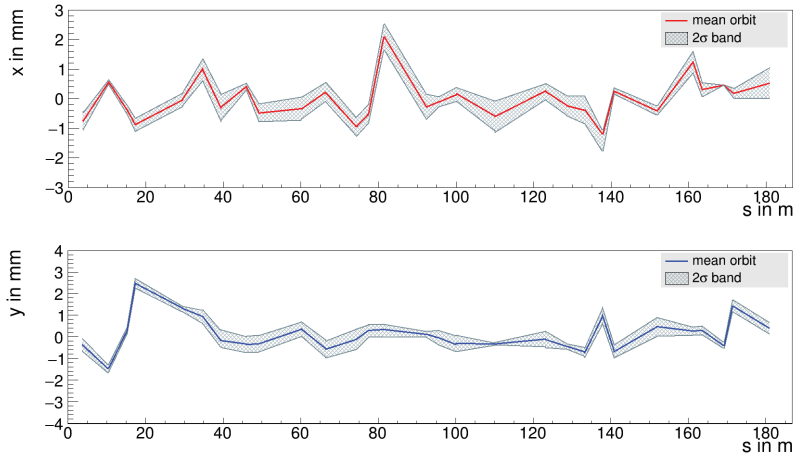

Figure 7.18: Closed orbits in horizontal (red) and vertical (blue) direction after fitting the model using the LOCO algorithm and matching the orbits by adjusting the steerer kicks. A 2σ range is shown based on randomly changed steerer kicks assuming an error of 1 % for each steerer setting.

8. Conclusion and Outlook

The existence of permanent EDMs of fundamental particles could explain the matter antimatter asymmetry in the Universe. EDMs of charged particles can be studied using storage rings as particle traps and observing the evolution of the beam polarization. In the context of this thesis, a simulation model of COSY was discussed in order to investigate systematic effects for the EDM experiment at COSY, especially their impact on the invariant spin axis. Therefore, the COSY lattice was implemented using the software library *Bmad*. The model was extended by a realistic description of the RF Wien filter using grid field maps followed by successful benchmarks against theoretical predictions. In addition, the *Bmad* library was expanded by routines that calculate the spin tune and invariant spin axis with high accuracy using spin tracking results.

In a second step, magnet misalignments and effective lengths of dipoles and quadrupoles were studied. The misalignments of all dipoles and quadrupoles that were measured after the realignment were implemented into the simulation model. The resulting closed orbit is distorted with *RMS* values at the order of 1 mm. The misalignments tilt the invariant spin axis by 0.19 mrad in horizontal and 0.23 mrad in longitudinal direction. Since both values are one order of magnitude smaller than the measured angles, the magnet misalignments can not fully explain the spin motion in COSY. However, the measurement accuracies of the misalignments were used to determine a lower limit of the EDM measurement at COSY. Randomly changing the positions and rotations within these accuracies leads to closed orbit changes. From the corresponding tilt angles distributions of the the invariant spin axis, the minimal resolvable EDM value turned out to be $1.49 \cdot 10^{-19}$ e cm. Due to closely mounted magnets, the effective length of dipoles and quadrupoles can be affected. Using first estimates for the shortening of the dipoles due to nearby steerer magnets, the effect on the closed orbit was investigated and compared to measurements. The comparison of simulated and measured orbits show large agreements when the steerer magnets are turned off. Here, further investigations are needed, since the effective length of the dipoles have to be calculated more carefully using field map simulations or even measurements. On the other hand additional orbit measurements, especially with turned off steerer magnets, are needed for a detailed comparison to simulation results. Additionally, the quadrupole fields are likely to be affected by other magnets and have to be studied in the future.

In order to improve the model quality and fit it to measurements of the real machine, two fit methods were implemented into *Bmad*, have been successfully benchmarked and applied to measurements. The first method uses the well known orbit correction algorithm to fit the simulated orbit to the measured values by changing the steerer magnets. The second method minimizes the difference of simulated and measured orbit response matrices and allows for a simultaneous fit of several different machine parameters. Combining and applying both algorithms results in a simulation model that shows large similarities to the machine quantities. The final orbits, betatron tunes as well as the betatron functions are in good agreement. The final invariant spin axis is tilted by 3.122 mrad in horizontal and 0.997 mrad in longitudinal direction. Since the measurements for the fit algorithm could only be done with an unpolarized beam, there are no direct benchmark values for the invariant spin axis. However, a comparison to former preliminary measurement results of the November 2018 beam time shows that the tilt in horizontal direction is close to the measured one. The tilt angle in longitudinal direction is around five times smaller than the measured value. To fully compare the fit algorithm results to the machine, a complete set of measurements, including optics, orbit and polarization measurements is needed.

All in all, the simulation model of COSY was successfully extended towards a more realistic description of the machine by adding several systematic effects and implementing a sophisticated fitting algorithm based on orbit response matrix measurements. The fit procedure can be used to achieve a deeper understanding of beam time measurements and can easily be extended to fit further machine parameters.

A. Appendix

A.1 Phase Space Simulations

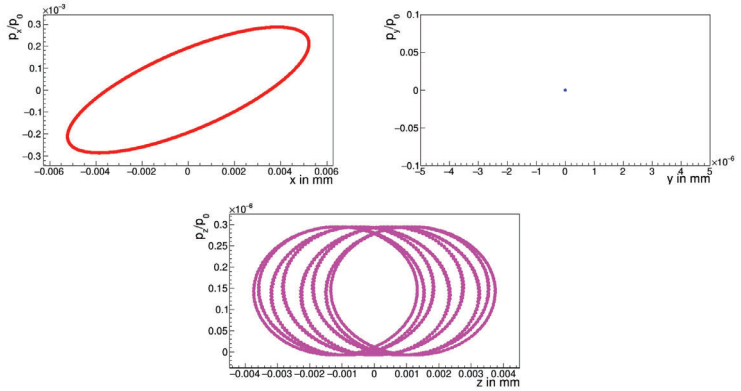

Figure A.1: Three-dimensional phase space of a particle with an initial horizontal offset at injection. Due to non-vanishing dispersion, different ellipses varying in their horizontal center position can be seen in the longitudinal phase space.

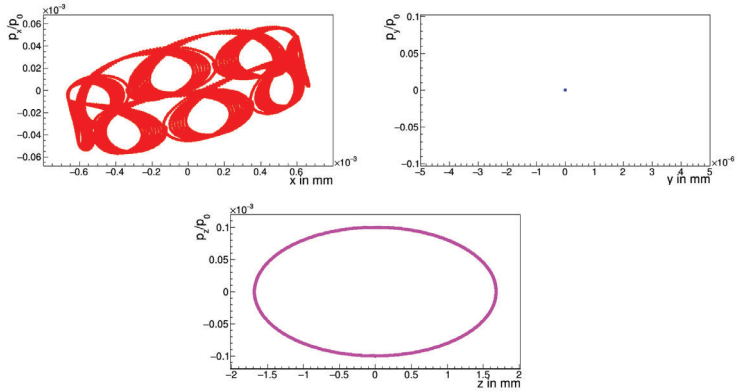

Figure A.2: Three-dimensional phase space of a particle with an initial longitudinal momentum offset of $\frac{\Delta p_z}{p_0} = 10^{-4}$ at injection. While the vertical phase space is not affected, the horizontal motion is a superposition of betatron oscillations and dispersive effects.

A.2 Default Quadrupole Settings

Quadrupole family	strength in $\frac{1}{m^2}$
QT1	-0.5639776707
QT2	0.5242107005
QT3	0.7447403327
QT4	-0.6868960770
QT5	-0.6418238093
QT6	0.5903630483
QT7	-0.6341148281
QT8	0.5903479168
QU1	-0.27125
QU2	0.333592
QU3	-0.27125
QU4	0.44548
QU5	-0.27125
QU6	0.333592

Table A.1: Default quadrupole strength settings of the COSY model. Each quadrupole family comprises four single quadrupoles. The arc quadrupoles are indicated by the letter "U", the ones in the straight sections are labeled with "T". A positive quadrupole strength represents a quadrupole that is horizontally focusing and vertically defocusing.

A.3 Magnet Misalignments

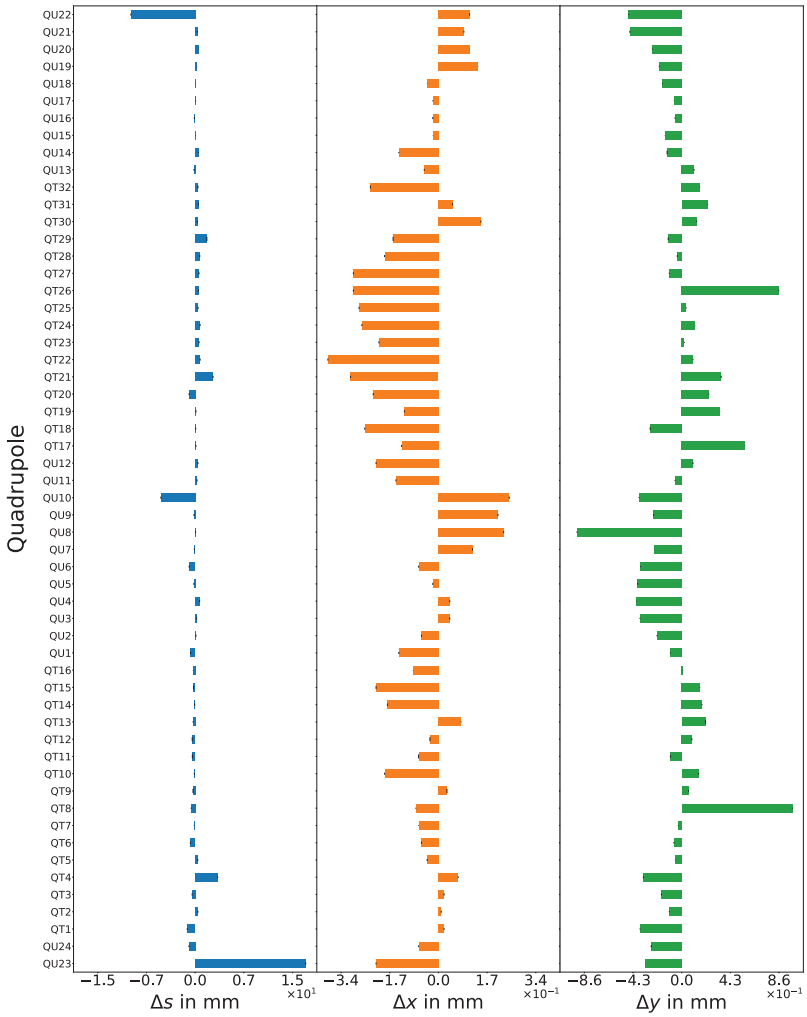

Figure A.3: Measured misalignments of all quadrupoles including the measurement uncertainties. QT1, ..., QT16 are the quadrupoles in the straight sections and QU1, ..., QU12 the quadrupoles in the arc sections of COSY. The measurements were performed in January 2020.

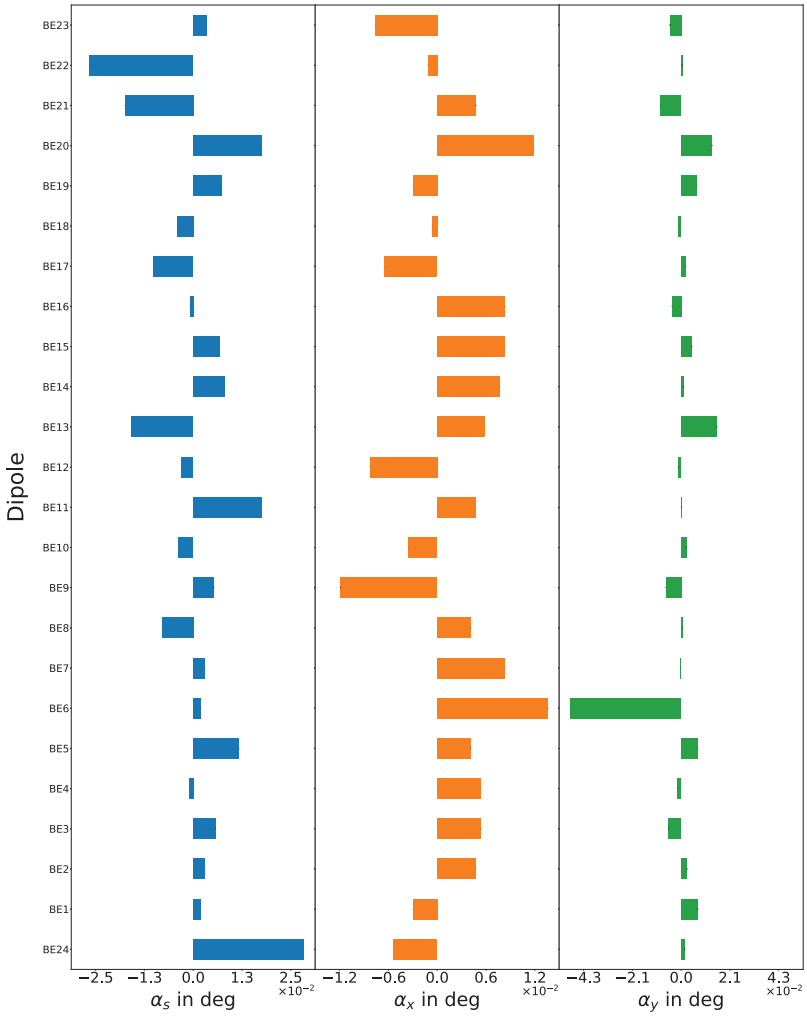

Figure A.4: Measured rotations of all dipoles including the measurement uncertainties. The individual 24 dipole magnets of COSY are denoted with B1, ..., B24. The measurements were performed in January 2020.

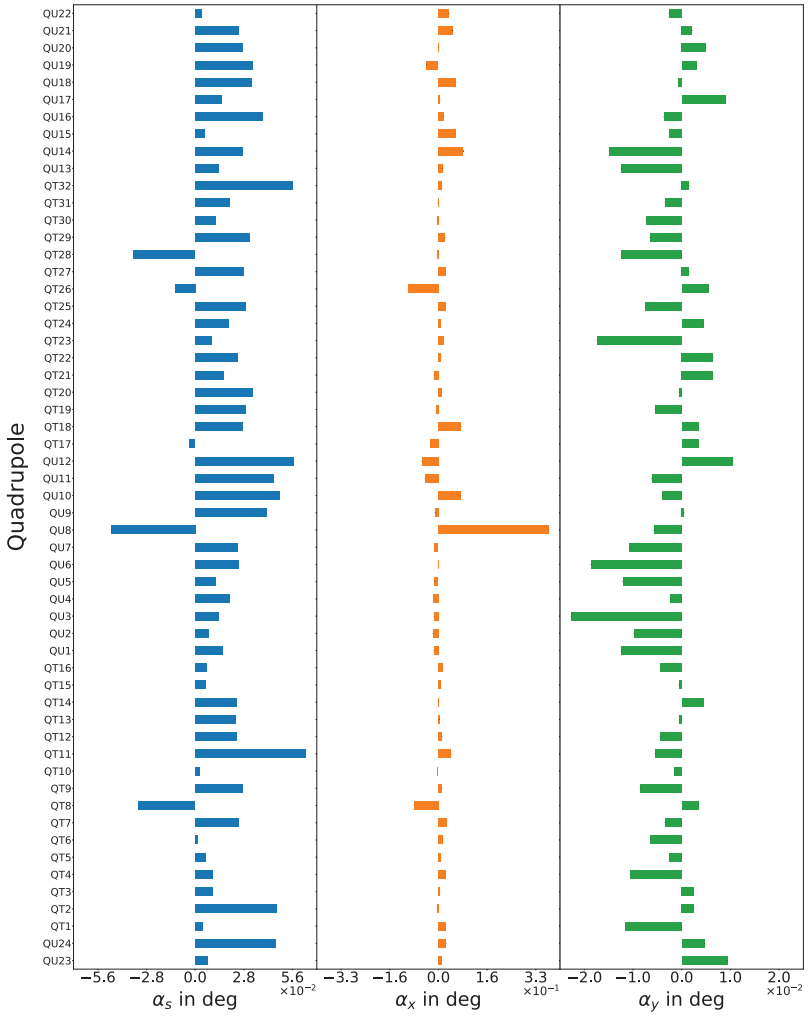

Figure A.5: Measured rotations of all quadrupoles including the measurement uncertainties. QT1, ..., QT16 are the quadrupoles in the straight sections and QU1, ..., QU12 the quadrupoles in the arc sections of COSY. The measurements were performed in January 2020.

List of Figures

List of Tables

Bibliography

[1] Vermessungsbüro Dipl.-Ing. H.J.Stollenwerk. Bahnstraße 8, 50126 Bergheim.

[2] T. Wagner and J. Pretz. Beam-based Alignment at the Cooler Syncrotron (COSY). In: *Proceedings, 10th International Particle Accelerator Conference (IPAC'19)*. 2019, pp. 3632–3634. DOI: doi:10.18429/JACoW-IPAC2019-THPGW024. URL: http://jacow.org/ipac2019/papers/thpgw024.pdf.

[3] JEDI collaboration. Homepage. http://collaborations.fz-juelich.de/ikp/jedi/. Accessed: 2019-01-27.

[4] L. Canetti, M. Drewes, and M. Shaposhnikov. Matter and Antimatter in the Universe. *New Journal of Physics,* 14 (Apr. 2012). DOI: 10.1088/1367-2630/14/9/095012.

[5] A. Riotto and M. Trodden. Recent Progress In Baryogenesis. *Annual Review of Nuclear and Particle Science,* 49 (Jan. 1999). DOI: 10.1146/annurev.nucl.49.1.35.

[6] W. Bernreuther. CP violation and baryogenesis. *Lect. Notes Phys.,* 591 (2002), pp. 237–293.

[7] E. Komatsu et al. Seven-Year Wilinson Microwave Anisotropy Probe-(WMAP) Observations: Cosmological Interpretation. *The Astrophysical Journal Supplement Series,* 192.2 (2011). DOI: 10.1088/0067-0049/192/2/18.

[8] A. D. Sakharov. Violation of CP Invariance, C asymmetry, and baryon asymmetry of the universe. *Pisma Zh. Eksp. Teor. Fiz.,* 5 (1967), pp. 32–35. DOI: 10.1070/PU1991v034n05ABEH002497.

[9] D. J. Griffiths. *Introduction to elementary particles*. Wiley-VCH, Weinheim, 2008.

[10] M. S. Sozzi. *Discrete symmetries and CP violation: from experiment to theory*. Oxford Graduate Texts. Oxford Univ. Press, 2008. DOI: 10.1093/acprof:oso/9780199296668.001.0001.

[11] T. D. Lee and C. Yang. Question of Parity Conservation in Weak Interactions. *Phys. Rev.,* 104 (1956), pp. 254–258. DOI: 10.1103/PhysRev.104.254.

[12] C. S. Wu et al. Experimental Test of Parity Conservation in Beta Decay. *Phys. Rev.,* 105 (1957), pp. 1413–1414. DOI: 10.1103/PhysRev.105.1413.

[13] M. Goldhaber, L. Grodzins, and A. W. Sunyar. Helicity of Neutrinos. *Phys. Rev.,* 109 (1958), pp. 1015–1017. DOI: 10.1103/PhysRev.109.1015.

[14] W. Greiner and J. Reinhardt. *Field Quantization.* Springer-Verlag Berlin Heidelberg, 1996.

[15] A. Angelopoulos et al. First direct observation of time-reversal non-invariance in the neutral-kaon system. *Physics Letters B,* 444 (Dec. 1998). DOI: 10.1016/S0370-2693(98)01356-2.

[16] J. H. Christenson et al. Evidence for the 2π Decay of the K_2^0 Meson. *Phys. Rev. Lett.,* 13 (1964), pp. 138–140. DOI: 10.1103/PhysRevLett.13.138.

[17] Murray Gell-Mann and A. Pais. Behavior of neutral particles under charge conjugation. *Phys. Rev.,* 97 (1955), pp. 1387–1389. DOI: 10.1103/PhysRev.97.1387.

[18] M. Kobayashi and T. Maskawa. CP Violation in the Renormalizable Theory of Weak Interaction. *Prog. Theor. Phys.,* 49 (1973), pp. 652–657. DOI: 10.1143/PTP.49.652.

[19] B. I. Khriplovich and S. Lamoreaux. *CP Violation Without Strangeness: Electric Dipole Moments of Particles, Atoms, and Molecules*. Springer-Verlag Berlin Heidelberg, 1997.

[20] N. F. Ramsey and A. Weis. Suche nach permanenten elektrischen Dipolmomenten: ein Test der Zeitumkehrinvarianz. *Physik Journal,* 52.9 (1996), pp. 859–863. DOI: 10.1002/phbl.19960520906.

[21] M. Rosenthal. *Experimental Benchmarking of Spin Tracking Algorithms for Electric Dipole Moment Searches at the Cooler Synchrotron COSY*. PhD thesis, RWTH Aachen University. 2016.

[22] A. Czarnecki and B. Krause. Neutron electric dipole moment in the standard model: Valence quark contributions. *Phys. Rev. Lett.,* 78 (1997), pp. 4339–4342. DOI: 10.1103/PhysRevLett.78.4339.

[23] M. Pospelov and A. Ritz. Electric dipole moments as probes of new physics. *Annals Phys.,* 318 (2005), pp. 119–169. DOI: 10.1016/j.aop.2005.04.002.

[24] F. Guo and U. Meißner. Baryon electric dipole moments from strong CP violation. *Journal of High Energy Physics,* 2012.12 (2012). DOI: 10.1007/JHEP12(2012)097.

[25] J. M. Pendlebury et al. Revised experimental upper limit on the electric dipole moment of the neutron. *Phys. Rev.,* D92.9 (2015). DOI: 10.1103/PhysRevD.92.092003.

[26] Steven Weinberg. A New Light Boson? *Phys. Rev. Lett.,* 40 (1978), pp. 223–226. DOI: 10.1103/PhysRevLett.40.223.

[27] R.D. Peccei and H. Quinn. CP Conservation in the Presence of Pseudoparticles. *Physical Review Letters - PHYS REV LETT,* 38 (June 1977), pp. 1440–1443. DOI: 10.1103/PhysRevLett.38.1440.

[28] J. H. Smith, E. M. Purcell, and N. F. Ramsey. Experimental Limit to the Electric Dipole Moment of the Neutron. *Phys. Rev.,* 108 (1 1957), pp. 120–122.

[29] J. Baron et al. Order of Magnitude Smaller Limit on the Electric Dipole Moment of the Electron. *Science,* 343 (2014), pp. 269–272. DOI: 10.1126/science.1248213.

[30] W. C. Griffith et al. Improved Limit on the Permanent Electric Dipole Moment of Hg-199. *Phys. Rev. Lett.,* 102 (2009). DOI: 10.1103/PhysRevLett.102.101601.

[31] G. W. Bennett et al. An Improved Limit on the Muon Electric Dipole Moment. *Phys. Rev.,* D80 (2009). DOI: 10.1103/PhysRevD.80.052008.

[32] V. F. Dmitriev and R. A. Sen'kov. Schiff moment of the mercury nucleus and the proton dipole moment. *Phys. Rev. Lett.,* 91 (2003). DOI: 10.1103/PhysRevLett.91.212303.

[33] F. Rathmann and N. Nikolaev. Precursor experiments to search for permanent electric dipole moments of protons and deuterons at COSY. In: *Proceedings, 8th International Conference on Nuclear Physics at Storage Rings*. Mar. 2012, p. 029. DOI: 10.22323/1.150.0029.

[34] D. Anastassopoulos, V. Anastassopoulos, D. Babusci, et al. *AGS Proposal: Search for a permanent electric dipole moment of the deuteron nucleus at the* 10^{-27} *ecm level*. 2004.

[35] F. J. M. Farley et al. New Method of Measuring Electric Dipole Moments in Storage Rings. *Physical Review Letters,* 93.5 (2004). DOI: 10.1103/physrevlett.93.052001. URL: http://dx.doi.org/10.1103/PhysRevLett.93.052001.

[36] K. Wille. *Physik der Teilchenbeschleuniger und Synchrotronstrahlungsquellen: Eine Einführung*. Vieweg+Teubner Verlag, 2013.

[37] H. Wiedemann. *Particle accelerator physics*. 3rd ed. Berlin: Springer, 2007.

[38] F. Hinterberger. *Physik der Teilchenbeschleuniger und Ionenoptik*. 2nd ed. Springer-Verlag, 2008. URL: https://www.bibsonomy.org/bibtex/2f1a71df0fd198c3f66e7630457e469c7/pkilian.

[39] V. Schmidt. "Analysis of Closed-Orbit Deviations for a first direct Deuteron Electric Dipole Moment Measurement at the Cooler Synchrotron COSY". MA thesis. RWTH Aachen University, 2016.

[40] J. Buon. *Beam Phase Space and Emittance*. Tech. rep. CERN, 1992.

[41] H. Ströher. EDM Experiments at Storage Rings. *EPJ Web of Conferences,* 181 (Jan. 2018). DOI: 10.1051/epjconf/201818101031.

[42] S. Y. Lee. *Spin Dynamics and Snakes in Synchrotrons*. 1st ed. World Scientific, 1997. ISBN: 9789810228057.

[43] D. Fick. *Einführung in die Kernphysik mit polarisierten Teilchen*. Mannheim, Bibliographisches Institut, 1971.

[44] G. G. Ohlsen. Polarization transfer and spin correlation experiments in nuclear physics. *Rept. Prog. Phys.,* 35 (1972), pp. 717–801. DOI: 10.1088/0034-4885/35/2/305.

[45] W. Pauli. *Zur Quantenmechanik des magnetischen Elektrons*. Vieweg Verlag, 1988.

[46] B. Povh et al. *Particles and Nuclei: An Introduction to the Physical Concepts*. Springer Berlin Heidelberg, 2002.

[47] L.H. Thomas. The Kinematics of an electron with an axis. *Phil. Mag. Ser. 7,* 3 (1927), pp. 1–21. DOI: 10.1080/14786440108564170.

[48] V. Bargmann, Louis Michel, and V.L. Telegdi. Precession of the polarization of particles moving in a homogeneous electromagnetic field. *Phys. Rev. Lett.,* 2 (1959). Ed. by Thibault Damour, Ivan Todorov, and Boris Zhilinskii, pp. 435–436. DOI: 10.1103/PhysRevLett.2.435.

[49] T. Fukuyama and A. J. Silenko. Derivation of Generalized Thomas-Bargmann-Michel-Telegdi Equation for a Particle with Electric Dipole Moment. *Int. J. Mod. Phys.,* A28 (2013). DOI: 10.1142/S0217751X13501479.

[50] J. Pretz. Measurement of Permanent Electric Dipole Moments of Charged Hadrons in Storage Rings. *Hyperfine Interactions,* 214 (Jan. 2013). DOI: 10.1007/s10751-013-0799-4.

[51] A. J. Silenko. Quantum-mechanical description of the electromagnetic interaction of relativistic particles with electric and magnetic dipole moments. *Russ. Phys. J.,* 48 (2005). [Izv. Vuz. Fiz.48,9(2005)], pp. 788–792. DOI: 10.1007/s11182-005-0203-1.

[52] BNL Storage Ring EDM Collaboration. *A Proposal to measure thr Proton Electric Dipole Moment with* 10^{-29} *ecm Sensitivity*. 2011.

[53] S. Martin, A. Lehrach, and R. M. Talman. Design of a Prototype EDM Storage Ring. In: *Proceedings, SPIN 2018*. Sept. 10, 2018, p. 144. URL: https://juser.fz-juelich.de/record/862005.

[54] F. Abusaif et al. Feasibility Study for an EDM Storage Ring (Dec. 2018). Ed. by C. Carli et al. arXiv: 1812.08535 [physics.acc-ph].

[55] V. Schmidt and A. Lehrach. Analysis of closed orbit deviations for a first direct deuteron electric dipole moment measurement at the cooler synchrotron COSY. *J. Phys. Conf. Ser.,* 874.1 (2017). DOI: 10.1088/1742-6596/874/1/012051.

[56] A. Skawran and A. Lehrach. Spin tracking for a deuteron EDM storage ring. *J. Phys. Conf. Ser.,* 874 (2017). DOI: 10.1088/1742-6596/874/1/012050.

[57] M. Rosenthal. RF Wien Filter Based EDM Measurements using Clockwise/ Counterclockwise Beams. *JEDI: Internal Note,* (2016).

[58] W. Morse, Y. Orlov, and Y. Semertzidis. Rf Wien filter in an electric dipole moment storage ring: The "partially frozen spin" effect. *Physical Review Special Topics Accelerators and Beams,* 16 (Nov. 2013). DOI: 10.1103/PhysRevSTAB.16.114001.

[59] J. Slim et al. Electromagnetic Simulation and Design of a Novel Waveguide RF Wien Filter for Electric Dipole Moment Measurements of Protons and Deuterons. *Nucl. Instrum. Meth.,* A828 (2016), pp. 116–124. DOI: 10.1016/j.nima.2016.05.012.

[60] V. Hejny and J. Pretz. Possible ways to extract the EDM from Wien filter data. *JEDI: Internal Note,* (2018).

[61] R. Maier et al. Cooler synchrotron COSY. *Nuclear Physics A,* 626 (1997), pp. 395–403.

[62] J. Slim. *A Novel Waveguide RF Wien Filter for Electric Dipole Moment Measurements of Deuterons and Protons at the COoler SYnchrotron - (COSY)/Jülich.* PhD thesis, RWTH Aachen University. 2018.

[63] R. Weidmann et al. The polarized ion source for COSY. *Review of Scientific Instruments,* 67 (Apr. 1996), pp. 1357 –1358. DOI: 10.1063/1.1146665.

[64] W. Bräutigam et al. Status and perspectives of the cyclotron JULIC as COSY injector. *Nukleonika,* 48, suppl.2 (2003), pp. 123 –126.

[65] A. Lehrach. *Erarbeitung und Umsetzung eines Konzepts zur Beschleunigung polarisierter Protonen im Kuhlersynchrotron COSY.* PhD thesis, Universität Bonn. 1998.

[66] V. Bocharov et al. Budker INP proposals for HESR and COSY electron cooler systems. In: *AIP Conference Proceedings.* Vol. 821. Mar. 2006. DOI: 10.1063/1.2190126.

[67] N. Alinovskiy et al. 2 MEV Electron Cooler for COSY and HESR – First Results. In: *Proceedings, 5th International Particle Accelerator Conference.* 2014, pp. 765–767. URL: http://juser.fz-juelich.de/record/187936.

[68] D. Mohl et al. Physics and Technique of Stochastic Cooling. *Phys. Rept.,* 58 (1980), pp. 73–119. DOI: 10.1016/0370-1573(80)90140-4.

[69] D. Prasuhn et al. Electron and stochastic cooling at COSY. *Nuclear Instruments and Methods in Physics Research Section A: Accelerators, Spectrometers, Detectors and Associated Equipment,* 441 (Feb. 2000), pp. 167–174. DOI: 10.1016/S0168-9002(99)01128-6.

[70] V.S. Morozov et al. Spin manipulation of 1.94-GeV/c polarized protons stored in the COSY cooler synchrotron. *Phys. Rev. ST Accel. Beams,* 7 (2004), p. 024002. DOI: 10.1103/PhysRevSTAB.7.024002.

[71] Ya.S. Derbenev and A.M. Kondratenko. Polarization kinematics of particles in storage rings. *Sov. Phys. JETP,* 37 (1973), pp. 968–973.

[72] P. Benati et al. Synchrotron oscillation effects on an rf-solenoid spin resonance. *Physical Review Special Topics - Accelerators and Beams,* 15 (Dec. 2012). DOI: https://doi.org/10.1103/PhysRevSTAB.15.124202.

[73] B. Hoistad et al. *Proposal for the Wide Angle Shower Apparatus (WASA) at COSY-Jülich - "WASA at COSY"*. arXiv preprint nucl-ex/0411038. 2004.

[74] O. Javakhishvili, I. Keshelashvili, and D. Mchedlishvili. A storage ring EDM polarimeter. In: *Proceedings, Journal of Physics: Conference Series*. Detection Systems, Techniques in Nuclear, and Particle Physics. Sept. 2019.

[75] G. Guidoboni et al. How to Reach a Thousand-Second in-Plane Polarization Lifetime with 0.97-GeV/c Deuterons in a Storage Ring. *Phys. Rev. Lett.,* 117.5 (2016), p. 054801. DOI: 10.1103/PhysRevLett.117.054801.

[76] D. Sagan. Bmad: A relativistic charged particle simulation library. *Nucl. Instrum. Meth.,* A558.1 (2006), pp. 356–359. ISSN: 0168-9002. DOI: https://doi.org/10.1016/j.nima.2005.11.001.

[77] M. Clausen and L. Dalesio. EPICS: Experimental physics and industrial control system. *ICFA Beam Dynamics Newsletter,* 47 (Jan. 2008).

[78] V. Hejny and J. Pretz. *Wien-filter induced spin rotations derived from the Thomas-BMT equation*. Internal Note. 2018.

[79] V. Poncza and A. Lehrach. Search for Electric Dipole Moments at Cosy in Jülich - Spin-Tracking Simulations Using Bmad. In: *Proceedings, 10th International Particle Accelerator Conference*. 2019, MOPTS028. DOI: 10.18429/JACoW-IPAC2019-MOPTS028.

[80] D. Eversmann et al. New Method for a Continuous Determination of the Spin Tune in Storage Rings and Implications for Precision Experiments. *Physical Review Letters,* 115 (9 2015). DOI: https://doi.org/10.1103/PhysRevLett.115.094801.

[81] D. Eversmann. *High Precision Spin Tune Determination at the Cooler Synchrotron in Jülich*. PhD thesis in preparation, RWTH Aachen University. 2019.

[82] W. Jellinghaus. *Magnetische Messungen an ferromagnetischen Stoffen*. De Gruyter, 1952.

[83] W. S. Wesskin and A. Kußmann. *Die Ferromagnetischen Legierungen und Ihre Gewerbliche Verwendung*. Springer-Verlag, 1932.

[84] C. Lippert. *Aufbau und Inbetriebnahme einer Multipolmessmaschine*. Jül-Spez-517, Aug. 1989.

[85] O. Ziem. *Aufrüstung eines Magnetfeldmeßsplatzes durch Einbindung einer VME-Meßmaschine*. Tech. rep. Juel-3372. 1997. URL: https://juser.fz-juelich.de/record/861487.

[86] L.H.A. Leunissen. *Non-linear transverse dynamics at the Cooler Synchrotron COSY*. PhD thesis, Technische Universität Eindhoven. 1997. DOI: https://doi.org/10.6100/IR502906.

[87] H.J. Stein. Forschungszentrum Jülich. Private communication. Apr. 2020.

[88] É. Forest. *Beam Dynamics: A New Attitude and Framework*. Vol. 8. The Physics and Technology of Particle and Photon Beams. Amsterdam, The Netherlands: Hardwood Academic / CRC Press, 1998.

[89] *Strategic Accelerator Design (SAD)*. http://acc-physics.kek.jp/SAD/. Accessed: 2020-05-25.

[90] K. Hwang and S. Y. Lee. Dipole fringe field thin map for compact synchrotrons. *Phys. Rev. ST Accel. Beams,* 18.12 (2015). DOI: 10.1103/PhysRevSTAB.18.122401.

[91] F. Zimmermann. Measurement and Correction of Accelerator Optics. In: *Proceedings, Joint US-CERN-Japan-Russian School on Beam Measurement*. May 1998, pp. 21–107. DOI: 10.1142/9789812818003_0002.

[92] O. Kovalenko et al. Orbit Response Matrix Analysis for FAIR Storage Rings. In: *Proceedings, 7th International Particle Accelerator Conference (IPAC 2016)*. 2016. DOI: 10.18429/JACoW-IPAC2016-THPMB003.

[93] H. Yanai, K. Takeuchi, and Y. Takane. *Projection Matrices, Generalized Inverse Matrices, and Singular Value Decomposition*. Statistics for Social and Behavioral Sciences. Springer, 2011.

[94] *Linear Algebra Package (LAPACK)*. https://www.cs.utexas.edu/users/plapack/. Accessed: 2020-05-20.

[95] A. Nass. "The Search for Proton and Deuteron Electric Dipole Moments using Storage Rings". Conference on Flavour Physics and CP Violation (FPCP) (Proceeding in preparation). June 2020.

[96] T. Wagner. "Beam-Based Alignment - Determining BPM offsets and quadrupole alignment". DPG-Frühjahrstagungen. 2020.

[97] J. Safranek. Experimental determination of storage ring optics using orbit response measurements. *Nucl. Instrum. Meth. A,* 388 (1997), pp. 27–36. DOI: 10.1016/S0168-9002(97)00309-4.

[98] L.S. Nadolski. Use of LOCO at Synchrotron SOLEIL. *Conf. Proc. C,* 0806233 (2008), THPC064.

[99] T. Satogata and J. Niedziela. *Simulations of RHIC Orbit Response Analysis using LOCO*. 2007.

[100] C. Weidemann et al. Model Driven Machine Improvement of COSY Based on ORM Data. In: *Proceedings, 7th International Particle Accelerator Conference*. 2016, THPMB009. DOI: 10.18429/JACoW-IPAC2016-THPMB009.

[101] D. Ji et al. First Experience of Applying Loco for Optics at Cosy. In: *Proceedings, 7th International Particle Accelerator Conference*. 2016. DOI: 10.18429/JACoW-IPAC2016-TUPMR026.

[102] K. Ott. Quadrupole misalignment determination at BESSY. *Conf. Proc. C,* 960610 (1996), pp. 890–892.

[103] Z. Marti et al. *Analytical derivatives of the orbit response matrix and dispersion for LOCO fit*. 2017.

[104] S. Y. Lee. *Accelerator Physics*. World Scientific, 2004.

[105] O. Kovalenko. *Correcting the beam optics: Orbit Response Matrix analysis for the FAIR storage rings*. http://collaborations.fz-juelich.de/ikp/jedi/. Accessed: 2020-05-23. 2016.

[106] X. Huang, J. Safranek, and G. Portmann. LOCO with constraints and improved fitting technique. *ICFA Beam Dyn. Newslett.,* 44 (2007), pp. 60–69.

[107] X. Huang et al. Fitting the Fully Coupled ORM for the Fermilab Booster. In: *Proceedings, Particle Accelerator Conference*. June 2005, pp. 3322 – 3324. DOI: 10.1109/PAC.2005.1591455.

[108] Vermessungsbüro Dipl.-Ing. H.J.Stollenwerk. Private communication. Aug. 2018.

[109] J. Böker and F. Rathmann. Private communication. Mar. 2020.

Acknowledgments

I would like to conclude my work by thanking everyone who has contributed to this work over the past years and without whom this would not have been possible.

First and foremost, I would like to thank Prof. Dr. Andreas Lehrach, who has supported me with advice all these years. Through him, I was able to gain many valuable experiences even beyond my actual work and, among other things, discovered my enthusiasm for teaching.
A further thank goes to Prof. Dr. Andrzej Magiera, who without hesitation agreed to take over the secondary supervision of my work and also gave me the opportunity to work in his group on site.
Many thanks also to Dr. Ralf Gebel, without whom this work would not have been possible in this form. It is not a matter of course to be allowed to participate in conferences all over the world as a young scientist and to gain so much experience. I appreciate this support very much.

A big thank you goes to the members of the JEDI collaboration and the staff of the IKP. Thanks for all the nice and constructive conversations and the help from all sides. It was always a great pleasure for me to work in such an international, friendly and professional environment. I wish all of them from the bottom of my heart, continued success and joy in their work. Special thanks go to Dr. Hans-Joachim Stein, who gave me many exciting suggestions, especially last year, and to Tim Wagner, who actively supported me in my measurements at COSY. I also had the good fortune to spend my daily life in the circle of other aspiring young scientists and would like to thank them for the numerous technical and non-technical discussions.

Last but not least, my thanks go to my parents, Dr. Uta Rahn-Schmidt and Dr. Klaus Peter Schmidt, who have encouraged me over all the years and whose example I have always followed. Thanks to my husband Frederic Poncza for his patience and unconditional support. I also thank the rest of my family for all their open ears, encouraging words and expressions of interest.

The past years have shaped me in many ways and the experiences I have gained will always stay with me. Thanks again to all those involved and may the force be always with you.

Eidesstattliche Erklärung

Ich, Vera Poncza,

erkläre hiermit, dass diese Dissertation und die darin dargelegten Inhalte die eigenen sind und selbstständig, als Ergebnis der eigenen originären Forschung, generiert wurden.

Hiermit erkläre ich an Eides statt

1. Diese Arbeit wurde vollständig oder größtenteils in der Phase als Doktorand dieser Fakultät und Universität angefertigt;

2. Sofern irgendein Bestandteil dieser Dissertation zuvor für einen akademischen Abschluss oder eine andere Qualifikation an dieser oder einer anderen Institution verwendet wurde, wurde dies klar angezeigt;

3. Wenn immer andere eigene- oder Veröffentlichungen Dritter herangezogen wurden, wurden diese klar benannt;

4. Wenn aus anderen eigenen- oder Veröffentlichungen Dritter zitiert wurde, wurde stets die Quelle hierfür angegeben. Diese Dissertation ist vollständig meine eigene Arbeit, mit der Ausnahme solcher Zitate;

5. Alle wesentlichen Quellen von Unterstützung wurden benannt;

6. Wenn immer ein Teil dieser Dissertation auf der Zusammenarbeit mit anderen basiert, wurde von mir klar gekennzeichnet, was von anderen und was von mir selbst erarbeitet wurde;

7. Ein Teil oder Teile dieser Arbeit wurden zuvor veröffentlicht und zwar in:

- V. Schmidt and A. Lehrach. Analysis of closed orbit deviations for a first direct deuteron electric dipole moment measurement at the cooler synchrotron COSY. Journal of Physics: Conference Series (2017).

- V. Poncza and A. Lehrach. Search for Electric Dipole Moments at Cosy in Jülich - Spin-Tracking Simulations Using Bmad. In: Proceedings, 10th International Particle Accelerator Conference (2019).

11.05.2021

_____

Vera Poncza